Spectroscopic Studies of 2D Nanomaterials

by

Benjamin Chambers

Thesis
Submitted to Flinders University
for the degree of

Doctor of Philosophy
College of Science and Engineering
November 2018

CONTENTS

ABSTRACT

Two dimensional materials are investigated with a variety of spectroscopic methods including metastable (helium) induced electron spectroscopy, ultraviolet photoelectron spectroscopy, x-ray photoelectron spectroscopy, Raman spectroscopy and Auger electron spectroscopy complimented with scanning electron microscopy. Characterising the surfaces of materials that form interfaces within a device is imperative for the development or fabrication of devices with optimal performances.

Materials such as graphene oxide, graphene and carbon nanotubes owe their electronic properties to their sp^2 networks. Graphene oxide prepared with various annealing temperatures has been characterised with ultraviolet photoelectron spectroscopy and x-ray photoelectron spectroscopy, determining the electronic structure and the composition of the surface for the temperature series. It has been determined that higher annealing temperatures resulted in improved sp^2 concentrations and hence improved charge transport properties.

The thickness of two dimensional materials is often less than the probing depth of spectroscopic methods. Graphene is characterised using metastable (helium) induced electron spectroscopy, x-ray photoelectron spectroscopy and Raman spectroscopy to exclusively determine the electronic structure of the graphene layers. It was determined that the number of layers and defects greatly influences its electronic structure.

A concept is developed to measure the inner coaxial tube within double wall carbon nanotubes utilising the difference in surface sensitivity of ultraviolet photoelectron spectroscopy and metastable (helium) electron spectroscopy. Defects in the outer walls are shown to lower the charge transport properties whilst the inner walls retain their sp^2 network and optimal charge transport properties.

MoS_2 films are characterised using ultraviolet photoelectron spectroscopy, Raman spectroscopy, Auger electron spectroscopy and scanning electron microscopy. The electronic structure of non-homogenous few layer MoS_2 is quantitatively determined and compared with bulk MoS_2.

DECLARATION

I certify that this thesis does not incorporate without acknowledgment any material previously submitted for a degree or diploma in any university; and that to the best of my knowledge and belief it does not contain any material previously published or written by another person except where due reference is made in the text.

Benjamin Andrew Chambers August 2018

ACKNOWLEDGMENTS

I would like to acknowledge my supervisors Professor Gunther Andersson and Professor Jamie Quinton. You both provided me with experiences that have modelled who I have become. I would like to thank Gunther for providing me the opportunity to take part in maintenance of the MIES/UPS/XPS instrumentation and for allowing me to work with his research group as a leader. I have learned more than I expected about teamwork, collaborations and the routines in operating a lab. I thoroughly enjoyed the hands-on experience; I am very proud of the fact that I have replaced/repaired or installed from new, close to every component that I have required. I must thank Gunther for his patience particularly in the earlier years where I consistently knocked on his door for advice. Jamie has been an idol to me since I sat in his first year physics lectures; his passion for physics and ability to highlight the physics in everyday life has always inspired me. Jamie has always been happy to lend an ear and provide advice, both on research and general life reflections. Thank you, Jamie, for being approachable, knowledgeable and for your unique combination of humour and vulnerability.

A very special person entered my life over a year ago; when I first received an email from Professor Tara Brabazon, I was expecting to encounter a dragon. I was not wrong! It must be clarified however that Tara is a dragon who fights for the students, something I found very refreshing in a world of ticking non-existent boxes and filling out rigid forms. Thank you, Tara, for supporting me in every way you could, you are a true legend.

In terms of my progress, the health of the MIES instrument was paramount. I was lucky enough to experience the workshop with multiple staff members who were all talented, friendly and hardworking. I would like to thank Bob Northeast, Christopher Price, Wayne Peacock, Mark Ellis, Bill Drury and Andrew Dunn. Your ability to immediately assist with urgent issues helped prevent further damage and lower downtime. I hope the workshop, which has since been reduced over the years, is reverted to its glory days for the benefit of future students and instruments.

I would like to thank Professor Nunzio Motta, Dr. Marco Notarianni and Professor Andrey Turchanin for their collaborations in research and for discussions regarding publications.

I would like to thank Dr. Christopher Gibson for assistance with Raman spectroscopy and our casual discussions regarding lab maintenance, your own experiences helped to reflect upon my own. I would also like to thank Dr. Cameron Shearer and LePing Yu for their collaboration in preparing the CNT and a broad range of discussions regarding research.

To my office colleagues Alex Sibley and Natalya Schmerl, thank you for being supportive, reflective and sharing odd walks to the plaza to get some fresh air. I hope you both succeed in your own ventures and find the happiness you both deserve. I would like to thank the following friends for consistent support and understanding my absence from events: Andrew Dallimore, Matthew Dunn, Oskar Majewski, Sian Le Vars, Lewis Williams, James and Megan Beal.

My PhD journey would not have been possible without my family. Your support reduced the friction in my life allowing me to do what I could. I would like to thank my parents, Suzannah and David, for providing me the opportunities with education throughout my life that allowed me to reach this point. I would like to thank my siblings Rebecca, Timothy and Annabelle for your support and for reminding me that family never changes. I would like to thank my extended family John, Michael, Carissa and Charlie for sharing their love and including me in their family.

To my loving wife Sarah, thank you for your infinite patience, your continual support of my dreams and your efforts in pushing me to grow in every aspect of life. I have always been afraid of failure, but you have helped me learn that sometimes one needs to fail, to learn how to succeed.

PUBLICATIONS

The following is a list of publications submitted during the authors candidature resulting from research presented within the dissertation:

Journal Articles

B. A. Chambers, M. Notarianni, J. Liu, N. Motta and G. Andersson, Examining the electrical and chemical properties of reduced graphene oxide with varying annealing temperatures in argon atmosphere. Applied Surface Science, 2015. 356: p. 719-725.

B. A. Chambers, C. Neumann, A. Turchanin, C. Gibson and G. Andersson, The direct measurement of the electronic density of states of graphene using metastable induced electron spectroscopy. 2D Materials, 2017. 4(2): p. 025068.

B. A. Chambers, C. J. Shearer, L. Yu, C. T. Gibson and G. Andersson, Measuring the Density of States of the Inner and Outer Wall of Double-Walled Carbon Nanotubes. Nanomaterials, 2018. 8(6).

Poster Presentations

B. A. Chambers, G. A. Andersson, J. S. Quinton, M. Notarianni and N. Motta, Towards improved charge transfer between carbon based nanostructures for flexible transparent electrodes, ACMM23 ICONN 2014, Adelaide, South Australia

B. A. Chambers, J. Quinton and G. Andersson, Metastable induced electron spectroscopy of CVD graphene and highly ordered pyrolytic graphite, 4th Annual Conference of the Flinders Centre for NanoScale Science and Technology 2014, Victoria Square, Adelaide

B. A. Chambers, J. Quinton, G. Andersson, Metastable induced electron spectroscopy of CVD graphene and highly ordered pyrolytic graphite, 20th Inelastic Ion-Surface Collisions conference (IISC-20) 2014, Wirrina Cove, Australia

B.A. Chambers, C. Neumann, A. Tuchanin, C. Gibson and G. Andersson, The first density of state measurements of graphene using metastable helium induced electron spectroscopy, 7th Annual Conference of the Flinders Centre for NanoScale Science and Technology 2017, Bedford Park, Australia

LIST OF FIGURES

LIST OF TABLES

ABBREVIATIONS

AD	Auger Deexcitation
AES	Auger electron spectroscopy
AFM	Atomic force microscopy
AMMRF	Australian Microscopy and Microanalysis Research Facility
AN	Auger neutralisation
ANFF	Australian National Fabrication Facility
ARXPS	Angle resolved x-ray photoelectron spectroscopy
CNT	Carbon nanotube
CVD	Chemical vapour deposition
DLG	Double layer graphene
DoS	Density of states
DWCNT	Double wall carbon nanotube
FOV	Field of view
FTE	Flexible transparent electrodes
FWHM	Full width half maximum
GO	Graphene oxide
rGO	Reduced graphene oxide
HOPG	Highly oriented (ordered) pyrolytic graphite
MIES	Metastable (helium) induced electron spectroscopy
MLG	Multilayer graphene
MWCNT	Multiwall carbon nanotube
RI	Resonance Ionisation
SEM	Scanning electron spectroscopy

SLG	Single layer graphene
SVD	Single value decomposition
SWCNT	Single wall carbon nanotube
TCF	Transparent conducting films
UHV	Ultra high vacuum
UP	Ultraviolet photoelectron
UPS	Ultraviolet photoelectron spectroscopy
UV	Ultraviolet
XP	X-ray photoelectron
XPS	X-ray photoelectron spectroscopy

Chapter 1

1. Introduction

1.1. Surface Science

Surface science endeavours to examine the behaviour of surfaces, interfaces or nanostructures. Through a better understanding of the characteristics and phenomena that occur at the very surface of a material; development of concepts can be made towards creating surfaces with desired properties and furthermore creating new and improved applications of these materials.

The surface of any material can be described with its physical and chemical properties. Physical properties refer to characteristics that can be observed without changing the composition of the material. Physical properties include but are not limited to: melting or boiling point, surface roughness, structure (islands, monolayer or porous nature), electrical conductivity, flexibility and hardness. Chemical properties refer to characteristics that describe the materials potential to change in composition. Examples of chemical properties include: flammability, oxidation, toxicity and radioactivity.

The aim of surface science is to localise any measurements, fabrication or modification specifically to the outer most layer of a solid; therefore, excluding any material below the first few atomic layers known as bulk material.

1.2. Nanoscience, Nanomaterials and Nanotechnology

Nanoscience is a subsection of science that specifically studies materials and phenomena on the nanoscale. 1 nanometre is defined as 1 × 10^{-9} m, the nanoscale ranges from 1 – 100 nm [1]. Nanotechnology is the application of nanoscience to create technology or manipulate materials on the nanoscale. Nanomaterials are materials that have nanoscale dimensions or materials that have been fabricated using nanotechnology. Nanomaterials can further be classified into dimensions: 3D, 2D, 1D and 0D. With each decrease in dimension the structure is confined to a thickness of a few nanometres or less: 3D describes a nanocrystalline material [2, 3]; 2D describes a sheet or thin film [4, 5]; 1D would be further confined in 2 dimensions to a nanowire or nanotube [6]; whilst 0D would be confined to a single unit such as a quantum dots or clusters [7, 8].

Properties of materials at the nanoscale are very different to macroscopic materials which are large enough to be viewed by eye. As nanomaterials become more prevalent in modern technology the importance of studying them increases. Properties such as colour, melting point, flexibility and hardness are known to drastically differ when comparing bulk material to nanomaterials [9]. One such example would be graphite (bulk) and graphene (2D nanomaterial); graphite found in a pencil shears off as we draw leaving behind an opaque line. Graphene on the other hand is a 2D material with ‘zero’ thickness, allowing it to be optically transparent.

Nanomaterials that have confined dimensions, often possess phenomena that require quantum physics to describe, this is known as quantum confinement. Classical physics describes electrons as travelling through solids as particles. Through quantum confinement the electrons are described by quantum physics as having wave-particle duality; the electron’s position is defined as a probability defined by wave functions [10]. Quantum physics is useful to describe phenomena such as quantum tunnelling where an electron can pass through an insulating material.

1.3. Solid State Physics

Solid state physics is the study of solid matter on the atomic scale to provide improved knowledge of materials on a macro scale. Solids can exist as crystalline, polycrystalline or amorphous solids. Crystalline solids possess a regular arrangement of atoms in a lattice. The symmetry within these lattices is ideal for the modelling of material behaviour by starting with a single unit and extrapolating through repeated units. Some solids however are not single crystals of repeatedly bound atoms, they will often exist as a structure consisting of smaller crystalline grains; these are known as polycrystalline solids. A material may not have any long-range order seen in crystalline solids; these are referred to as amorphous solids. A comparison between a crystalline solid and an amorphous solid is presented in Figure 1–1; the crystalline SiO_2 quartz possesses high order over a long range whilst the amorphous SiO_2 glass lacks long range order.

Figure 1-1 has been removed due to copyright restrictions

Figure 1–1: Crystalline and amorphous SiO_2 (Modified from Cao et al. [11])

A benefit of long range ordered crystalline structures is the ability to model the structure mathematically and hence be used to calculate its electronic properties. To define the electronic properties of crystalline solids, the space in which the electrons exist must be defined. In solid states physics a Bravais lattice, illustrated in Figure 1–2, is used to describe an array of discrete points generated by translation vectors:

$$\vec{\boldsymbol{R}} = n_1\vec{\boldsymbol{a}}_{\boldsymbol{1}} + n_2\vec{\boldsymbol{a}}_{\boldsymbol{2}} + n_3\vec{\boldsymbol{a}}_{\boldsymbol{3}}, \qquad \textit{Equation 1-1}$$

where the point R is defined as a sum of vectors $\vec{\mathbf{a}}_1$, $\vec{\mathbf{a}}_2$ and $\vec{\mathbf{a}}_3$, multiplied by integers n_1, n_2 and n_3.

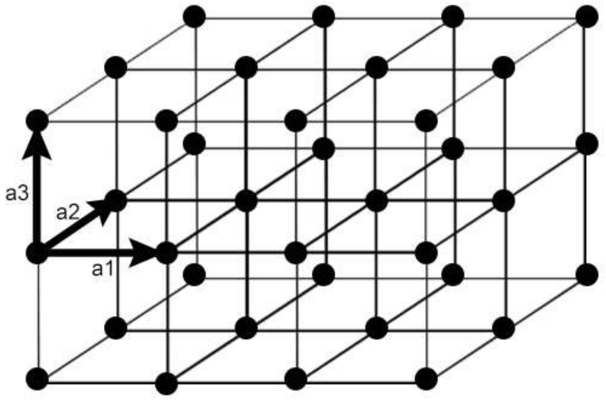

Figure 1–2: Bravais lattice

One can translate real space to the reciprocal space, also known as momentum space, using a Fourier transformation such that a lattice:

$$\vec{\boldsymbol{G}} = v_1\vec{\boldsymbol{b}}_{\boldsymbol{1}} + v_2\vec{\boldsymbol{b}}_{\boldsymbol{2}} + v_3\vec{\boldsymbol{b}}_{\boldsymbol{3}}, \qquad \textit{Equation 1-2}$$

is constructed where v are integers and $\vec{\mathbf{b}}$ are vectors; each reciprocal vector is described by the following:

$$\vec{\boldsymbol{b}}_{\boldsymbol{1}} = 2\pi\frac{(\vec{\boldsymbol{a}}_2\vec{\boldsymbol{a}}_3)}{\vec{\boldsymbol{a}}_1(\vec{\boldsymbol{a}}_2\vec{\boldsymbol{a}}_3)}, \vec{\boldsymbol{b}}_{\boldsymbol{2}} = 2\pi\frac{(\vec{\boldsymbol{a}}_1\vec{\boldsymbol{a}}_3)}{\vec{\boldsymbol{a}}_2(\vec{\boldsymbol{a}}_1\vec{\boldsymbol{a}}_3)}\, and\, \vec{\boldsymbol{b}}_{\boldsymbol{3}} = 2\pi\frac{(\vec{\boldsymbol{a}}_1\vec{\boldsymbol{a}}_2)}{\vec{\boldsymbol{a}}_3(\vec{\boldsymbol{a}}_1\vec{\boldsymbol{a}}_2)}, \qquad \textit{Equation 1-3}$$

where vectors $\vec{\mathbf{a}}_1$, $\vec{\mathbf{a}}_2$ and $\vec{\mathbf{a}}_3$ are taken from the Bravais lattice vectors. This reciprocal space unit cell is known as a Brillouin zone and is the fundamental block for examining or characterising electronic properties.

An example of a Brillouin zone for a body centred cubic (BCC) lattice is illustrated in Figure 1–3a; critical points (Γ, N, P and H) and lines of symmetry (Δ, Λ and Σ) are marked. The lines of symmetry are used to model the path an electron travels from the central atom to surrounding atoms. The energy required to move the electron within the Brillouin zone can be plotted in a band structure plot illustrated in Figure 1–3b. If an electron begins at Γ [000], where the energy is 0, travelling along the symmetry line Δ, towards point H [100], it requires 1C energy. Travelling from point H [100] to P [111] it reduces in energy, as the distance between Γ and P (Λ) is shorter. Any combination of translations within the unit cell can be made and a correlative energy required for specific movements can be illustrated on the band structure plot. In the band structure plot, there are higher levels of energy exceeding 1C; relating to movements outside of the unit cell into the next adjacent cells.

Figure 1-3 has been removed due to copyright restrictions

Figure 1–3: (a) Brillouin zone for body centred cubic (BCC) (b) the respective energy band structure plot [12]

From these band structure plots, the distribution of the electrons throughout space can be mapped. The series of allowed energies which the electrons can exist are known as energy bands. Figure 1–4 illustrates a band structure and its corresponding energy bands known as a band gap diagram; the gaps between bands occur where no electron energy states exist.

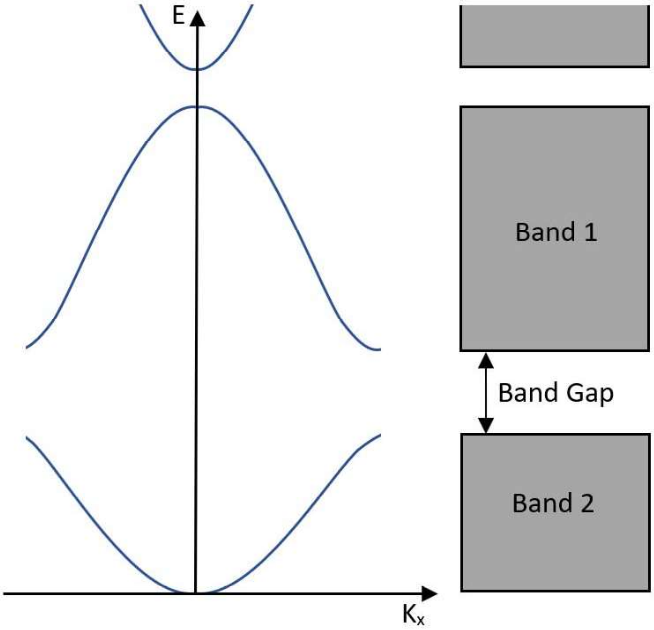

Figure 1–4: Allowed energy bands

When reviewing the electronic properties of a material, one examines the ease of which an electron can be transferred from the valence band (readily lost electrons) to the conduction band (zone where the electrons are free to move between atoms). Valence bands are filled with electrons up to the Fermi energy (E_f). The energy required to remove an electron from a material and remain at rest in vacuum is known as the vacuum level (E_{vac}) providing a reference energy threshold for the ejection of electrons [13]. The difference between the E_f and E_{vac} is the minimum energy required to remove an electron from the Fermi level into vacuum, this is known as the work function (Φ). Insulators, known for their resistance to electrical conductance, have large band gaps (Figure 1–5a) and hence require large potential differences to be applied for the electrons to overcome the gap and allow for conduction. Semiconductors possess band gaps in the range of a few eV (Figure 1–5b) and require some potential to overcome the small gap. Metals, known for their conductivity, possess valence bands and conduction bands that overlap (Figure 1–5c) and typically conduct with very little applied potential difference; hence metals are prevalent in electrical applications.

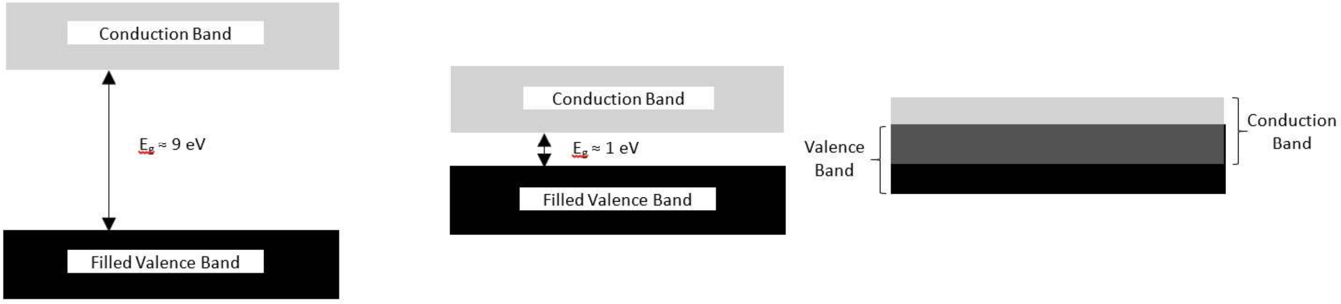

Figure 1–5: Conduction and valence bands for (a) insulators, (b) semiconductors and (c) metals

Band gaps can be directly observed in band structure plots; Figure 1–6 is an example of a semiconductor (silicon) with a small (indirect) bandgap of < 1 eV. The indirect bandgap is one where an electron requires momentum change as well as applied potential. The smallest direct bandgap in Figure 1–6 would be Γ - Γ approximately 3.4 eV.

Figure 1-6 has been removed due to copyright restrictions

Figure 1–6: Semiconductor (silicon) with band gap illustrated on band structure plot [12]

The number of permitted states which an electron can occupy at any energy can be represented by a population density known as the density of states (DoS). Figure 1–7 is an illustration of a graphene band structure and its respective DoS. The peaks in population are related to the permitted energies throughout the momentum space and relate to the probability of finding an electron at an energy. This is important for understanding electronic characteristics of a material such as predicting the amounts of electrons available for charge transport or understanding the outcomes of pairing different materials and optimising electron transport between them.

Figure 1-7 has been removed due to copyright restrictions

Figure 1–7: Graphene band structure and density of states [14].

1.4. Applications and Research Motivation

The research conducted in this thesis began with transparent conducting films (TCFs) as the primary theme before becoming instrumentally focused. Transparent conducting films are typically made from thin 2D materials that are transparent optically but also possess optimal charge transport properties [15-18]. TCFs are primarily used in devices such as touch screen devices that allow conduction of electrical signals whilst being optically transparent; allowing for users to see through the electrode and view the screen behind the user interface. TCFs can be found in photovoltaic devices, where some require the electrodes to maximise contact across an area to minimise resistance but also allow for optical light to pass through [19-22]. The transparency of a photovoltaic may allow for the active layers to receive the optimal incident spectrum of solar energy to generate electricity but may also introduce applications on windows where power can be generated but also allow a user to view beyond the device. The confined thickness also allows for materials that are typically opaque to be transparent [23]. Using materials with confined dimensions allows for phenomena such as ballistic conduction [24] to be utilised, allowing for the transport of electrons without scattering within the nanomaterial; this results in reduced resistances, heat generation and electromigration [25] which is beneficial in designing a device that has improved lifetime and efficiencies. Using nanomaterials to fabricate supercapacitors, high charge densities can be achieved, maximising energy storage in small volumes for use in portable devices such as mobile phones or wearable devices [26-30]. Transistors also benefit from nanotechnology research; through alternate device designs and higher transistor densities the performances of devices can be increased [31-34].

The performance of a device is typically a result of matching specific interfaces with desired properties. Through the characterisation of interfaces, the performances of devices can be improved [35]. The surface characterisation of 2D materials provided motivation for novel surface sensitive instrumental techniques, thus this thesis discusses the development of methodology used to characterise 2D materials.

1.5. Materials

1.5.1. Carbon Allotropes

Carbon is known to exist as various allotropes; different forms of carbon that possess different crystalline structures. Examples of allotropes include diamond, graphite, graphene and fullerenes. Diamond is a famous allotrope known for its lustrous appearance and its extreme hardness. Its properties are a result of the strong covalent bonding throughout its sp^3 tetrahedral structure. The sp^3 bonding in diamond results in it band gap of approximately 5.47 eV [36], giving it the potential to be used in semiconductor applications [36-38].

An alternative structure to the tetrahedral coordination can be found in graphite. Graphite consists of a series of sheets stacked in parallel that possess a hexagonal carbon structure. The hexagonal honeycomb structure is a result of its sp^2 hybridization which gives the carbon to carbon bonding its trigonal planar shape; the 3 carbon atoms form a bond angle of 120°. The 2s, $2p_x$ and $2p_y$ orbitals form σ bonds with neighbouring atoms whilst the remaining $2p_z$ orbitals form a perpendicular delocalised π bond. With a lattice of delocalised π bonds, the material behaves as a semimetal with its valence and conduction band overlapping by 0.3 eV [39].

Typically, graphite is synthesised for research using a pyrolytic method. Hydrocarbons are heated to high temperatures that is close to their decomposition temperature (~ 3300 K) then allowed to crystallise [40]. The resultant material is known as highly ordered pyrolytic graphite or highly oriented pyrolytic graphite (HOPG). This is ideal for research as it minimises contamination and defects providing favourable coordination for reference measurements or further studies. HOPG is often used as a refreshable surface for microscopy as the surface provides an atomically flat, non-polar surface which for elemental analysis provides only a carbon background.

Graphene is a single monolayer of carbon atoms arranged in a sp^2 hybridised lattice. It is a 2D material that is considered to be the building block of the 3D graphite [41]. K. Novoselov and A. Geim in 2010 were awarded a Nobel Prize in physics for their discovery of graphene as a stable 2D material with desirable electronic properties [42]. Similar to graphite it possesses favourable charge transport properties due to its sp^2 hybridisation; however through quantum confinement, graphene also possesses unique properties such as charge transport without scattering due its electrons behaving like massless particles (Dirac Fermions) in ambient conditions [43, 44]. In addition to the materials favourable electronic properties, graphene also possesses other advantageous properties such as transparency, strength and flexibility providing versatility for use in developing technology [45].

Graphene was first prepared through mechanical exfoliation of HOPG [42]. The separation of the many graphene sheets, held together by weak Van der Waals forces, was achieved through peeling layers using scotch tape or sonication in solution [46]. Methods for fabricating new graphene layers include: graphitisation of SiC [47], chemical self- assembly [48] and chemical vapour deposition [49-51]. Methods for transferring or reducing existing graphitic materials include: electrochemical exfoliation [52], spin coated films [53] and plasma or chemical reduction of multilayer graphene, graphene oxide or graphitic oxides [54-57].

Graphene oxide (GO) is an example of a network that has been disrupted by altering the bonds. With the carbon bound to oxygen the network is no longer fully sp^2 hybridised, replaced with functional groups such as carboxyl, hydroxyl and epoxy bridges that formed sp^3 hybridised bonds. Provided areas of sp^2 network are left for charge transport, GO is still viable for electronic applications. Advantages of using GO include functionality for attachment to other interfaces or modification for specific designs. Graphene is considered to be a zero-band gap material, introducing oxygen or other functional groups could be useful for changing the material characteristics from metallic behaviour to a semiconductor with designed work functions for use in targeted interface applications [58, 59].

Fullerenes are defined as hollow spherical carbon structures that consist of C_{20+2F} with $F \neq 1$ and $F \geq 0$ [60]. The Buckminster fullerene is a well-known example with 60 atoms bound in a network with hexagonal and pentagonal shapes resembling a football [61].

Fullerenes can also exist as hollow cylinders known as carbon nanotubes, which exist as a network of hexagonally bound carbons similar to graphene and are conceptually thought to be similar to a graphene sheet that has been rolled up into a seamless cylinder [62]. CNTs were first discovered by Iijima in 1991 [63] using a synthesis method known as arc discharge [64, 65]. Other methods of synthesising CNTs include laser ablation [65, 66] and chemical vapour deposition (CVD) [67, 68]. The first methods of synthesis typically resulted in a mixture of CNTs, fullerenes and soot (amorphous carbon), requiring further research in improving the purity and selection of specific types of CNTs. Examples of techniques being developed include; the separation of metallic and semiconducting CNTs [69], purification through oxidation [66, 70], modification of CNTs properties through bromination [71, 72] or fluorination [73-75], aligned growth [76] diameter selection [77-79] and the scalability of production [80].

CNTs, similar to graphene, have high mechanical strength, elasticity, high surface area and favourable charge transport properties [81-83] making them ideal for the advancement of technologies such as energy storage [26-28, 84], sensors [85], photovoltaic devices [86] and probe tips [87]. CNTs are capable of being modified to allow for specific properties to be tuned for their targeted device [88].

Depending on the axis in which the graphene sheet is theoretical rolled (chiral vector); the CNT will possess distinct structures that will determine whether the CNT is metallic or semiconducting [89, 90]. Chiral vectors are illustrated in Figure 1–8 on a graphene lattice. The diameter of a CNT is a result of the magnitude of the chiral vector L, an increase in L will result in a larger CNT circumference [91]. Varying the angle of the chiral vector will alter the orientation carbon atoms. With the chiral angle $\theta = 0$, the resultant orientation will exist such the carbon atoms appear to arrange in a zigzag as you travel the circumference of the tube. Increasing the angle to $\theta = \pi / 6$, will result in an orientation known as an armchair structure.

Figure 1-8 has been removed due to copyright restrictions

Figure 1–8: Chiral vectors illustrated on graphene lattice. L defines the circumference whilst the chiral angle η defines the structure. (θ = 0 corresponds to a zigzag structured CNT and θ = π / 6 corresponds to a CNT with an arm chair nanotube) [91]

The difference between the armchair and zigzag structure is illustrated in Figure 1–9. The chiral CNT is a result of any angle θ that lies between the armchair and zigzag orientation. To assist in identification, any CNT is defined by its chiral indices (n_1, n_2). The chiral indices for any zigzag CNT would be (n, 0), whilst an armchair CNT would possess chiral indices where $n_1 = n_2$.

Figure 1-9 has been removed due to copyright restrictions

Figure 1–9: Illustration of various carbon atom orientations within a CNT [92]

A plot of possible chiral CNTs is illustrated in Figure 1–10 demonstrating the importance of the chirality on its electron properties; the armchair structures behaviour like a metal, whilst various chiral and zigzag structures behave like semiconductors. The properties of CNTs vary with diameter and helicity [6, 93, 94], making the research into the structural design important: optimal CNTs can be specifically selected for the intended applications. Semiconducting CNTs are suitable but not limited to use in solar cells, transistors and diodes [95, 96]. Metallic CNTs may be desirable for uses where high metallic conductivity is required [66].

Figure 1-10 has been removed due to copyright restrictions

Figure 1–10: 2D graphene sheet with chiral indices for a range of resultant CNTs. Each possible chiral CNT is denoted with a circled dot (metallic) or dot (semiconductor) [97]

So far only single wall carbon nanotubes (SWCNTs) have been considered; nanotubes can exist coaxially with multiple layers of carbon nanotubes. Two concentric CNTs are known as double wall carbon nanotubes (DWCNTs), any other number of concentric carbon nanotubes are known as multiwall carbon nanotubes (MWCNT). The properties of SWCNTs and DWCNTs are often compared in an effort to design materials for specific applications [98, 99].

The greatest challenge found incorporating CNTs in a working device is being able to do so without disrupting its network and hence affecting its charge transport properties. CNTs have been synthesised such that the ends are used as attachment points however carbon to metal contacts are known for having high contact resistances [67, 76, 100-104]. MWCNTs are often chosen as they can carry high currents without electrical failure [105, 106]. DWCNTs and MWCNTs also have an advantage over SWCNTs as the outer walls can be modified for interface attachment or functionalisation whilst the interior CNTs remain unaffected; retaining their charge transport properties [71, 72, 74, 75, 107, 108].

In summary, when examining the electronic properties of carbon allotropes, one is interested in the sp^2 network and the delocalised π bonds which are essential for charge transport. Any modifications made to the structure will result in breaking bonds altering the availability of delocalised π bonds and reduce its charge transport ability [57]. Characterisation of these materials allows one to confirm the suitability of a material to be used in a desired application. Systematic characterisation of a sample with variations in structure can allow one to tune the appropriate properties.

1.5.2. Transition metal dichalcogenides

Transition metal dichalcogenides (TMDCs) are materials that consist of transition metals such as molybdenum (Mo) or tungsten (W) hosted by chalcogenide atoms such as sulphur (S) and Selenium (Se) [109]. A 2D TMDC will typically follow the formula: MX_2 where M is the metal and X is the chalcogenide. Common examples include MoS_2, $MoSe_2$, WS_2 and WSe_2 [110].

TMDCs similar to graphite possess a stacked 2D layer structure; the intra molecular bonds are strong with each layer being held together with weak Van der Waal forces. The electronic nature of the 2D crystal depends on its structure. Using MoS_2 as an example, the most common configurations are trigonal prismatic and octahedral structures: the trigonal prismatic structure in MoS_2 leads to a semiconducting lattice, whilst an octahedral crystal results in a metallic layer [111-113]. Top down the structures appear hexagonal and tetragonal respectively [114]; the crystal structures are illustrated in Figure 1–11 with their corresponding calculated band structures highlighting the semiconducting and metallic nature.

Figure 1-11 has been removed due to copyright restrictions

Figure 1–11: Crystal structures of monolayer MoS_2 (a) hexagonal (b) tetragonal. Calculated band structures of hexagonal (c) and tetragonal (d) MoS_2 [114]

In comparison to graphene, semiconducting MoS_2 is not a zero bandgap semiconductor [115], it possesses a direct bandgap of 1.9 eV [116] making it highly suitable for semiconductor devices that use p-n junctions [117-119] and optoelectronic devices such as lasers and light sensors [120-124]. Methods for tuning band structure include but are not limited to: changing the number of layers [116, 125-127], size of clusters or nanostructure [128], modulation of electric field effects [129], magnetic fields [130], control of disorder [131], alloys [132] and layer stacking [133].

Numerous methods of fabrication are available for TMDCs. Similar to graphene, MoS_2 can be mechanically separated due to the weak Van der Waal forces, allowing for a fresh surface to be prepared [134]. Liquid phase exfoliation (LPE) is a technique that involves sonicating the material in solution such that the layers are separated and dispersed in solution sometimes assisted using surfactants [135-138]. Thinning processes such as plasma treatments [139], laser sublimation [140, 141] and chemical etching [142-145] aim to reduce a thicker material down to desirable thicknesses or sizes. Chemical vapour deposition is often used as it is a cost-effective method for producing large areas of MX_2 films with high quality and control over both the thickness and the lateral sizes [146-150]. In addition to fabrication of TMDC materials, various methods of producing architecture or incorporation of materials into devices are available, examples include growing 2D materials into heterostructures [132, 151], stacking of materials [152], growing of TMDC nanocomposites [153] or 2D printing [154].

In summary the thickness dependence of MoS_2 and other TMDCs that when confined exhibit direct band gap behaviour promotes motivation for the study of the electronic properties with the variation in thickness. Concepts for tuning the properties through the control of the fabrication process can be examined instrumentally and allow for systems to be optimised.

1.6. References

1. Wilson, M., *Nanotechnology : basic science and emerging technologies*. 2004, Boca Raton: Chapman & Hall/CRC.
2. Anees, P., Valsakumar, M. C., Sharat, C., and Panigrahi, B. K., *Ab initio study on stacking sequences, free energy, dynamical stability and potential energy surfaces of graphite structures.* Modelling and Simulation in Materials Science and Engineering, 2014. **22**(3): p. 035016.
3. Yu, T., Liang, C. W., Kim, C., Song, E. S., and Yu, B., *Three-dimensional stacked multilayer graphene interconnects.* IEEE Electron Device Letters, 2011. **32**(8): p. 1110-1112.
4. Liu, N., Pan, Z., Fu, L., Zhang, C., Dai, B., and Liu, Z., *The origin of wrinkles on transferred graphene.* Nano Research, 2011. **4**(10): p. 996.
5. Li, X. and Zhu, H., *Two-dimensional* MoS_2*: properties, preparation, and applications.* Journal of Materiomics, 2015. **1**(1): p. 33-44.
6. Hamada, N., Sawada, S.-i., and Oshiyama, A., *New one-dimensional conductors: graphitic microtubules.* Physical Review Letters, 1992. **68**(10): p. 1579-1581.
7. Hu, S. and Wang, X., *From cluster assembly to ultrathin nanocrystals and complex nanostructures.* Science China Chemistry, 2012. **55**(11): p. 2257-2271.
8. Singh, R., *Tuning fine structure splitting and exciton emission energy in semiconductor quantum dots.* Journal of Luminescence, 2018. **202**: p. 118-131.
9. Khan, I., Saeed, K., and Khan, I., *Nanoparticles: properties, applications and toxicities.* Arabian Journal of Chemistry, 2017.
10. Griffiths, D. J., *Introduction to quantum mechanics*. 2nd ed ed. 2005: Pearson Prentice Hall.
11. Cao, C., Li, Z.-B., Wang, X.-L., Zhao, X.-B., and Han, W.-Q., *Recent advances in inorganic solid electrolytes for lithium batteries.* Frontiers in Energy Research, 2014. **2**: p. 25.
12. Hummel, R. E., *Electronic properties of materials*. 1993, Berlin: Springer.
13. Kahn, A., *Fermi level, work function and vacuum level.* Materials Horizons, 2016. **3**(1): p. 7-10.
14. Kim, D. S. *Band structures and DOS of graphene*. 6/08/2018]; Available from: https://sites.google.com/site/hrsckim/useful-info/gnuplot/example002.
15. Li, X., Zhu, Y., Cai, W., Borysiak, M., Han, B., Chen, D., Piner, R. D., Colombo, L., and Ruoff, R. S., *Transfer of large-area graphene films for high-performance transparent conductive electrodes.* Nano Letters, 2009. **9**(12): p. 4359-4363.
16. Kim, C.-L., Jung, C.-W., Oh, Y.-J., and Kim, D.-E., *A highly flexible transparent conductive electrode based on nanomaterials.* Npg Asia Materials, 2017. **9**: p. e438.
17. Kou, P., Yang, L., Chang, C., and He, S., *Improved flexible transparent conductive electrodes based on silver nanowire networks by a simple sunlight illumination approach.* Scientific Reports, 2017. **7**: p. 42052.
18. Akinwande, D., Petrone, N., and Hone, J., *Two-dimensional flexible nanoelectronics.* Nature Communications, 2014. **5**: p. 5678.
19. Shi, Z. and Jayatissa, A., *The impact of graphene on the fabrication of thin film solar cells: current status and future prospects.* Materials, 2018. **11**(1): p. 36.
20. Lee, T. D. and Ebong, A. U., *A review of thin film solar cell technologies and challenges.* Renewable and Sustainable Energy Reviews, 2017. **70**: p. 1286-1297.
21. Kuhn, L. and Gorji, N. E., *Review on the graphene/nanotube application in thin film solar cells.* Materials Letters, 2016. **171**: p. 323-326.
22. Iqbal, M. Z. and Rehman, A.-U., *Recent progress in graphene incorporated solar cell devices.* Solar Energy, 2018. **169**: p. 634-647.
23. Wei, W., Qingkai, Y., Peng, P., Zhihong, L., Jiming, B., and Shin-Shem, P., *Control of thickness uniformity and grain size in graphene films for transparent conductive electrodes.* Nanotechnology, 2012. **23**(3): p. 035603.

24. White, C. T. and Todorov, T. N., *Carbon nanotubes as long ballistic conductors.* Letters to Nature, 1998. **393**: p. 3.
25. Black, J. R., *Electromigration- a brief survey and some recent results.* IEEE Transactions on Electron Devices, 1969. **16**(4): p. 338-347.
26. Chen, X., Paul, R., and Dai, L., *Carbon-based supercapacitors for efficient energy storage.* National Science Review, 2017. **4**(3): p. 453-489.
27. Pan, H., Li, J., and Feng, Y., *Carbon nanotubes for supercapacitor.* Nanoscale Research Letters, 2010. **5**(3): p. 654-668.
28. Gong, W., Fugetsu, B., Wang, Z., Sakata, I., Su, L., Zhang, X., Ogata, H., Li, M., Wang, C., Li, J., Ortiz-Medina, J., Terrones, M., and Endo, M., *Carbon nanotubes and manganese oxide hybrid nanostructures as high performance fiber supercapacitors.* Communications Chemistry, 2018. **1**(1): p. 16.
29. Lukatskaya, M. R., Dunn, B., and Gogotsi, Y., *Multidimensional materials and device architectures for future hybrid energy storage.* Nature Communications, 2016. **7**: p. 12647.
30. Hao, Y., Santhakumar, K., Amaresh, S. P., Jae-Hyung, J., Yun Sung, L., and Wu, L., *Graphene supercapacitor with both high power and energy density.* Nanotechnology, 2017. **28**(44): p. 445401.
31. Llinas, J. P., Fairbrother, A., Borin Barin, G., Shi, W., Lee, K., Wu, S., Yong Choi, B., Braganza, R., Lear, J., Kau, N., Choi, W., Chen, C., Pedramrazi, Z., Dumslaff, T., Narita, A., Feng, X., Müllen, K., Fischer, F., Zettl, A., Ruffieux, P., Yablonovitch, E., Crommie, M., Fasel, R., and Bokor, J., *Short-channel field-effect transistors with 9-atom and 13-atom wide graphene nanoribbons.* Nature Communications, 2017. **8**(1): p. 633.
32. Chang, P., Liu, X., Di, S., and Du, G., *Evaluation of ballistic transport in III-V-Based p-Channel MOSFETs.* IEEE Transactions on Electron Devices, 2017. **64**(3): p. 1053-1059.
33. Rahman, A., Jing, G., Datta, S., and Lundstrom, M. S., *Theory of ballistic nanotransistors.* IEEE Transactions on Electron Devices, 2003. **50**(9): p. 1853-1864.
34. Chen, Y., Xu, Y., Zhao, K., Wan, X., Deng, J., and Yan, W., *Towards flexible all-carbon electronics: flexible organic field-effect transistors and iverter circuits using solution-processed all-graphene source/drain/gate electrodes.* Nano Research, 2010. **3**(10): p. 8.
35. Chambers, B. A., MacDonald, B. I., Ionescu, M., Deslandes, A., Quinton, J. S., Jasieniak, J. J., and Andersson, G. G., *Examining the role of ultra-thin atomic layer deposited metal oxide barrier layers on CdTe/ITO interface stability during the fabrication of solution processed nanocrystalline solar cells.* Solar Energy Materials and Solar Cells, 2014. **125**: p. 164-169.
36. Wort, C. J. H. and Balmer, R. S., *Diamond as an electronic material.* Materials Today, 2008. **11**(1): p. 22-28.
37. Fox, B. A., Hartsell, M. L., Malta, D. M., Wynands, H. A., Kao, C. T., Plano, L. S., Tessmer, G. J., Henard, R. B., Holmes, J. S., Tessmer, A. J., and Dreifus, D. L., *Diamond devices and electrical properties.* Diamond and Related Materials, 1995. **4**(5): p. 622-627.
38. Czelej, K., Śpiewak, P., and Kurzydłowski, K. J., *Electronic structure of substitutionally doped diamond: spin-polarized, hybrid density functional theory analysis.* Diamond and Related Materials, 2017. **75**: p. 146-151.
39. Chung, D. D. L., *Review graphite.* Journal of Materials Science, 2002. **37**(8): p. 1475-1489.
40. Blackman, L. C. F. and A. R. Ubbelohde, F. R. S., *Stress recrystallization of graphite.* Proceedings of the Royal Society of London. Series A. Mathematical and Physical Sciences, 1962. **266**(1324): p. 20.
41. Geim, A. K. and Novoselov, K. S., *The rise of graphene.* Nature Materials, 2007. **6**(March): p. 9.
42. Novoselov, K. S., Geim, A. K., Morozov, S. V., Jiang, D., Zhang, Y., Dubonos, S. V., Grigorieva, I. V., and Firsov, A. A., *Electric field effect in atomically thin carbon films.* Science, 2004. **306**(October): p. 4.

43. Novoselov, K. S., Jiang, Z., Zhang, Y., Morozov, S. V., Stormer, H. L., Zeitler, U., Maan, J. C., Boebinger, G. S., Kim, P., and Geim, A. K., *Room-temperature quantum Hall effect in graphene.* Science, 2012. **315**(March): p. 1.
44. Novoselov, K. S., Jiang, D., Schedin, F., Booth, T. J., Khotokevich, V. V., Morozov, S. V., and Geim, A. K., *Two-dimensional atomic crystals.* PNAS, 2005. **102**(July): p. 3.
45. Novoselov, K. S., Falko, V. I., Colombo, I., Gellert, P. R., Schwab, M. G., and Kim, K., *A roadmap for graphene.* Nature, 2012. **490**(October): p. 9.
46. Hernandez, Y., Nicolosi, V., Lotya, M., Blighe, F. M., Sun, Z., De, S., McGovern, I. T., Holland, B., Byrne, M., Gun'Ko, Y. K., Boland, J. J., Niraj, P., Duesberg, G., Krishnamurthy, S., Goodhue, R., Hutchison, J., Scardaci, V., Ferrari, A. C., and Coleman, J. N., *High-yield production of graphene by liquid-phase exfoliation of graphite.* Nat Nano, 2008. **3**(9): p. 563-568.
47. Emtsev, K. V., Bostwick, A., Horn, K., Jobst, J., Kellogg, G. L., Ley, L., McChesney, J. L., Ohta, T., Reshanov, S. A., Rohrl, J., Rotenberg, E., Schmid, A. K., Waldmann, D., Weber, H. B., and Seyller, T., *Towards wafer-size graphene layers by atmospheric pressure graphitization of silicon carbide.* Nat Mater, 2009. **8**(3): p. 203-207.
48. Wang, H., Wang, X., Li, X., and Dai, H., *Chemical self-assembly of graphene sheets.* Nano Research, 2009. **2**: p. 7.
49. Sun, J., Lindvall, N., Cole, M. T., Teo, K. B. K., and Yurgens, A., *Large-area uniform graphene-like thin films grown by chemical vapor deposition directly on silicon nitride.* Applied Physics Letters, 2011. **98**: p. 3.
50. Zhang, J., Hu, P., Wang, Z., Wang, Z., Liu, D., Yang, B., and Cao, W., *CVD growth of large area and uniform graphene on tilted copper foil for high performance flexible transparent conductive film.* Journal of Materials Chemistry, 2012. **22**: p. 18283-18290
51. Mattevi, C., Kim, H., and Chhowalla, M., *A review of chemical vapour deposition of graphene on copper.* Journal of Materials Chemistry, 2011. **21**(10): p. 3324-3334.
52. Liu, J., Notarianni, M., Will, G., Tiong, V. T., Wang, H., and Motta, N., *Electrochemically exfoliated graphene for electrode films: effect of graphene flake thickness on the sheet resistance and capacitive properties.* Langmuir, 2013. **29**(43): p. 13307-13314.
53. Kymakis, E., Stratakis, E., Stylianakis, M. M., Koudoumas, E., and Fotokis, C., *Spin coated graphene films as the transparent electrode in organic photovoltaic devices.* Thin Solid Films, 2011. **520**: p. 4.
54. William S. Hummers, J. and Offeman, R. E., *Preparation of graphitic oxide.* Journal of the American Chemical Society, 1958. **80**(6): p. 1339.
55. Marcano, D. C., Kosynkin, D. V., Berlin, J. M., Sinitskii, A., Sun, Z., Slesarev, A., Alemany, L. B., Lu, W., and Tour, J. M., *Improved synthesis of graphene oxide.* ACSNano, 2010. **4**(8): p. 4806-4814.
56. Luo, Z., Yu, T., Kim, K.-j., Ni, Z., You, Y., Lim, S., Shen, Z., Wang, S., and Lin, J., *Thickness-dependent reversible hydrogenation of graphene layers.* ACS Nano, 2009. **3**(7): p. 1781-1788.
57. Luo, Z., Shang, J., Lim, S., Li, D., Xiong, Q., Shen, Z., Lin, J., and Yu, T., *Modulating the electronic structures of graphene by controllable hydrogenation.* Applied Physics Letters, 2010. **97**: p. 3.
58. Elias, D. C., Nair, R. R., Mohiuddin, T. M. G., Morozov, S. V., Blake, P., Halsall, M. P., Ferrari, A. C., Boukhvalov, D. W., Katsnelson, M. I., Geim, A. K., and Novoselov, K. S., *Control of graphene's properties by reversible hydrogenation: evidence for graphane.* Science, 2009. **323**(5914): p. 610.
59. Bekyarova, E., Itkis, M. E., Ramesh, P., Berger, C., Sprinkle, M., de Heer, W. A., and Haddon, R. C., *Chemical modification of epitaxial graphene: spontaneous grafting of aryl groups.* Journal of the American Chemical Society, 2009. **131**(4): p. 1336-1337.
60. Zieleniewska, A., Lodermeyer, F., Roth, A., and Guldi, D. M., *Fullerenes - how 25 years of charge transfer chemistry have shaped our understanding of (interfacial) interactions.* Chemical Society Reviews, 2018. **47**(3): p. 702-714.

61. Kroto, H. W., Heath, J. R., O'Brien, S. C., Curl, R. F., and Smalley, R. E., *C_{60}: buckminsterfullerene.* Nature, 1985. **318**: p. 162.
62. Dresselhaus, M. S., Dresselhaus, G., Saito, R., and Jorio, A., *Raman spectroscopy of carbon nanotubes.* Physics Reports, 2005. **409**(2): p. 47-99.
63. Iijima, S., *Helical microtubules of graphitic carbon.* Nature, 1991. **354**: p. 56.
64. Arora, N. and Sharma, N. N., *Arc discharge synthesis of carbon nanotubes: comprehensive review.* Diamond and Related Materials, 2014. **50**: p. 135-150.
65. Das, R., Shahnavaz, Z., Ali, M. E., Islam, M. M., and Abd Hamid, S. B., *Can we optimize arc discharge and laser ablation for well-controlled carbon nanotube synthesis?* Nanoscale Research Letters, 2016. **11**(1): p. 510.
66. Wang, W., Fernando, K. A. S., Lin, Y., Meziani, M. J., Veca, L. M., Cao, L., Zhang, P., Kimani, M. M., and Sun, Y.-P., *Metallic single-walled carbon nanotubes for conductive nanocomposites.* Journal of the American Chemical Society, 2008. **130**(4): p. 1415-1419.
67. Sten, V., Ann, N. C., Johan van der, C., Kees, B., and Ryoichi, I., *Towards the integration of carbon nanotubes as vias in monolithic three-dimensional integrated circuits.* Japanese Journal of Applied Physics, 2013. **52**(4S): p. 04CB02.
68. Eckert, V., Leonhardt, A., Hampel, S., and Büchner, B., *Morphology of MWCNT in dependence on N-doping, synthesized using a sublimation-based CVD method at 750 °C.* Diamond and Related Materials, 2018. **86**: p. 8-14.
69. Liu, C. and Cheng, H.-M., *Controlled growth of semiconducting and metallic single-wall carbon nanotubes.* Journal of the American Chemical Society, 2016. **138**(21): p. 6690-6698.
70. Osswald, S., Flahaut, E., Ye, H., and Gogotsi, Y., *Elimination of D-band in Raman spectra of double-wall carbon nanotubes by oxidation.* Chemical Physics Letters, 2005. **402**(4): p. 422-427.
71. Bulusheva, L. G., Okotrub, A. V., Flahaut, E., Asanov, I. P., Gevko, P. N., Koroteev, V. O., Fedoseeva, Y. V., Yaya, A., and Ewels, C. P., *Bromination of double-walled carbon nanotubes.* Chemistry of Materials, 2012. **24**(14): p. 2708-2715.
72. Colomer, J. F., Marega, R., Traboulsi, H., Meneghetti, M., Van Tendeloo, G., and Bonifazi, D., *Microwave-assisted bromination of double-walled carbon nanotubes.* Chemistry of Materials, 2009. **21**(20): p. 4747-4749.
73. Wang, Y.-Q. and Sherwood, P. M. A., *Studies of carbon nanotubes and fluorinated nanotubes by X-ray and ultraviolet photoelectron spectroscopy.* Chemistry of Materials, 2004. **16**(25): p. 5427-5436.
74. Muramatsu, H., Kim, Y. A., Hayashi, T., Endo, M., Yonemoto, A., Arikai, H., Okino, F., and Touhara, H., *Fluorination of double-walled carbon nanotubes.* Chemical Communications, 2005(15): p. 2002-2004.
75. Hayashi, T., Shimamoto, D., Kim, Y. A., Muramatsu, H., Okino, F., Touhara, H., Shimada, T., Miyauchi, Y., Maruyama, S., Terrones, M., Dresselhaus, M. S., and Endo, M., *Selective optical property modification of double-walled carbon nanotubes by fluorination.* ACS Nano, 2008. **2**(3): p. 485-488.
76. Changjian, Z., Richard, S., Zachary, B., Yihan, C., Salahuddin, R., Anshul, A. V., Mansun, C., Yang, C., and Cary, Y. Y., *Synthesis and interface characterization of CNTs on graphene.* Nanotechnology, 2017. **28**(5): p. 054007.
77. Chen, Y., Malkovskiy, A., Wang, X.-Q., Lebron-Colon, M., Sokolov, A. P., Perry, K., More, K., and Pang, Y., *Selection of single-walled carbon nanotube with narrow diameter distribution by using a PPE–PPV copolymer.* ACS Macro Letters, 2012. **1**(1): p. 246-251.
78. Ramesh, S., Shan, H., Haroz, E., Billups, W. E., Hauge, R., Adams, W. W., and Smalley, R. E., *Diameter selection of single-walled carbon nanotubes through programmable solvation in binary sulfonic acid mixtures.* The Journal of Physical Chemistry C, 2007. **111**(48): p. 17827-17834.

79. Shuhei, T., Taiga, S., and Masahito, K., *Diameter control of vertically aligned carbon nanotubes using $CoFe_2O_4$ nanoparticle Langmuir–Blodgett films.* Japanese Journal of Applied Physics, 2018. **57**(3S2): p. 03EG15.
80. Jia, X. and Wei, F., *Advances in production and applications of carbon nanotubes.* Topics in Current Chemistry, 2017. **375**(1): p. 18.
81. Kumar, S., Nehra, M., Kedia, D., Dilbaghi, N., Tankeshwar, K., and Kim, K.-H., *Carbon nanotubes: a potential material for energy conversion and storage.* Progress in Energy and Combustion Science, 2018. **64**: p. 219-253.
82. Anshul, A. V., Changjian, Z., Yang, C., Phillip, W., and Cary, Y. Y., *Effect of improved contact on reliability of sub-60 nm carbon nanotube vias.* Nanotechnology, 2016. **27**(37): p. 375202.
83. Santini, C. A., Vereecken, P. M., Volodin, A., Groeseneken, G., Gendt, S. D., and Haesendonck, C. V., *A study of Joule heating-induced breakdown of carbon nanotube interconnects.* Nanotechnology, 2011. **22**(39): p. 395202.
84. Liu, L., Niu, Z., and Chen, J., *Flexible supercapacitors based on carbon nanotubes.* Chinese Chemical Letters, 2018. **29**(4): p. 571-581.
85. Jamal, G. R. A., Islam, M. R., Rahman, M. A., Meem, J. F., and Sathi, R. A. *Chirality dependence of single wall carbon nanotube based gas sensor*. in *2016 IEEE Region 10 Conference (TENCON)*. 2016.
86. Stapleton, A. J., Afre, R. A., Ellis, A. V., Shapter, J. G., Andersson, G. G., Quinton, J. S., and Lewis, D. A., *Highly conductive interwoven carbon nanotube and silver nanowire transparent electrodes.* Science and Technology of Advanced Materials, 2013. **14**(3): p. 035004.
87. Ashley, D. S., Cameron, J. S., Christopher, T. G., Joseph, G. S., David, A. L., and Andrew, J. S., *Carbon nanotube modified probes for stable and high sensitivity conductive atomic force microscopy.* Nanotechnology, 2016. **27**(47): p. 475708.
88. Spadafora, E. J., Saint-Aubin, K., Celle, C., Demadrille, R., Grevin, B., and Simonato, J.-P., *Work function tuning for flexible transparent electrodes based on functionalized metallic single walled carbon nanotubes.* Carbon, 2012. **50**: p. 6.
89. Biswas, C. and Lee Young, H., *Graphene versus carbon nanotubes in electronic devices.* Advanced Functional Materials, 2011. **21**(20): p. 3806-3826.
90. McEuen, P. L., Fuhrer, M. S., and Hongkun, P., *Single-walled carbon nanotube electronics.* IEEE Transactions on Nanotechnology, 2002. **1**(1): p. 78-85.
91. Ando, T., *The electronic properties of graphene and carbon nanotubes.* Npg Asia Materials, 2009. **1**: p. 17.
92. He, H., Pham-Huy, L. A., Dramou, P., Xiao, D., Zuo, P., and Pham-Huy, C., *Carbon nanotubes: applications in pharmacy and medicine.* BioMed Research International, 2013. **2013**: p. 12.
93. Odom, T. W., Huang, J.-L., Kim, P., and Lieber, C. M., *Structure and electronic properties of carbon nanotubes.* The Journal of Physical Chemistry B, 2000. **104**(13): p. 2794-2809.
94. Saito, R., Fujita, M., Dresselhaus, G., and Dresselhaus, M. S., *Electronic structure of chiral graphene tubules.* Applied Physics Letters, 1992. **60**(18): p. 2204-2206.
95. Si, J., Liu, L., Wang, F., Zhang, Z., and Peng, L.-M., *Carbon nanotube self-gating diode and application in integrated circuits.* ACS Nano, 2016. **10**(7): p. 6737-6743.
96. Brownlie, L. and Shapter, J., *Advances in carbon nanotube n-type doping: methods, analysis and applications.* Carbon, 2018. **126**: p. 257-270.
97. Dresselhaus, M. S., Dresselhaus, G., and Saito, R., *Physics of carbon nanotubes.* Carbon, 1995. **33**(7): p. 883-891.
98. Moore, K. E., Flavel, B. S., Ellis, A. V., and Shapter, J. G., *Comparison of double-walled with single-walled carbon nanotube electrodes by electrochemistry.* Carbon, 2011. **49**(8): p. 2639-2647.
99. Grace, T., Yu, L., Gibson, C., Tune, D., Alturaif, H., Al Othman, Z., and Shapter, J., *Investigating the effect of carbon nanotube diameter and wall number in carbon nanotube/silicon heterojunction solar cells.* Nanomaterials, 2016. **6**(3): p. 52.

100. Mizuhisa, N., Akio, K., Daiyu, K., Masahiro, H., Shintaro, S., and Yuji, A., *Electrical properties of carbon nanotube bundles for future via interconnects.* Japanese Journal of Applied Physics, 2005. **44**(4R): p. 1626.
101. Murali, R., Brenner, K., Yang, Y., Beck, T., and Meindl, J. D., *Resistivity of graphene nanoribbon interconnects.* IEEE Electron Device Letters, 2009. **30**(6): p. 611-613.
102. Zhou, C., Vyas, A. A., Wilhite, P., Wang, P., Chan, M., and Yang, C. Y., *Resistance determination for sub-100-nm carbon nanotube vias.* IEEE Electron Device Letters, 2015. **36**(1): p. 71-73.
103. Quoc, N., Cassell, A. M., Austin, A. J., Jun, L., Krishnan, S., Meyyappan, M., and Yang, C. Y., *Characteristics of aligned carbon nanofibers for interconnect via applications.* IEEE Electron Device Letters, 2006. **27**(4): p. 221-224.
104. Lee, K. J., Chandrakasan, A. P., and Kong, J., *Breakdown current density of CVD-grown multilayer graphene interconnects.* IEEE Electron Device Letters, 2011. **32**(4): p. 557-559.
105. Wei, B. Q., Vajtai, R., and Ajayan, P. M., *Reliability and current carrying capacity of carbon nanotubes.* Applied Physics Letters, 2001. **79**(8): p. 1172-1174.
106. de Pablo, P. J., Howell, S., Crittenden, S., Walsh, B., Graugnard, E., and Reifenberger, R., *Correlating the location of structural defects with the electrical failure of multiwalled carbon nanotubes.* Applied Physics Letters, 1999. **75**(25): p. 3941-3943.
107. Marcolongo, G., Ruaro, G., Gobbo, M., and Meneghetti, M., *Amino acid functionalization of double-wall carbon nanotubes studied by Raman spectroscopy.* Chemical Communications, 2007(46): p. 4925-4927.
108. Brozena, A. H., Moskowitz, J., Shao, B., Deng, S., Liao, H., Gaskell, K. J., and Wang, Y., *Outer wall selectively oxidized, water-soluble double-walled carbon nanotubes.* Journal of the American Chemical Society, 2010. **132**(11): p. 3932-3938.
109. Xia, D., Gong, F., Pei, X., Wang, W., Li, H., Zeng, W., Wu, M., and Papavassiliou, D. V., *Molybdenum and tungsten disulfides-based nanocomposite films for energy storage and conversion: A review.* Chemical Engineering Journal, 2018. **348**: p. 908-928.
110. Butler, S. Z., Hollen, S. M., Cao, L., Cui, Y., Gupta, J. A., Gutiérrez, H. R., Heinz, T. F., Hong, S. S., Huang, J., Ismach, A. F., Johnston-Halperin, E., Kuno, M., Plashnitsa, V. V., Robinson, R. D., Ruoff, R. S., Salahuddin, S., Shan, J., Shi, L., Spencer, M. G., Terrones, M., Windl, W., and Goldberger, J. E., *Progress, challenges, and opportunities in two-dimensional materials beyond graphene.* ACS Nano, 2013. **7**(4): p. 2898-2926.
111. Ganatra, R. and Zhang, Q., *Few-layer MoS_2: a promising layered semiconductor.* ACS Nano, 2014. **8**(5): p. 4074-4099.
112. Samadi, M., Sarikhani, N., Zirak, M., Zhang, H., Zhang, H.-L., and Moshfegh, A. Z., *Group 6 transition metal dichalcogenide nanomaterials: synthesis, applications and future perspectives.* Nanoscale Horizons, 2018. **3**(2): p. 90-204.
113. Guo, X., Yang, G., Zhang, J., and Xu, X., *Structural, mechanical and electronic properties of in-plane 1T/2H phase interface of MoS_2 heterostructures.* AIP Advances, 2015. **5**(9): p. 097174.
114. Huang, H., Cui, Y., Li, Q., Dun, C., Zhou, W., Huang, W., Chen, L., Hewitt, C. A., and Carroll, D. L., *Metallic 1T phase MoS_2 nanosheets for high-performance thermoelectric energy harvesting.* Nano Energy, 2016. **26**: p. 172-179.
115. Kobayashi, K. and Yamauchi, J., *Electronic structure and scanning-tunneling-microscopy image of molybdenum dichalcogenide surfaces.* Physical Review B, 1995. **51**(23): p. 17085-17095.
116. Mak, K. F., Lee, C., Hone, J., Shan, J., and Heinz, T. F., *Atomically thin MoS_2: a new direct-gap semiconductor.* Physical Review Letters, 2010. **105**(13): p. 136805.
117. Radisavljevic, B., Radenovic, A., Brivio, J., Giacometti, V., and Kis, A., *Single-layer MoS_2 transistors.* Nature Nanotechnology, 2011. **6**: p. 147.
118. Strojnik, M., Kovic, A., Mrzel, A., Buh, J., Strle, J., and Mihailovic, D., *MoS_2 nanotube field effect transistors.* AIP Advances, 2014. **4**(9): p. 097114.

119. Frisenda, R., Molina-Mendoza, A. J., Mueller, T., Castellanos-Gomez, A., and van der Zant, H. S. J., *Atomically thin p–n junctions based on two-dimensional materials.* Chemical Society Reviews, 2018. **47**(9): p. 3339-3358.
120. Splendiani, A., Sun, L., Zhang, Y., Li, T., Kim, J., Chim, C.-Y., Galli, G., and Wang, F., *Emerging photoluminescence in monolayer* MoS_2*.* Nano Letters, 2010. **10**(4): p. 1271-1275.
121. Eda, G., Yamaguchi, H., Voiry, D., Fujita, T., Chen, M., and Chhowalla, M., *Photoluminescence from chemically exfoliated* MoS_2*.* Nano Letters, 2011. **11**(12): p. 5111-5116.
122. Krasnok, A., Lepeshov, S., and Alú, A., *Nanophotonics with 2D transition metal dichalcogenides.* Optics Express, 2018. **26**(12): p. 15972-15994.
123. Lopez-Sanchez, O., Lembke, D., Kayci, M., Radenovic, A., and Kis, A., *Ultrasensitive photodetectors based on monolayer* MoS_2*.* Nature Nanotechnology, 2013. **8**: p. 497.
124. Sundaram, R. S., Engel, M., Lombardo, A., Krupke, R., Ferrari, A. C., Avouris, P., and Steiner, M., *Electroluminescence in single layer* MoS_2*.* Nano Letters, 2013. **13**(4): p. 1416-1421.
125. Kim, J. H., Lee, J., Kim, J. H., Hwang, C. C., Lee, C., and Park, J. Y., *Work function variation of* MoS_2 *atomic layers grown with chemical vapor deposition: The effects of thickness and the adsorption of water/oxygen molecules.* Applied Physics Letters, 2015. **106**(25): p. 251606.
126. Lee, C., Yan, H., Brus, L. E., Heinz, T. F., Hone, J., and Ryu, S., *Anomalous lattice vibrations of single- and few-layer* MoS_2*.* ACS Nano, 2010. **4**(5): p. 2695-2700.
127. Chernikov, A., Berkelbach, T. C., Hill, H. M., Rigosi, A., Li, Y., Aslan, O. B., Reichman, D. R., Hybertsen, M. S., and Heinz, T. F., *Exciton binding energy and nonhydrogenic Rydberg series in monolayer* WS_2*.* Physical Review Letters, 2014. **113**(7): p. 076802.
128. Lauritsen, J. V., Kibsgaard, J., Helveg, S., Topsøe, H., Clausen, B. S., Lægsgaard, E., and Besenbacher, F., *Size-dependent structure of* MoS_2 *nanocrystals.* Nature Nanotechnology, 2007. **2**: p. 53.
129. Li, Y., Xu, C.-Y., Zhang, B.-Y., and Zhen, L., *Work function modulation of bilayer* MoS_2 *nanoflake by backgate electric field effect.* Applied Physics Letters, 2013. **103**(3): p. 033122.
130. Li, T. S. and Ho, Y. H., *Electronic properties of monolayer* MoS_2 *in a modulated magnetic field.* Physics Letters A, 2016. **380**(3): p. 444-451.
131. Mignuzzi, S., Pollard, A. J., Bonini, N., Brennan, B., Gilmore, I. S., Pimenta, M. A., Richards, D., and Roy, D., *Effect of disorder on Raman scattering of single-layer* MoS_2*.* Physical Review B, 2015. **91**(19): p. 195411.
132. Zhang, X., Lai, Z., Ma, Q., and Zhang, H., *Novel structured transition metal dichalcogenide nanosheets.* Chemical Society Reviews, 2018. **47**(9): p. 3301-3338.
133. Bernardi, M., Palummo, M., and Grossman, J. C., *Extraordinary sunlight absorption and one nanometer thick photovoltaics using two-dimensional monolayer materials.* Nano Letters, 2013. **13**(8): p. 3664-3670.
134. Young, P. A., *Lattice parameter measurements on molybdenum disulphide.* Journal of Physics D: Applied Physics, 1968. **1**(7): p. 936.
135. Bang, G. S., Nam, K. W., Kim, J. Y., Shin, J., Choi, J. W., and Choi, S.-Y., *Effective liquid-phase exfoliation and sodium ion battery application of* MoS_2 *nanosheets.* ACS Applied Materials & Interfaces, 2014. **6**(10): p. 7084-7089.
136. Guardia, L., Paredes, J. I., Rozada, R., Villar-Rodil, S., Martínez-Alonso, A., and Tascón, J. M. D., *Production of aqueous dispersions of inorganic graphene analogues by exfoliation and stabilization with non-ionic surfactants.* RSC Advances, 2014. **4**(27): p. 14115-14127.
137. Gupta, A., Arunachalam, V., and Vasudevan, S., *Water dispersible, positively and negatively charged* MoS_2 *nanosheets: surface chemistry and the role of surfactant binding.* The Journal of Physical Chemistry Letters, 2015. **6**(4): p. 739-744.
138. Manna, K., Huang, H.-N., Li, W.-T., Ho, Y.-H., and Chiang, W.-H., *Toward understanding the efficient exfoliation of layered materials by water-assisted cosolvent liquid-phase exfoliation.* Chemistry of Materials, 2016. **28**(21): p. 7586-7593.

139. Nan, H., Wang, Z., Wang, W., Liang, Z., Lu, Y., Chen, Q., He, D., Tan, P., Miao, F., Wang, X., Wang, J., and Ni, Z., *Strong photoluminescence enhancement of* MoS_2 *through defect engineering and oxygen bonding.* ACS Nano, 2014. **8**(6): p. 5738-5745.

140. Cho, S., Kim, S., Kim, J. H., Zhao, J., Seok, J., Keum, D. H., Baik, J., Choe, D.-H., Chang, K. J., Suenaga, K., Kim, S. W., Lee, Y. H., and Yang, H., *Phase patterning for ohmic homojunction contact in* $MoTe_2$*.* Science, 2015. **349**(6248): p. 625.

141. Castellanos-Gomez, A., Barkelid, M., Goossens, A. M., Calado, V. E., van der Zant, H. S. J., and Steele, G. A., *Laser-thinning of* MoS_2*: on demand generation of a single-layer semiconductor.* Nano Letters, 2012. **12**(6): p. 3187-3192.

142. Kim, K. S., Kim, K. H., Nam, Y., Jeon, J., Yim, S., Singh, E., Lee, J. Y., Lee, S. J., Jung, Y. S., Yeom, G. Y., and Kim, D. W., *Atomic layer etching mechanism of* MoS_2 *for nanodevices.* ACS Applied Materials & Interfaces, 2017. **9**(13): p. 11967-11976.

143. Dong, L., Lin, S., Yang, L., Zhang, J., Yang, C., Yang, D., and Lu, H., *Spontaneous exfoliation and tailoring of* MoS_2 *in mixed solvents.* Chemical Communications, 2014. **50**(100): p. 15936-15939.

144. Amani, M., Lien, D.-H., Kiriya, D., Xiao, J., Azcatl, A., Noh, J., Madhvapathy, S. R., Addou, R., Kc, S., Dubey, M., Cho, K., Wallace, R. M., Lee, S.-C., He, J.-H., Ager, J. W., Zhang, X., Yablonovitch, E., and Javey, A., *Near-unity photoluminescence quantum yield in* MoS_2*.* Science, 2015. **350**(6264): p. 1065.

145. Amani, M., Taheri, P., Addou, R., Ahn, G. H., Kiriya, D., Lien, D.-H., Ager, J. W., Wallace, R. M., and Javey, A., *Recombination kinetics and effects of superacid treatment in sulfur- and selenium-based transition metal dichalcogenides.* Nano Letters, 2016. **16**(4): p. 2786-2791.

146. Peimyoo, N., Shang, J., Cong, C., Shen, X., Wu, X., Yeow, E. K. L., and Yu, T., *Nonblinking, intense two-dimensional light emitter: monolayer* WS_2 *triangles.* ACS Nano, 2013. **7**(12): p. 10985-10994.

147. Zhou, S., Gan, L., Wang, D., Li, H., and Zhai, T., *Space-confined vapor deposition synthesis of two dimensional materials.* Nano Research, 2018. **11**(6): p. 2909-2931.

148. Song, J.-G., Park, J., Lee, W., Choi, T., Jung, H., Lee, C. W., Hwang, S.-H., Myoung, J. M., Jung, J.-H., Kim, S.-H., Lansalot-Matras, C., and Kim, H., *Layer-controlled, wafer-scale, and conformal synthesis of tungsten disulfide nanosheets using atomic layer deposition.* ACS Nano, 2013. **7**(12): p. 11333-11340.

149. Elías, A. L., Perea-López, N., Castro-Beltrán, A., Berkdemir, A., Lv, R., Feng, S., Long, A. D., Hayashi, T., Kim, Y. A., Endo, M., Gutiérrez, H. R., Pradhan, N. R., Balicas, L., Mallouk, T. E., López-Urías, F., Terrones, H., and Terrones, M., *Controlled synthesis and transfer of large-area* WS_2 *sheets: from single layer to few layers.* ACS Nano, 2013. **7**(6): p. 5235-5242.

150. Lee, Y., Lee, J., Bark, H., Oh, I.-K., Ryu, G. H., Lee, Z., Kim, H., Cho, J. H., Ahn, J.-H., and Lee, C., *Synthesis of wafer-scale uniform molybdenum disulfide films with control over the layer number using a gas phase sulfur precursor.* Nanoscale, 2014. **6**(5): p. 2821-2826.

151. Winter, A., George, A., Neumann, C., Tang, Z., Mohn, M. J., Biskupek, J., Masurkar, N., Reddy, A. L. M., Weimann, T., Hübner, U., Kaiser, U., and Turchanin, A., *Lateral heterostructures of two-dimensional materials by electron-beam induced stitching.* Carbon, 2018. **128**: p. 106-116.

152. Zhang, C., Johnson, A., Hsu, C.-L., Li, L.-J., and Shih, C.-K., *Direct imaging of band profile in single layer* MoS_2 *on graphite: quasiparticle energy gap, metallic edge states, and edge band bending.* Nano Letters, 2014. **14**(5): p. 2443-2447.

153. Deng, Z., Jiang, H., and Li, C., *2D metal chalcogenides incorporated into carbon and their assembly for energy storage applications.* Small, 2018. **14**(22): p. 1800148.

154. Hu, G., Kang, J., Ng, L. W. T., Zhu, X., Howe, R. C. T., Jones, C. G., Hersam, M. C., and Hasan, T., *Functional inks and printing of two-dimensional materials.* Chemical Society Reviews, 2018. **47**(9): p. 3265-3300.

Chapter 2

2. Instrumental

2.1.Photoelectron Spectroscopy

Electromagnetic radiation can be directed towards a surface and will result in the excitation of the electrons at the surface. With sufficient energy, electrons can be ejected from the sample; this is known as the photoelectric effect. The kinetic energy of an electron $E_{kinetic}$ can be described using the photoelectric equation; a modified version of Einstein's equation [1]:

$$E_{kinetic} = E_{photon} - (\Phi_{spectrometer} + E_{binding}) \qquad \textit{Equation 2-1}$$

Where E_{photon} is the energy of the incident photon, $\Phi_{spectrometer}$ is the work function of the spectrometer and $E_{binding}$ is the binding energy of the electrons that were ejected from the surface. Thus, Equation 2-1 can be rearranged to:

$$E_{binding} = E_{photon} - E_{kinetic} - \Phi_{spectrometer} \qquad \textit{Equation 2-2}$$

Knowing the applied photon energy and measuring the kinetic energy of the electrons detected, one can calculate the binding energy of the electrons at the surface of the material. The work function of the spectrometer has been calibrated to incorporate its value which may vary over time or with catastrophic events; such as high doses of low energy electrons or atmospheric vents.

The incoming photon energy will determine whether electrons from the core or the valence orbitals will be ejected and detected. The valence electrons are easily ejected with low excitation energies given they exist on the outer shells of an atom and experience less attraction to the nucleus. The core electrons situated closer to the nucleus require higher energy photons to overcome the attractive forces and eject from the surface.

Photoelectron spectroscopy is ideal for analysing surfaces as the electron mean free path, the distance an electron will travel before it interacts with surrounding atoms or electrons, is less than 10 nm between energies of 10 - 1500 eV. Therefore, any information obtained from photoelectron spectroscopy is unique to the surface layers and not the bulk material.

The attenuation of the electrons intensity as it penetrates through matter is described by:

$$I(d,E) = I_0 exp\left(-\frac{x}{\lambda(E)}\right)$$ *Equation 2-3*

Where I is the measured intensity, I_0 is the initial electron energy, x is the total displacement of the electron, λ is the path length of an electron which varies for different energies and is experimentally determined [2].

A plot of the mean free path of an electron can be made against the energy of an electron showing the variation in the depth sensitivity with the applied energy. In Figure 2–1 the mean free path of an electron with 0 eV binding energy excited by a He 1 source (UPS) is approximately 1- 5 monolayers whilst the aluminium source (XPS) has an electron mean free path of approximately 9 monolayers. As the binding energy of electrons increases the surface sensitivities will change throughout the scale as the electron mean free path will alter with electron energy. For a typical measurement, electrons of interest in XPS will have binding energies less than 800 eV whilst electrons examined in UPS will have binding energies less than 15 eV. As such the range of mean free path for XPS ranges from 9 to 3 monolayers with increasing binding energy, whilst the mean free path for UPS will range from 2 to 20 monolayers with increasing binding energy. As such the information from UPS and XPS overlap in surface sensitivity.

Figure 2-1 has been removed due to copyright restrictions

Figure 2–1: Electron mean free path [2]

2.2. Ultraviolet Photoelectron Spectroscopy

Ultraviolet photoelectron spectroscopy (UPS) examines the kinetic energy of photoelectrons ejected from the valence bands as a result of excitation using ultraviolet (UV) radiation. The UV light, used to excite the electrons within this thesis, is generated using a helium discharge lamp producing UV light of 21.2 eV (He I). The electrons ejected from the samples surface travel through UHV space and accelerated towards the hemispherical spectrometer (PHOBIOS 150) with a bias of -10 V. The additional bias of -10 V ensures that all the secondary electrons are emitted by adding to the kinetic energy of the electrons. This allows for a secondary electron cut-off to be examined giving information about the materials work function. The spectrometer measures the kinetic energy of the electrons and counts the population of electrons with each kinetic energy. The measured energy includes the -10 eV from the bias as such the binding energy can be calculated for the electrons measured by UPS with the following equation:

$$E_{binding} = 21.2\ eV - (E_{kinetic} + 10\ eV) - \Phi_{spectrometer} \qquad \textit{Equation 2-4}$$

The valence electrons provide information as to the electrons that will be excited to the unoccupied orbitals to allow for electronic conduction. The measured spectrum of valence electrons will provide a representation for the density of states described in the solid states section.

When intrinsic semiconductors, studied within this thesis, are connected to ground, the energy levels align such that the Fermi level becomes 0 eV [3], unlike doped semiconductors known as extrinsic semiconductors which are not studied in this thesis. In Figure 2–2 a representation of the bandgap, for intrinsic semiconductors, can be made by taking the difference between the valence cut off (E_v) and the Fermi level (E_f = 0 eV); the bandgap is approximately twice E_v - E_f. The general structure of the spectrum is controlled by the DoS of the surface as determined by a materials band structure; features observed directly correlate to the band structure of a materials surface. The large peak at 16 eV in Figure 2–2 is known as the secondary electron peak; this is a background signal that results from electrons undergoing numerous inelastic collisions prior to being detected. With each collision an electron loses energy such that the final kinetic energy of the measured electron is less than a similar electron that experienced no collisions. As such the secondary electron feature is an ambiguous signal of electrons originating from various lower binding energies after undergoing a variety of collisions. The secondary electron cut-off, also known as the high energy cut-off, is the lowest energy of electrons that are detected; any electrons with lower kinetic energy are trapped at the surface and not ejected. The difference between the applied energy (E_{photon}) and the high energy cut-off provides the work function of the surface; the energy required to remove an electron from the surface of a solid in vacuum. In this example the applied energy of the ultraviolet light He I is 21.2 eV and the cut-off is 17.4 eV allowing for the work function to be calculated (21.2 eV - 17.4 eV = 3.8 eV). Changes in chemical bonding will result in the valence electrons being altered and the DoS also changing, shifting may also be a result of surface charging if the surface has areas insulated from the grounding or applied potential.

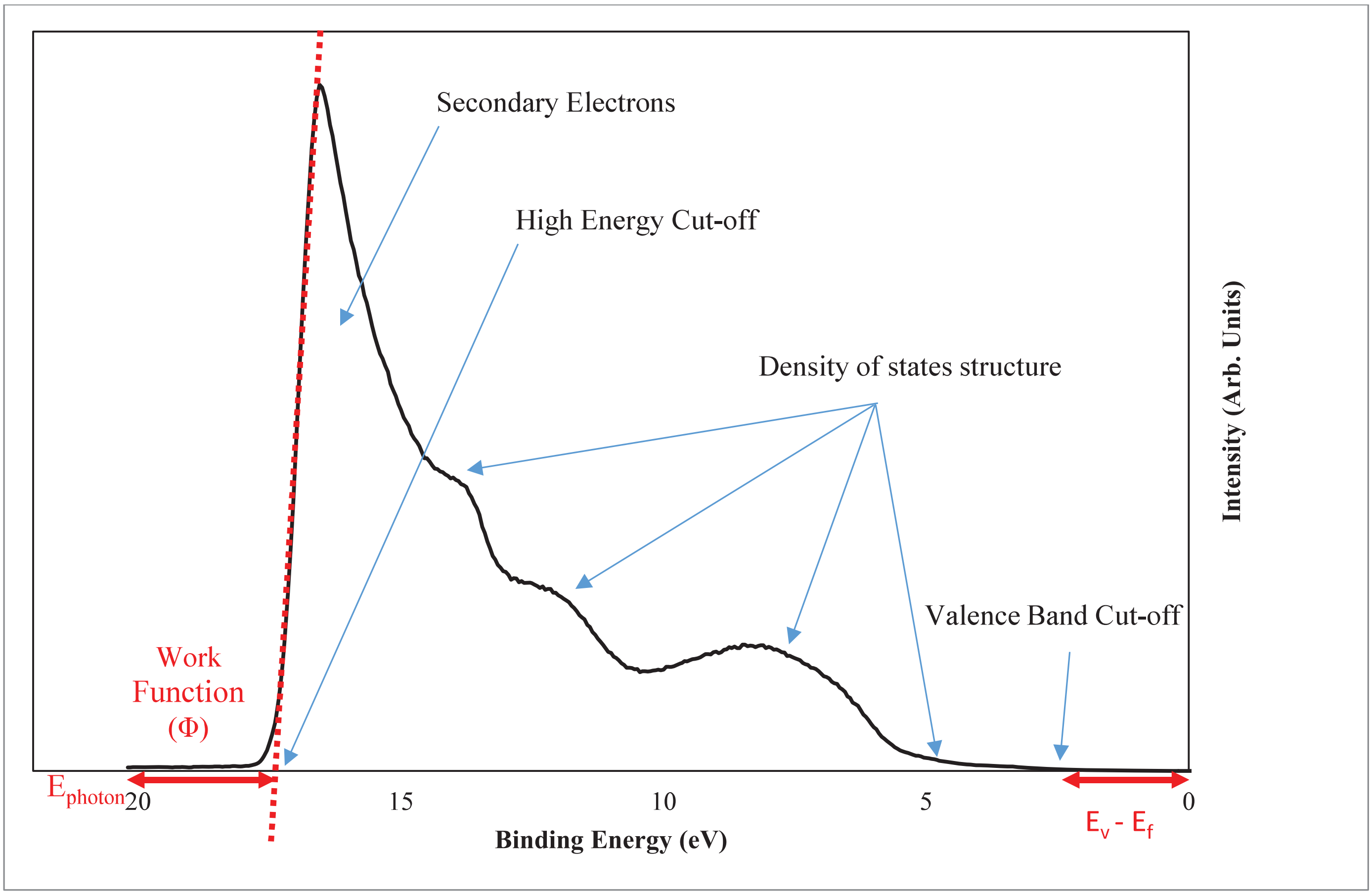

Figure 2–2: An example of an ultraviolet photoelectron spectrum with labelled points of interest

2.3. X-Ray Photoelectron Spectroscopy

X-ray photoelectron spectroscopy (XPS) examines the kinetic energy of photoelectrons ejected from the core and valence bands as a result of excitation using x-ray radiation. The core electrons provide information on the elemental composition of a surface. The orbitals within each element have a characteristic binding energy. X-rays from a magnesium MgKα source have a photon energy of 1253.6 eV which provides sufficient energy to liberate the core electrons from within the atoms. Reviewing Figure 2–1 the higher energy of the x-rays results in a deeper cross section meaning XPS is less surface sensitive than UPS, probing atoms up to 9 monolayers deep. Similar to UPS the binding energy of an electron can be calculated with the knowledge of the incident photon energy and the detected kinetic energy of the electrons ejected. XPS however does not utilise an additional 10 V bias as the energy supplied by electromagnetic radiation is more than enough to drive the photoelectric effect. Thus, using a MgKα source the binding energy of the detected electron can be calculated using the equation:

$$E_{binding} = 1253.6\ eV - E_{kinetic} - \Phi_{spectrometer}$$ *Equation 2-5*

Figure 2–3 is a survey XP spectrum of a single monolayer of graphene on a silicon substrate. A pass energy; the energy applied to bend the trajectory of incoming electrons is chosen to be 40 eV for survey measurements. The high pass energy is selected to allow for a high intensity signal that allows for quick scans with low dwell times. The survey spectrum is used as a preliminary scan to identify all elements present at the surface. Prominent peaks are identified with literature and higher resolution scans are made of these peaks if required. The higher resolution scans are made with lower pass energies, which reduces the intensity of the signal, and increasing the dwell time and number of scans. This assists in reducing the signal to noise ratio through an average of multiple scans and provides a smooth spectrum which may be modelled for examining specific elemental states, see Figure 2–4. An infinite number of components can be modelled; however each one needs to be justified. The least number of components are chosen; additional components can be included in cases where supplementary techniques can provide information to justify the decision. In some cases reviewing other core levels may assist in holistic characterisation. High resolution XP spectra were modelled with combined Gaussian-Lorentzian components and a correction for the Shirley background [4] using CasaXPS software.

An electron that is ejected from the surface without any interactions with surrounding atoms or electrons will have a measured kinetic energy equal to the excitation energy minus the energy lost to overcoming the binding energy. A large proportion of electrons will undergo inelastic collisions with surrounding atoms and therefore lose energy before being ejected and measured. The continuous increase in counts with higher binding energy observed in the survey spectrum presented in Figure 2–3 is a result of these inelastic collisions. Every ionisation of an atom produces the characteristic peaks and some inelastic background. The sum of inelastic background for the various interactions with different elements creates the large broad background signal.

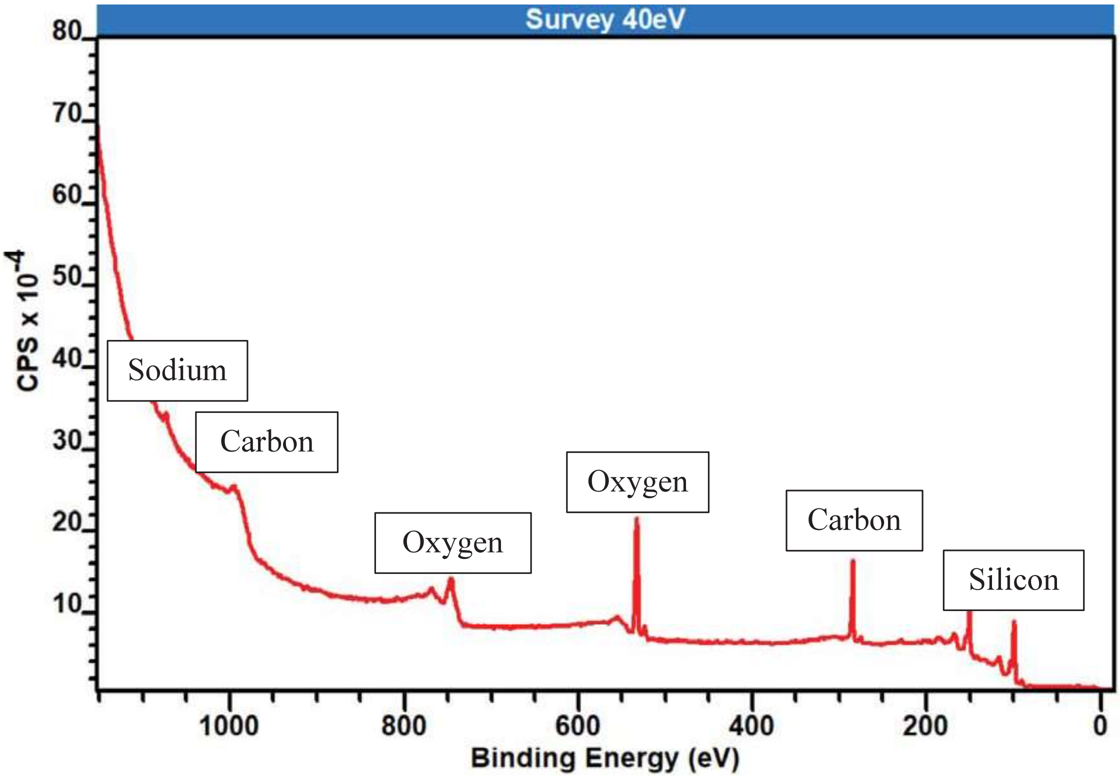

Figure 2–3: X-ray photoelectron spectrum survey scan run at 40 eV pass energy.

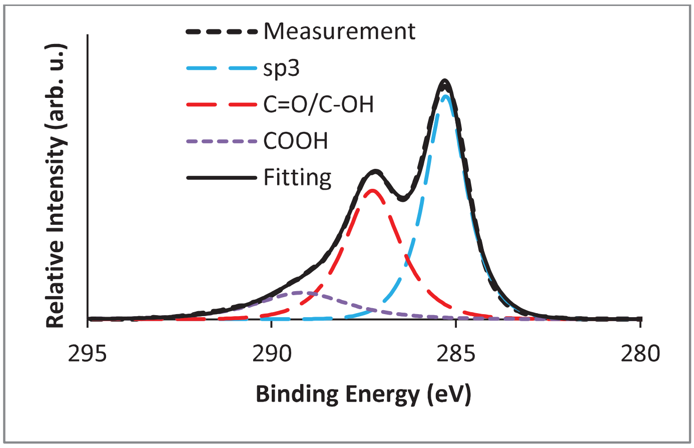

Figure 2–4: Example XP spectra of graphene oxide showing deconvolution of state analysis

From the XP spectra, the binding energy position, full width half maximum (FWHM) and the intensity of a peak can be determined. Every element has a specific characteristic peak position and comparing with reference data [5], the composition of the sample can be calculated. Any changes in the peak positions may indicate surface charging or bond changes. The FWHM of the peaks are related to the resolution of the measurement; which in some cases can be influenced by the composition. The intensity is related to the concentration of the element in the sample. A low intensity relative to the rest of the spectra indicates a low concentration and broad FWHM indicates that the resolution is low. If the resolution is too low, components within a signal such as oxidation states or other bound states may be difficult to model with confidence or justification. Using this information, the composition and relative elemental concentrations can be calculated. The intensity of a peak is calculated using:

$$Intensity = \frac{Peak\ area\ of\ component}{Atomic\ Sensitivity\ Factor\ of\ Element} \qquad \textit{Equation 2-6}$$

The sensitivity factors for all the XPS analysis are shown in Table 2-1.

Table 2-1: Atomic sensitivity factors used for XPS component calculations [5]

Element	Atomic Sensitivity Factors for XPS at 54.7° relative to the analyzer
Carbon 1s	0.296
Oxygen 1s	0.711
Silicon	0.339
Sodium	1.685
Molybdenum	3.321
Nitrogen	0.477
Sulfur	0.666

A sum of all component intensities is made and the percentage composition for each individual element can be determined as a percentage:

$$Percentage\ Composition = \frac{Specific\ Intensity}{Total\ Intensity} \times 100 \qquad \textit{Equation 2-7}$$

2.3.1. Angle Resolved X-Ray Photoelectron Spectroscopy

Angle resolved x-ray photoelectron spectroscopy (ARXPS) is a variation in the XPS procedure that allows one to obtain a concentration depth profile of a sample. Typically, an XPS measurement is conducted with the analyser normal to the sample surface (0˚), however in ARXPS one can run a series of measurements for different angles. By varying the angle between the analyser and the sample, the distance an electron travels through the solid is changed. Figure 2–5 illustrates a sample being analysed by a detector at various angles 0 - 60˚, the shortest path an electron takes to be seen by the detector is highlighted by the bold arrows; if the distance the photoelectron travels through the sample is greater than the electron mean free path, the chance of re-adsorption is high. Re-adsorption events are represented by the squared off arrows. Increasing the analysis angle, one increases the surface sensitivity of the measurement; through a series of consecutive measurements, the concentration depth profile can be determined.

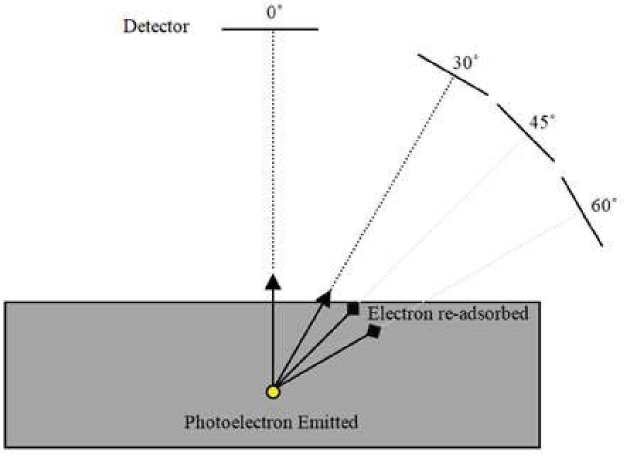

Figure 2–5: Illustration of ARXPS

The evaluation of the concentration depth profiling used similar algorithms described by Eschen et al. [6]. The measured intensity ratio (concentration of the element of interest) is compared to a fitted intensity, the concentration at various depths being the fitting parameter. With a minimisation in the difference between the measured and fitted intensity ratio the result is a concentration depth profile. The assumptions in the fitting procedure are; (a) The sample is compact up to the surface, i.e. there are no pores; variation in composition is not caused by density variations. (b) The substrate is homogeneous i.e. the mean free path is a constant value from the bulk to the surface. (c) The observation depth λ' varies linearly with cosθ (emission angle) (d) The substrate is infinitely thicker in comparison to the surface material, i.e. the change between the surface layer and the substrate is finite.

2.4. Metastable (Helium) Induced Electron Spectroscopy

In contrast to the previous photoelectron spectroscopic techniques which collect information with surface sensitivity in the order of a few nanometres from the surface; metastable helium induced electron spectroscopy is a true surface sensitive technique that only obtains information from the outer most layer of atoms. MIES is a spectroscopic technique that instead of using electromagnetic radiation, bombards the surface with metastable atoms that will interact with the outer most atoms to create an observable outcome. The atoms themselves are unable to exceed the Van der Waals interactions at the surface as such giving MIES true surface sensitivity [7]. Helium atoms are excited into meta-stable states (He^*) with an excitation of 19.8 eV and a lifetime of ~ 9000 s [8]. When the metastable helium atom approaches the surface, three possible interactions may occur. The three processes are illustrated in Figure 2–6 and Figure 2–7; provided the surface has an unoccupied state Φ_p the electron in the He^* outer orbital χ_b will tunnel into the surface resulting in a He^+ ion and the surface gaining an electron, this interaction is known as resonance ionisation (RI). The positive He^+ ion is neutralised by a process called Auger neutralisation (AN); an electron from the surface loses its energy to fill the vacant χ_a orbital neutralising the He atom and the solid gains the energy, an electron is then ejected from the solid with kinetic energy E_k. Combinations of the energy levels Φ_i and Φ_j are possible, leading to the broadening of features in the RI/AN spectra. The energy measured E_k for the RI/AN process is described by the equation:

$$E_k = E_i' - 2(\varepsilon + \Phi) \qquad \textit{Equation 2-8}$$

Where ε is the average binding energy of the electrons involved in the Auger process and E_i' is the ionisation potential of the He whilst Φ is the work function of the solid [8, 9]. The resonance ionisation process is hindered by the absence of unoccupied states Φ_p that allow the electron from the χ_b orbital to tunnel; this leads to a Auger deexcitation (AD). Auger deexcitation involves an electron from the surface Φ_i transferring to the inner vacant orbital χ_a of the He^* which then loses its electron from the outer orbital χ_b with energy E_k this time described by the equation:

$$E_k = E_i' - E_{binding} \qquad \textit{Equation 2-9}$$

Which should be highlighted allows the direct comparison of the AD components of MIES with UPS; with the exception the MIES is perfectly surface sensitive.

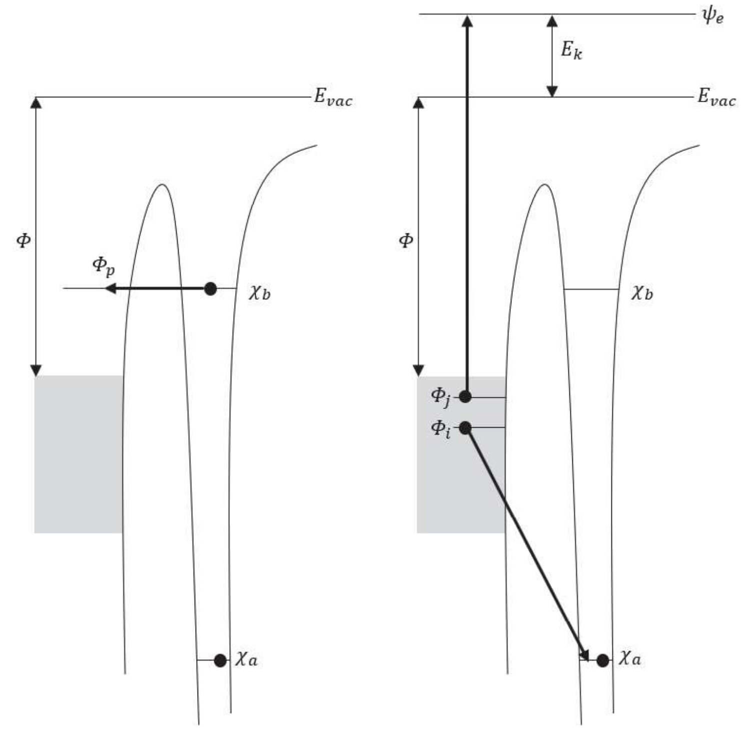

Figure 2–6: Resonance ionisation and Auger neutralisation process. Modified from Harada et al. [8] Adapted with permission from [8]. Copyright (2018) American Chemical Society.

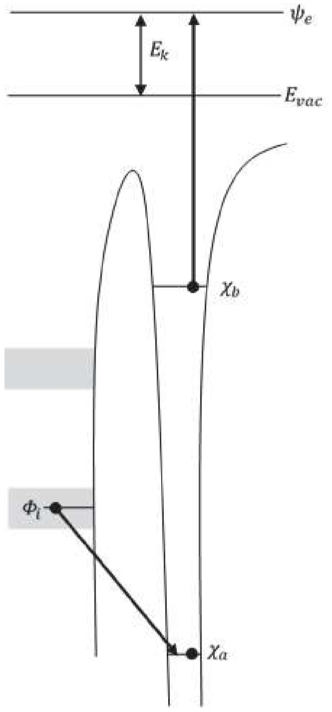

Figure 2–7: Auger deexcitation Process. Modified from Harada et al. [8]. Adapted with permission from [8]. Copyright (2018) American Chemical Society.

2.4.1. Singular Value Decomposition

Singular value decomposition (SVD) is used to evaluate a series of data and identify common components within a set of data. It is primarily used to separate the RI/AN and the AD components from resultant spectra, however it can be used for any component that experiences change across a series of measurements.

The SVD algorithm is used to identify contributions to the spectra and to identify the reference spectra. The algorithm has two steps. First, the number of base spectra is determined; second, the shapes of the base spectra are modelled. The base spectra have only a mathematical and not necessarily a physical meaning, e.g. the intensity of a base spectrum could be negative which has no physical meaning. Secondly the reference spectra are reconstructed as a linear combination of the base spectra. Following the procedure used by Morgner et al. [9] the base spectra form a matrix and is multiplied by an (n × n) matrix where n is the number of base spectra. The elements of the (n × n) are modelled with 2 criteria; all reference spectra are positive and all measured spectra must be fitted with a linear combination of the reference spectra as described by Equation 10:

$$S_i = \sum_n a_n S_n^r \qquad \textit{Equation 2-10}$$

where S_i is the measured spectrum, S_n^r are the reference spectra and a_n are the weighting coefficients. The sum of weighting coefficients should add up to unity: ($\sum_n a_n \approx 1$).

2.5. Auger Electron Spectroscopy and Scanning Electron Microscopy

Auger Electron Spectroscopy (AES) is a similar spectroscopic technique to XPS with the advantage of possessing high spatial resolution. The surface is irradiated with an electron beam with 1-20 keV which excites the surface and results in the ejection of electrons [10]. The process is described by the following equations [11]:

$$A + e_i^- = A^{+*} + e_i'^- + e_A^- \qquad \textit{Equation 2-11}$$

An incident electron e_i^- interacts with an atom A, $e_i'^-$ is the same incident electron after the interaction where it imparts enough energy onto an inner orbital electron e_A^- to eject it from the atom making it an excited ion A^{+*}. The excited atom can relax via two pathways:

$$A^{+*} = A^{++} + e_A^- \qquad \textit{Equation 2-12}$$

$$A^{+*} = A^{++} + h\upsilon_f \qquad \textit{Equation 2-13}$$

In Equation 2-12, an electron from a higher orbital relaxes into the hole produced in Equation 2-11, the energy is transferred to an adjacent electron which is then ejected e_A^- leaving an ion A^{++}, the ejected electron is known as an Auger electron. In Equation 2-13 instead of emitting an Auger electron, a photon $h\upsilon_f$ can be released.

Auger electron spectroscopy examines the kinetic energy of the Auger electrons which possess energy E_k. E_k is independent of the incident electron energy that was used to create the vacancy for the Auger process to occur. The spectra for AES are presented as energy vs derivative counts in an attempt to emphasise the low intensity peaks and normalise the high background radiation. For atoms with atomic numbers smaller than 10, the Auger emission is a dominating process, however for larger atomic numbers the fluorescence described in Equation 2-13 begins to dominate, reducing its effectiveness at compositional analysis in comparison to XPS. The key advantage of AES is its ability to focus the electron beam onto the surface such that specific locations are probed providing compositional information with high spatial resolution.

Whilst AES detects the Auger electrons, scanning electron microscopy (SEM) detects backscattered and secondary electrons. The secondary electrons receive a small amount of energy from the incident electrons, as such have a limited range of less than a few nanometres [12]. The electron beam is rastered across the surface and the intensity of the secondary electrons is recorded for each position. An image of the surface is formed by plotting the intensity, representing the quantity, of secondary electrons detected across the position of the sample surface. Utilising the secondary electron signal, SEM provides information on the topography of a samples surface with high spatial resolution. The resolution is dependent on the diameter of the beam diameter; the electron beam can be focused to diameters of 2 - 10 nm [11].

2.6. Raman Spectroscopy

Raman spectroscopy involves the illumination of a sample using a monochromatic laser, in the case of these investigations a laser of wavelength 532 nm with less than 5 mW power is used. Illuminating a molecule with radiation can result in various types of scattering. Figure 2–8a illustrates the absorption of a photon with energy E = hv, exciting the molecule to a virtual energy state; the energy applied is deliberately low to avoid excitation to absorption states which would result in fluorescence. Upon relaxation a photon of equal energy (E = hv) is reemitted and the molecule relaxes to its initial state. This is known as Rayleigh scattering or elastic scattering as no energy is lost during the collision of photons and molecules [13]. Inelastic scattering can also occur with the photon emitted having a different energy to the excitation photon. In Figure 2–8b the energy of the reemitted photon is E = hv - ΔE where ΔE corresponds with the difference in vibrational levels. ΔE can be positive or negative, when ΔE is positive the molecule has gained vibrational energy and the reemitted photon has less energy than the excitation photon; this is known as Stokes scattering. When ΔE is negative, the reemitted photon has more energy than the excitation photon and is a result of the molecule relaxing to a lower vibrational state than it was previously in, this is known as anti-Stokes scattering [11].

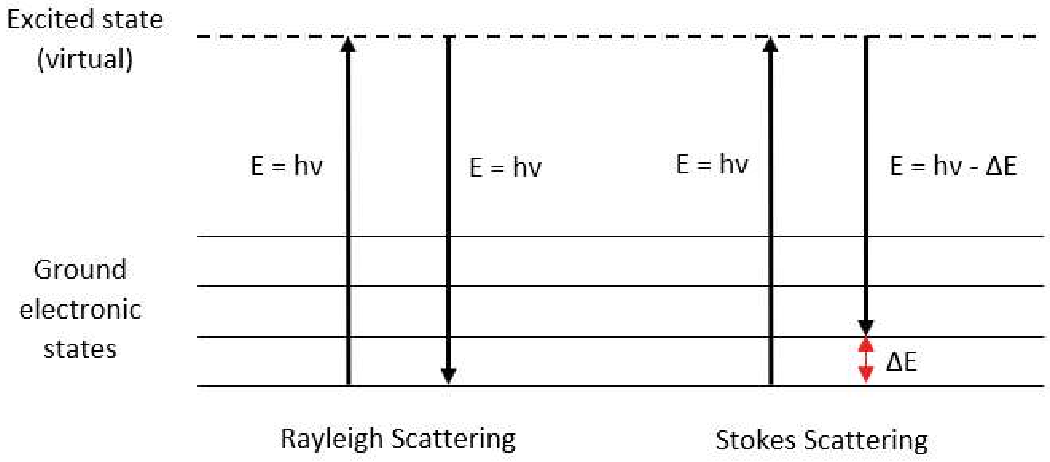

Figure 2–8: Illustration of (a) Rayleigh and (b) Stokes scattering

Plotting the shifted intensity versus the frequencies results in a Raman spectrum. Characteristic peaks correspond to specific energy levels of functional group vibrations allowing specific bonds to be determined. Raman spectroscopy is therefore a powerful tool for characterisation of the composition, types of bonds and in some cases thickness of films [14-16].

2.7. Optical Microscopy

In some cases, an optical image of the surface provides spatial information that aids in the understanding of other collaborative methods. Standard optical light reflected off the surface of a sample is focused through a series of lenses to magnify to a required level and the image is recorded with a digital camera.

2.8. Atomic Force Microscopy

Atomic force microscopy, a technique first proposed by Binnig et al. in 1986 [17], uses a very small tip with diameters as small as 2 nm on the end of a cantilever spring to probe the surface of interest [18]. The schematic for an AFM setup is shown in Figure 2–9, the instrument is composed of a laser source than projects light onto the backside of a cantilever, the reflected light is measured by a position sensitive detector which identifies how much the cantilever flexes. The tip attached to the cantilever will raster across the surface of a sample following the topography, any forces experienced by the tip will act on the cantilever and hence be measured by the detector. The sample sits on a piezoelectric manipulator which allows control of the samples position within a few nanometres. The detector and the piezoelectric manipulator are linked such that the deflection of the cantilever (force between tip and sample) is maintained, the variation in voltages are plotted as a function of position to produce an image of the surface topography.

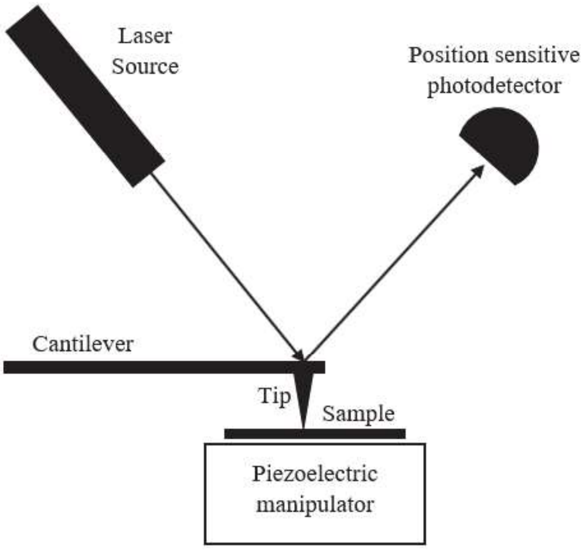

Figure 2–9: Schematic of AFM setup

Atomic force microscopy has 3 separate methods: contact mode, tapping mode non-contact and tapping mode contact. Contact mode drags the tip along the surface with a constant force controlled through the feedback loop. Contact AFM can be problematic for the lifetime of the tip and can also result in the destruction of the sample structure; as such, the tip can be oscillated such that at the tip briefly taps the surface at the maxima of its oscillation. Through tapping mode, the frictional forces found in contact mode can be minimised allowing the sample and tip to be preserved. A piezo, a crystal that expands when a voltage is passed through it, is used to oscillate the cantilever and hence the tip near the surface. As the tip approaches the surface it experiences resistance and the cantilever bends. Using the photodetector, a plot of force vs position can be made. The alternative mode of operation is non-contact operation where the tip is held a few nanometres above the surface where it experiences Van der Waals attraction. Given the attractive forces are weak, the forces are determined using AC detection techniques, allowing any resistance in the driven oscillation to be plotted with position.

2.9. References

1. Einstein, A., *Concerning an heuristic point of view toward the emission and transformation of light.* Annalen der Physik, 1905(17): p. 132-148.
2. M. P. Seah and Dench, W. A., *Quantitative electron spectroscopy of surfaces: a standard data base for electron inelastic mean free paths in solids.* Surface and interface analysis, 1979. **1**(1): p. 2-11.
3. Sze, S. M. and Ng, K. K., *Physics of semiconductor devices*, ed. Wiley. 1985, New York.
4. Shirley, D. A., *High-Resolution X-Ray Photoemission Spectrum of the Valence Bands of Gold.* Physical Review B, 1972. **5**(12): p. 4709-4714.
5. Chastain, J. and Moulder, J. F., *Handbook of x-ray photoelectron spectroscopy: a reference book of standard spectra for identification and interpretation of XPS data*. 1995: ULVAC-PHI, Incorporated.
6. Eschen, F., Heyerhoff, M., Morgner, H., and Vogt, J., *The concentration-depth profile at the surface of a solution of tetrabutylammonium iodide in formamide, based on angle-resolved photoelectron spectroscopy.* Journal of Physics: Condensed Matter, 1995. **7**(10): p. 1961.
7. Morgner, H., *The characterization of liquid and solid surfaces with metastable helium atoms*, in *Advances In Atomic, Molecular, and Optical Physics*, Benjamin, B. and Herbert, W., Editors. 2000, Academic Press. p. 387-488.
8. Yoshiya Harada, Masuda, S., and Ozaki, H., *Electron spectroscopy using metastable atoms as probes for solid surfaces.* Chemistry Review, 1997. **97**(6): p. 1897-1952.
9. Morgner, H., *The quantitative characterization of liquid and solid surfaces with metastable helium atoms.* AIP Conference Proceedings, 2000. **500**(1): p. 687-698.
10. Hofmann, S., *Auger- and x-ray photoelectron spectroscopy in materials science*. 2013, Berlin, Heidelberg: Springer.
11. Skoog, D., Holler, F., and Crouch, S., *Principles of instrumental analysis*. 2007, Belmont, CA: Thomson Higher Education.
12. Wilson, M., *Nanotechnology : basic science and emerging technologies*. 2004, Boca Raton: Chapman & Hall/CRC.
13. Ferraro, J. R., Nakamoto, K., and Brown, C. W., *Introductory Raman spectroscopy*. 2003, San Diego, UNITED STATES: Elsevier Science & Technology.
14. Ferrari, A. C., Meyer, J. C., Scardaci, V., Casiraghi, C., Lazzeri, M., Mauri, F., Piscanec, S., Jiang, D., Novoselov, K. S., Roth, S., and Geim, A. K., *Raman spectrum of graphene and graphene layers.* Physical Review Letters, 2006. **97**(18): p. 187401.
15. Malard, L. M., Pimenta, M. A., Dresselhaus, G., and Dresselhaus, M. S., *Raman spectroscopy in graphene.* Physics Reports, 2009. **473**(5–6): p. 51-87.
16. Changjian, Z., Richard, S., Zachary, B., Yihan, C., Salahuddin, R., Anshul, A. V., Mansun, C., Yang, C., and Cary, Y. Y., *Synthesis and interface characterization of CNTs on graphene.* Nanotechnology, 2017. **28**(5): p. 054007.
17. Binnig, G., Quate, C. F., and Gerber, C., *Atomic force microscope.* Physical Review Letters, 1986. **56**(9): p. 930-933.
18. Cheung, C. L., Hafner, J. H., and Lieber, C. M., *Carbon nanotube atomic force microscopy tips: direct growth by chemical vapor deposition and application to high-resolution imaging.* Proceedings of the National Academy of Sciences of the United States of America, 2000. **97**(8): p. 3809-3813.

Chapter 3

3. Aims and Scope

The development of complex systems from smaller subsystems is known as a bottom up approach. This approach is becoming more prevalent in research, giving rise to nanomaterials and nanotechnology. The importance of researching 2D materials is paramount in developing devices that perform to optimal specifications or improve existing devices. Solid state physics allows crystalline structures to be investigated and form an understanding of the physical properties that materials possess. The materials discussed and investigated in this dissertation are: graphite, graphene, graphene oxide, carbon nanotubes and molybdenum disulphide. The scope originally focussed on carbon materials, however collaborations were continued extending the scope to TMDCs.

The aim of this dissertation is to characterise 2D materials using surface sensitive instrumentation. The characterisation of the electronic and compositional properties of materials and their outermost surfaces will assist in optimising fabrication methods for device development; through improving surfaces used within device interfaces, the performances of devices increase.

The thesis is structured in the following manner:

The electronic structure and composition of graphene oxide is characterised with varying preparation conditions to optimise the electronic performance of the material. Desirable fabrication conditions are determined. (It should be noted that this chapter has been published and is a reformatted version.)

A novel method for exclusively examining the DoS of 2D graphene using MIES is explored. It is demonstrated that the AD components within the spectra can be separated and allow for the determination of DoS for only outermost atoms of a surface; a direct quantitative study of the surface energy levels. (It should be noted that this chapter has been published and is a reformatted version.)

Using the developed method for characterising 2D carbon materials using MIES, a concept for separating the density of states for the inner and outer walls for double wall carbon nanotubes is discussed. Through a comparison of UPS and MIES, which possess different surface sensitivity; a novel method that aims, for the first time, to measure the DoS of the internal CNTs is explored. (It should be noted that this chapter has been published and is a reformatted version.)

The electronic properties of 2D MoS_2, a TMDC, is explored with previously developed spectroscopy methods. With an initial aim to characterise the electronic structure of monolayer MoS_2 and compare to incrementally increased layers thickness. Due to sample availability and quality, challenges were encountered; the chapter discusses the characterisation of non-homogeneous thin films. (It should be noted that this chapter is the only results chapter that has not yet been published. As such the structure of the chapter may contrast with the previous chapters.)

Chapter 4

4. Experimental

To avoid repeating experimental details throughout each chapter, necessary experimental details will be presented here and referred to in subsequent chapters. Unique experimental details or modifications to the details described in this chapter will be presented with context within the relevant chapters.

4.1. UPS, MIES and XPS

UPS, MIES and XPS are conducted in an ultra-high vacuum (UHV) system built by SPECS (Berlin, Germany) with a base pressure of a few 10^{-10} mbar. A two stage cold cathode gas discharge from MFS (Claustal-Zellerfeld, Germany) is used to simultaneously generate UV light (He I line) and He*. A non-monochromatic x-ray source (Mg Kα) is used to generate Kα radiation. The emitted electrons are detected via a hemispherical Phoibos 100 energy analyser from SPECS (Berlin, Germany). UPS, MIES and XPS are conducted with a pass energy of 10 eV. A bias of -10 V was applied to the samples during UPS and MIES measurements to ensure complete emission of secondary electrons. The angle of UV and x-ray source radiation and the analyser are both 54° with respect to the sample normal.

4.2. In Situ Sample Heating

Heating of samples in situ in UHV facilitates water desorption and the removal of adventitious carbon. A filament located under the sample holder is used for heating, powered by a 3 A power supply. Sample surface temperatures reach up to 750 K depending on the filament installed; variations in the filament thickness and length result in changes in its heating behaviour. Cooling of the sample was achieved using a gas line carrying nitrogen with a segment of coil being submerged in liquid nitrogen. This allowed the sample to be cooled to a minimum of 93 K. The heating process took approximately 30 mins to safely reach maximum temperature and was held for a minimum of 10 mins to ensure maximum desorption.

4.3. Raman Spectroscopy

Raman spectra were acquired using a WITec alpha 300R Raman microscope at an excitation laser wavelength of 532 nm (≤ 5 mW) with a ×40 objective (numerical aperture 0.60). Typical integrations times were 10 - 30 seconds for 2 - 3 accumulations per spectrum.

Chapter 5

5. Examining the Electrical and Chemical Properties of Reduced Graphene Oxide with Varying Annealing Temperatures in Argon Atmosphere

This chapter is a reformatted version of the paper published in:

Applied Surface Science 356 (2015) 719–725.

Author Contribution:

Benjamin Chambers: Designed and performed experiments, data analysis, interpretation and prepared manuscript.

Marco Notarianni: Sample preparation, AFM and four-point probe measurements, provided sample preparation details for manuscript, revision of manuscript.

Jinzhang Liu: Intellectual contribution to sample preparation.

Nunzio Motta: Revision of manuscript.

Gunther Andersson: Intellectual contribution in conceptualising experiments, data interpretation and revision of manuscript.

Chapter 5 has been removed due to copyright restrictions

Chapter 6

6. The direct measurement of the electronic density of states of graphene using metastable induced electron spectroscopy

This chapter is a reformatted version of the paper published in:

2D Materials, 2017. 4(2) p. 025068

Author Contribution:

Benjamin Chambers: Designed and performed experiments, data analysis, interpretation and prepared manuscript.

Christof Neumann: Sample preparation.

Andrey Turchanin: Sample preparation, revision of manuscript.

Christopher Gibson: Performed Raman measurements and provided experimental details for manuscript, revision of manuscript.

Gunther Andersson: Intellectual contribution in conceptualising experiments, data interpretation and revision of manuscript.

Chapter 6 has been removed due to copyright restrictions

Chapter 7

7. Measuring the Density of States of the Inner and Outer Wall Double-Walled Carbon Nanotubes

This chapter is a reformatted version of the paper published in:

Nanomaterials 2018, 8(6), 448

Author Contribution:

Benjamin Chambers: Designed and performed experiments, data analysis, interpretation and prepared manuscript.

Cameron Shearer: Sample preparation, provided sample preparation details for manuscript, revision of manuscript

LePing Yu: Sample preparation.

Christopher Gibson: Performed Raman measurements and provided experimental details for manuscript, revision of manuscript.

Gunther Andersson: Intellectual contribution in conceptualising experiments, data interpretation and revision of manuscript.

Chapter 7 has been removed due to copyright restrictions

Chapter 8

8. Molybdenum Disulphide Thin Films

8.1. Abstract

Thin films of MoS_2, fabricated using CVD, are characterised using a combination of ultraviolet photoelectron spectroscopy, x-ray photoelectron spectroscopy, metastable helium induced electron spectroscopy, optical microscopy, Raman spectroscopy, Auger spectroscopy and scanning electron microscopy. The coverage of the MoS_2 was found to be less than 50 % of the total area, with the thickness of the film varying between monolayer and bulk; 80 % of the film is multilayer, thus is classified multilayer MoS_2 in comparison with the bulk reference. The DoS of the film was measured using UPS and compared with a reference bulk crystal MoS_2. Differences between the multilayer MoS_2 and the bulk MoS_2 spectra included the shape of the features and change in Fermi cut offs; broad features with a low Fermi edge for bulk MoS_2 and sharper features with a higher Fermi edge cut off for the thin film, indicating that thin film has a larger bandgap than the bulk material.

8.2. Introduction

MoS_2 is an example of a transition metal dichalcogenide that possesses an indirect bandgap of 1.29 eV as a bulk or multilayer material [1]. Reducing the thickness of the material to a monolayer will result its bandgap increasing to 1.89 eV [2]. Having a bandgap, in comparison to graphene's zero bandgap, makes the material suitable for semiconducting devices that require specific bandgaps. In addition to possessing a suitable bandgap, it has been reported that with a fine control over the number of deposited MoS_2 layers [3], the work function of a surface may be tuned [4] allowing for surfaces to be tuned for specific interfacing; decreasing the number of layers results in an increase in the band gap [5].

In Chapter 6 graphene samples fabricated by University of Jena proved to ideal 2D material for spectroscopic studies. The same research group had indicated that similar CVD fabrication methods for polycrystalline MoS_2 films were being researched. This provided an opportunity to explore surface sensitive studies of the 2D MoS_2 with controlled growth and characterise the changes in the DoS of the surface with variations in thickness.

Spectroscopy of MoS_2 aims to characterise the composition and electronic properties, however methods such as UPS and XPS typically probe deeper than the 2D material and detect signals from a combination of the desired material and the substrate. It has previously been demonstrated for carbon materials that MIES is an invaluable spectroscopic method for measuring the DoS of 2D materials whilst excluding the substrate electronic structure. Thus an experiment is designed to investigate the DoS of MoS_2 films.

8.3. Experiment design

Similar to the graphene sample that had been fabricated in Jena a MoS_2 sample was grown using chemical vapour deposition [6, 7] and transferred onto 285 nm silicon dioxide wafers supplied. The silicon dioxide sent to Jena had favourable conductivity for spectroscopy (Si P-type, B doped, $R= 0.005\ \Omega\text{cm}$), that has low resistance to avoid charging of the surface. A sample of monolayer MoS_2 was requested with plans to further examine multilayer MoS_2 samples following initial results of the monolayer sample. Comparing samples of increasing number of layers would allow for characterisation of DoS or work function changes [5, 8, 9].

8.4. Initial Method

8.4.1. Materials

Samples were requested to be prepared on 10 × 10 mm silicon wafers however a sample of 10 × 10 mm on a 20 × 20 mm silicon was received. Figure 8–1a is an approximate illustration of the sample received and the lines (Figure 8–1b) used to cut to create sample capable of being analysed; the least number of cuts were used to avoid damaging the sample and rendering it unusable. The orientation of the silicon (100) would not allow for diagonal cuts to maximise MoS_2 area, as such the resultant MoS_2 on silicon is illustrated in Figure 8–1c; a portion of the original MoS_2 sample.

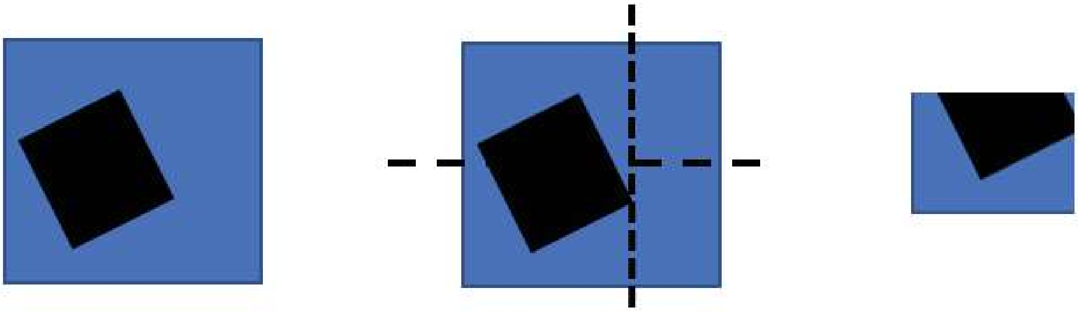

Figure 8–1: (a) Sample of MoS_2 (Black) on substrate (Blue) (b) lines cut (c) resultant sample for analysis

8.4.2. UPS and MIES

Experimental details discussed in Section 4.1. The analysis area for UPS, MIES and XPS is typically 2 mm in radius, however this sample preparation introduced a challenge; given the substrate cut was roughly 11 × 9 mm and the MoS_2 sample was of an irregular shape and off centre. The analysis spot would likely include a large proportion of bare substrate; to maximise the signal from the single monolayer of MoS_2 a different analysis mode would be required.

An alternative method of analysing the surface was designed; instead of using a single centred measurement, a series of positions would be measured 1 mm apart in a 3 × 3 grid for a total of nine analysis spots, the positions used are presented in Table 8-1, with the corresponding labels used in Table 8-2. A small area, medium magnification lens mode was used such that each analysis area was approximately 0.7 mm in radius. Examining a series of data collected in this manner allows regions dominated by MoS_2 or substrate to be identified and confirm which areas analysed are desirable for characterisation.

Table 8-1: A matrix of the positions (x, z), where y is at a constant

13, 24	13, 23	13, 22
14, 24	14, 23	14, 22
15, 24	15, 23	15, 22

Table 8-2: Labels for positions

1	2	3
4	5	6
7	8	9

8.4.3. Heating Procedure

Experimental details discussed in Section 4.2.

8.5. Initial Results

Initial UPS and MIES measurements for the various positions are illustrated in Figure 8–2 and Figure 8–3; cropped for comparison at lower intensities. No features between 0 - 6 eV are observed in either the UPS or the MIES. The shape of the UP spectra is similar to silicon with adventitious carbon for all positions with X = 14 and 15. In the UP spectra, positions with X = 13 have a different shape, with reduced intensity and remain featureless between 0 - 6 eV, this region may be unaffected by the MoS_2 deposition and also has a thin film of adventitious carbon on silicon.

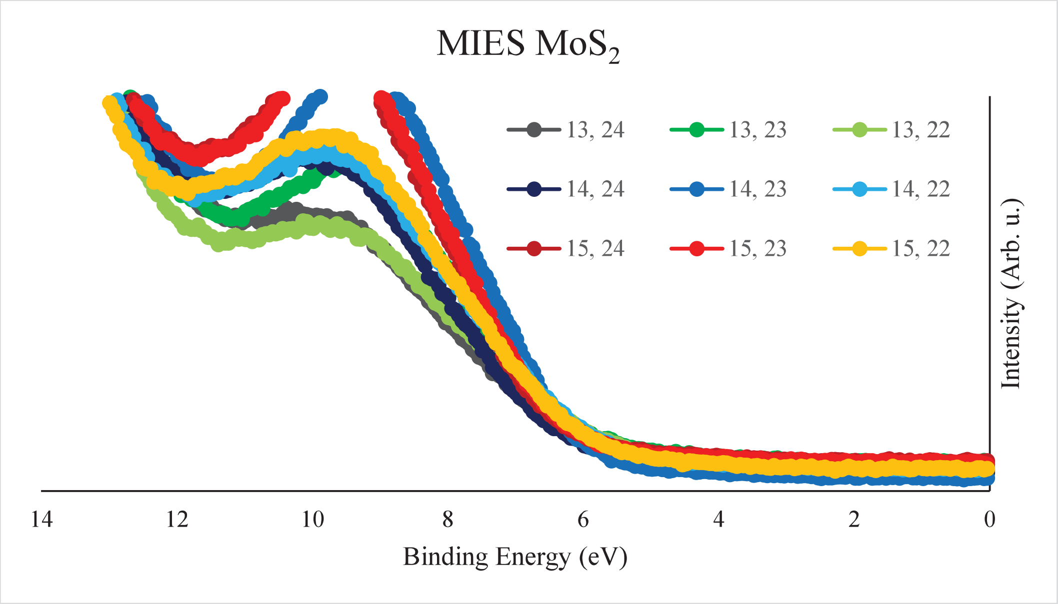

Figure 8–2: MIE spectra for MoS$_2$ for all positions 1-9

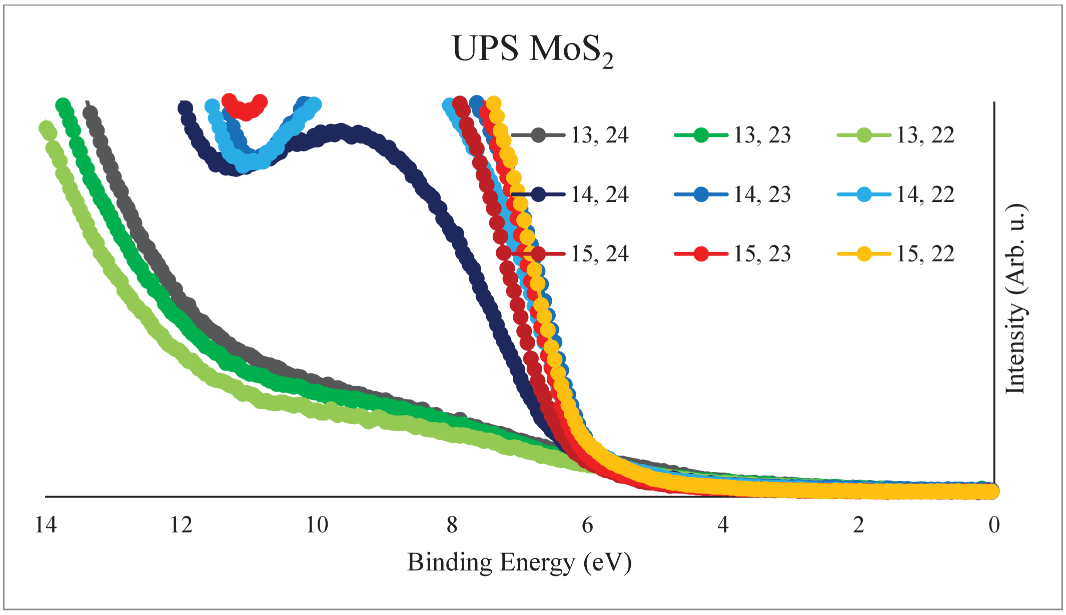

Figure 8–3: UP spectra for MoS$_2$ for all positions 1-9

XPS is used to examine the composition of each position. Figure 8–4 is a compositional summary of each location with the numerical values shown in Table 8-3. The silicon and oxygen content seem to remain consistent across the sample. Position (15, 22) is an exception that has a higher carbon and oxygen concentration indicating contamination. The molybdenum and sulphur concentrations are low with concentrations not exceeding 2.6 % and 4.8 % respectively. The silicon concentration across the sample, excluding position (15, 22), ranges from 41.8 % to 47.6 % indicating either sparse MoS$_2$ coverage or the concentration is low due to a low film thickness resulting in a low cross section. Previous measurements of monolayer graphene resulted in only 20 % silicon as such it is assumed, from this XPS summary, that the MoS_2 coverage is minimal. Reviewing the UPS this explains the lack of any features as it is mostly silicon with carbon contamination.

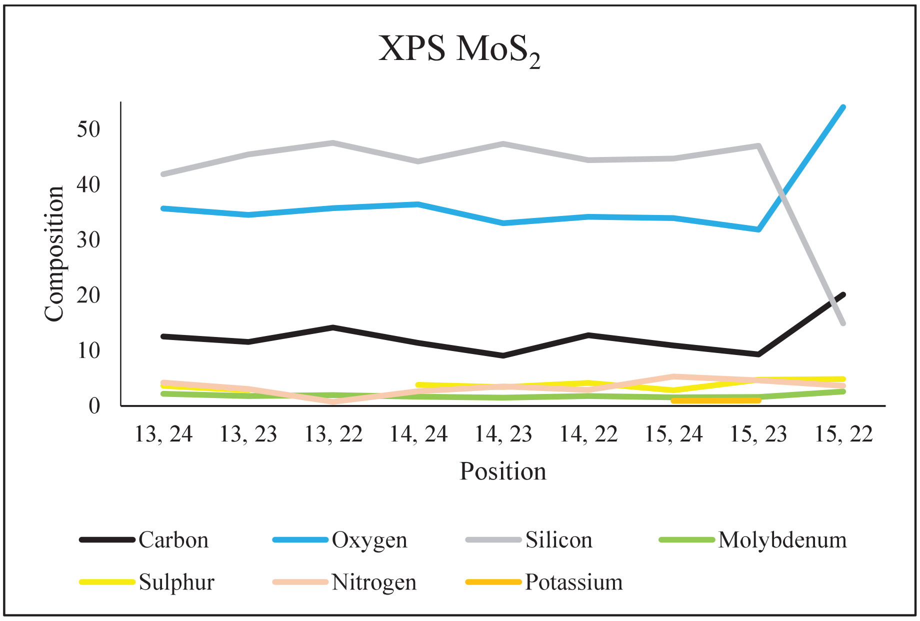

Figure 8–4: XPS composition for MoS_2 sample for positions 1-9

Table 8-3: XPS composition summary (relative concentration ratio % ± 0.2 %)

Position	1	2	3	4	5	6	7	8	9
	13, 24	13, 23	13, 22	14, 24	14, 23	14, 22	15, 24	15, 23	15, 22
Carbon	12.5	11.5	14.1	11.4	9.1	12.7	10.9	9.3	20.1
Oxygen	35.7	34.5	35.7	36.4	33.0	34.1	33.9	31.8	54.0
Silicon	41.8	45.5	47.6	44.2	47.4	44.4	44.7	47.0	14.9
Molybdenum	2.2	1.8	2.0	1.7	1.5	1.7	1.5	1.6	2.6
Sulphur	3.6	2.8		3.8	3.4	4.2	2.8	4.7	4.8
Nitrogen	4.2	3.1	0.7	2.7	3.5	2.8	5.3	4.6	3.6
Potassium		0.9			2.2		0.9	0.9	

8.5.1. Bulk MoS_2 Reference

A bulk sample of synthesised MoS_2 (BLK-MOS2-SYN) was purchased from 2D Semiconductors. Standard, medium area UPS and MIES were conducted on the sample across a temperature range similar to the investigation Morgner et al. had conducted with HOPG [10]. The MIE spectra presented in Figure 8–5b did not show any variation with temperature, indicating any changes in AD/AN interaction were independent of the temperature and remained consistent. It is also observed that the MoS_2 does not experience any prominent features in the MIES spectra. The lack of sharp features associated with Auger deexcitation indicates that it is dominated by resonance ionisation and Auger neutralisation; expected in semiconductors where the RI is not supressed [11]. A distinct structure in the UP spectra, Figure 8–5a, is observed for bulk MoS_2 between 0 eV and 7 eV, this is in agreement with literature [12].

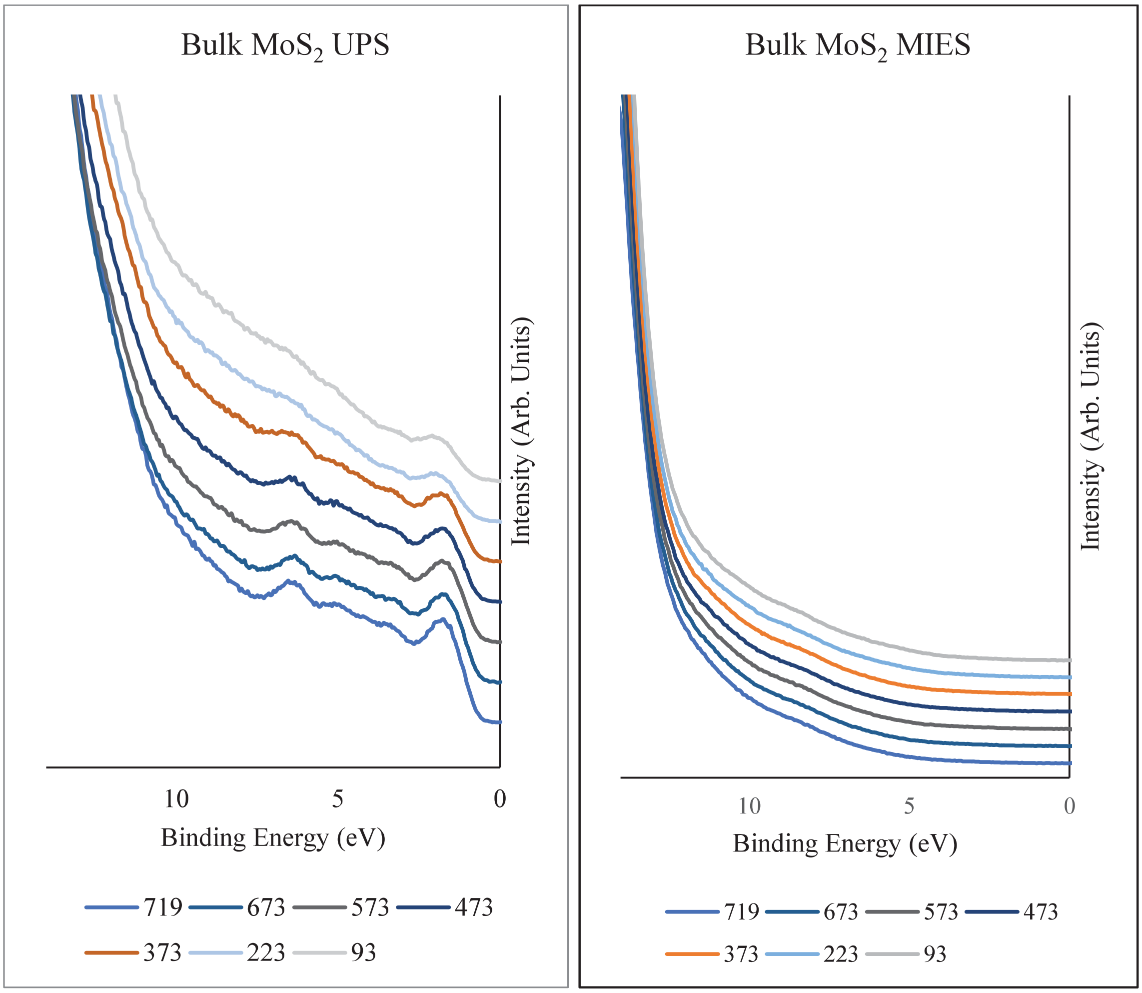

Figure 8–5: (a) UP and (b) MIE spectra for bulk MoS_2 across temperature range 93 K to 719 K

8.5.2. Summary of Initial Results

Reviewing the UP, MIE and XP spectra of the thin film MoS_2, it is difficult to identify the MoS_2 due to poor coverage. Comparing the UPS of the thin film MoS_2 with the reference bulk sample in Figure 8–6, the UP spectra exhibited no features between 0 eV and 6 eV that were present in the reference bulk MoS_2. The general structure looks similar to silicon with adventitious carbon. XPS of the thin film MoS_2 indicated that the relative concentration of Mo was less than 3 % confirming poor coverage of MoS_2.

After discussions with the research group in Jena, more samples were requested with 10 × 10 mm substrate with 10 × 10 mm sample to minimise uncovered substrate and increase the usable analysis area.

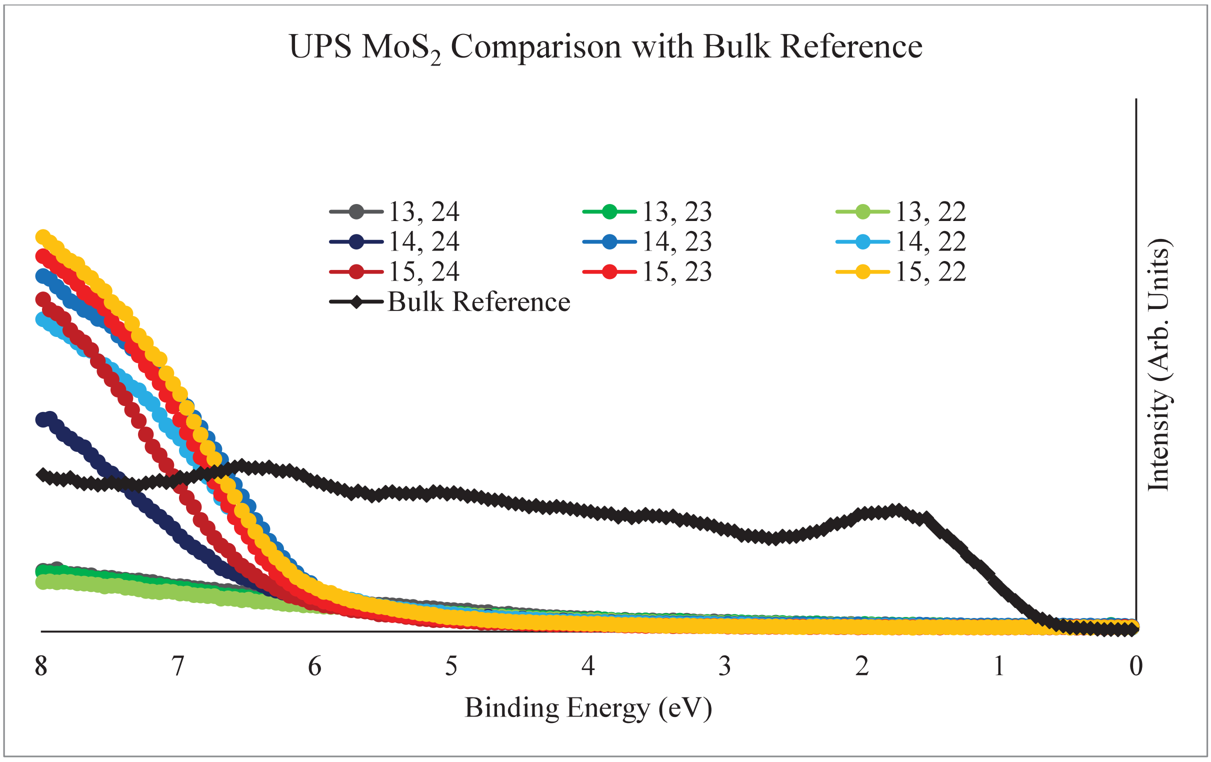

Figure 8–6: Comparison of UP spectra of bulk MoS_2 (at 719 K) and all positions of thin film MoS_2 sample

8.6. Revised Method

Using a similar method to that devised earlier; each position measured by XPS, UPS and MIES were separated by 2 mm, increased from 1 mm, such that no overlap of any two analysis spots occurred, the new positions are plotted in Table 8-4. The next series of measurements were conducted on a new sample consisting of a 10 × 10 mm silicon wafer with a MoS_2 sample area of approximately 5 × 5 mm; a photograph of the sample is presented in Figure 8–7. Measurements were conducted after heating to 723 K, once again to remove water or hydrocarbons that had adsorbed to the surface since fabrication.

Table 8-4: A new matrix of the positions (x, z), where y is at a constant 11 mm.

12, 25	12, 23	12, 21
14, 25	14, 23	14, 21
16, 25	16, 23	16, 21

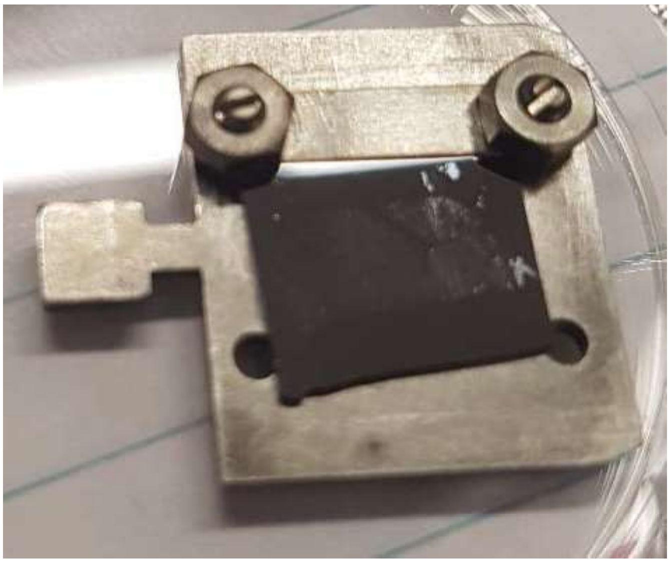

Figure 8–7: New sample received from Jena mounted on sample mount for UHV spectroscopy, bottom edge of sample is approximately 10 mm

8.7. Results

The XPS data presented in Figure 8–8 are in order of consecutive measurements. It is evident that the sample, measured over a period greater than 18 hrs, resulted in some adsorption of carbon within the UHV main chamber; the carbon concentration steadily increased over time, from a minimum of 9 % to a maximum of 26 %. This considerable increase was unexpected as previous samples have previously been left in the UHV chamber overnight and have not experienced any similar carbon adsorption. This sample could be experiencing this issue as only a portion of the sample surface is MoS_2, the remainder being silicon which possesses a high surface energy [13] and could experience this high carbon adsorption. Variation in carbon concentration will dominate any measured electronic structure, as such the measurements required a repeat whilst eliminating the carbon adsorption. To eliminate carbon variation with time, the sample is continually heated for the duration of the measurements. Typically, heating for long durations is limited to prolong the lifetime of the heating filament, however it is unavoidable in this circumstance, as such an exception was made.

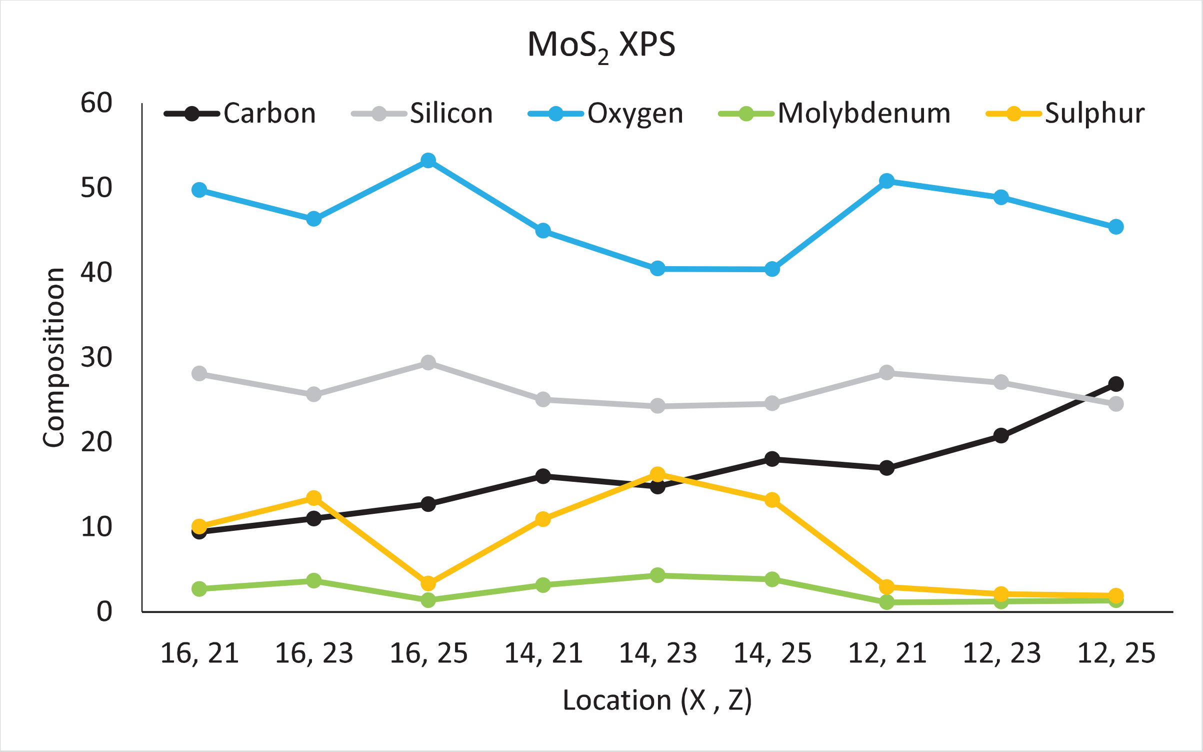

Figure 8–8: MoS_2 XPS composition presented in order of measurements

Prior to repetition of the measurements, it was noted that the MoS_2 concentration was extremely low for the X = 12 row which may have been close to the edge of the fabricated sample area. It was assumed that the area analysed may be bare silicon substrate and the position needed to be adjusted to centre onto the sample. The analysis positions were altered for the next series by 1 mm in the X plane; the updated positions can be found in Table 8-5.

Table 8-5: Updated matrix of positions

13, 25	13, 23	13, 21
15, 25	15, 23	15, 21
17, 25	17, 23	17, 21

The XPS data in Figure 8–9 is in order of labels (1-9), not in the order that each measurement was taken, that had previously been plotted. Repeating XPS measurements of MoS_2 with continuous heating resulted in a consistent carbon concentration, illustrated by the horizontal black line plotted in Figure 8–9, remaining between 8 % and 10 % with no proportionality to time. Reviewing Figure 8–9 the silicon remains relatively consistent across the sample, which is to be expected for a thin layer of MoS_2, as the thin film would not totally obscure the silicon from XPS.

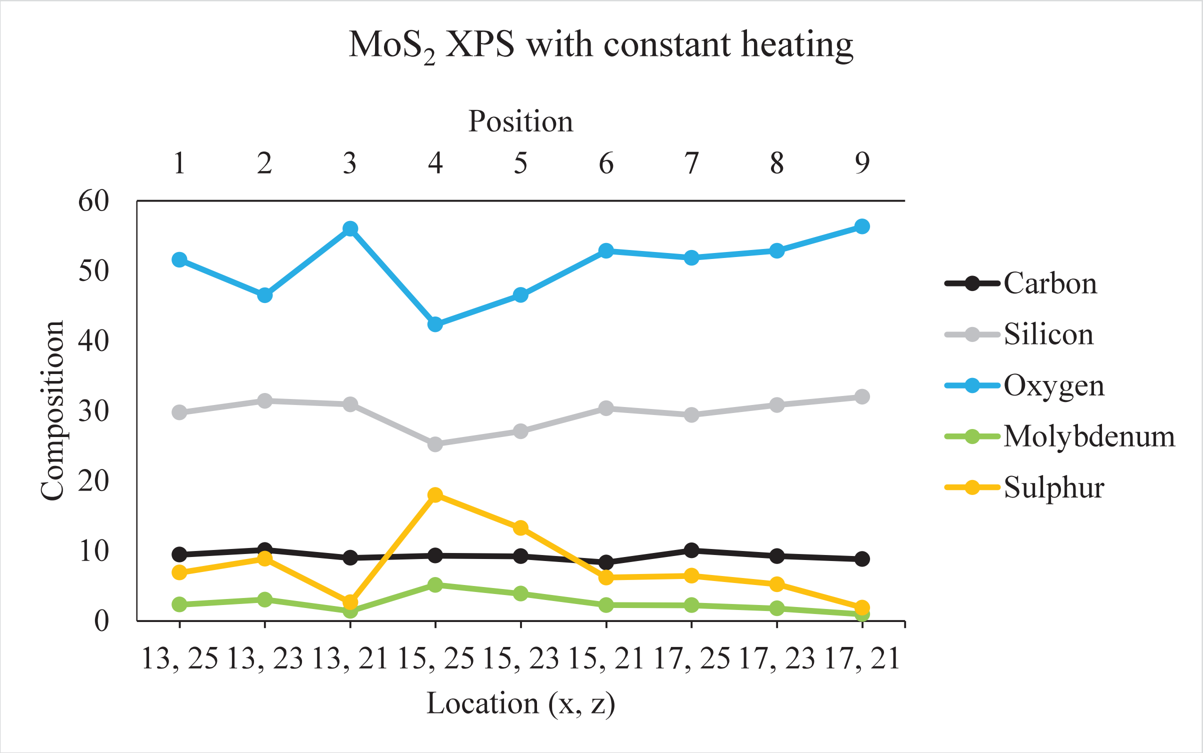

Figure 8–9: MoS_2 XPS composition in sequential order of labelling 1-9

Location 4 (15, 25) exhibits an increased MoS_2 concentration and a substantial drop in silicon concentration. There are two potential causes for this; either in comparison to the other locations this spot has the most coverage or this area possesses a thicker film such that it obscures more of the silicon substrate from the XPS.

The relative concentration of molybdenum at positions 4 and 5 are 5 % and 4 % respectively, highlighting that the areas of highest MoS_2 concentration exist at positions 4 and 5. The remaining positions range from concentrations of 1 % to 2 % of molybdenum. The oxygen correlates inversely with the MoS_2 such that the areas that are not covered by MoS_2 will have more oxygen species, most likely bound to the silicon or any adventitious carbon still left.

Similar to the bulk MoS_2 reference, MIES of the thin film MoS_2, presented in Figure 8–10, shows no distinct features; a result of its RI/AN dominance indicating the MoS_2 has unoccupied states for resonance that are spatially permitted with the metastable helium [11]. In order to compare UPS with MIES some AD contribution is required; the lack of features in the MIE spectra annuls the previous plan to identify the DoS for various layers of MoS_2 for varying thicknesses, as such only an average DoS for few layer MoS_2 can be made using UPS.

The UP spectra, presented in Figure 8–11, are displayed as a grid to represent the locations on the sample (1 - 9). The bottom left of the sample (position 7) has the strongest features between 6 eV and 0 eV whilst position 4 and 8 have similar features with less relative intensity. Position 5, the middle of the sample, appears to have less MoS_2 contribution than positions 4, 7 and 8. Examining the sample by eye, a vein is noticeable on the sample: an area of uncovered silicon. It is possible the analysis area of the UPS aligned with this vein such that a lower proportion of MoS_2 was examined. Positions 1, 2 and 3 have no prominent features relating to MoS_2 indicating that the position is not aligned with the MoS_2 sample, the area examined appears to be dominated by silicon substrate with adventitious carbon.

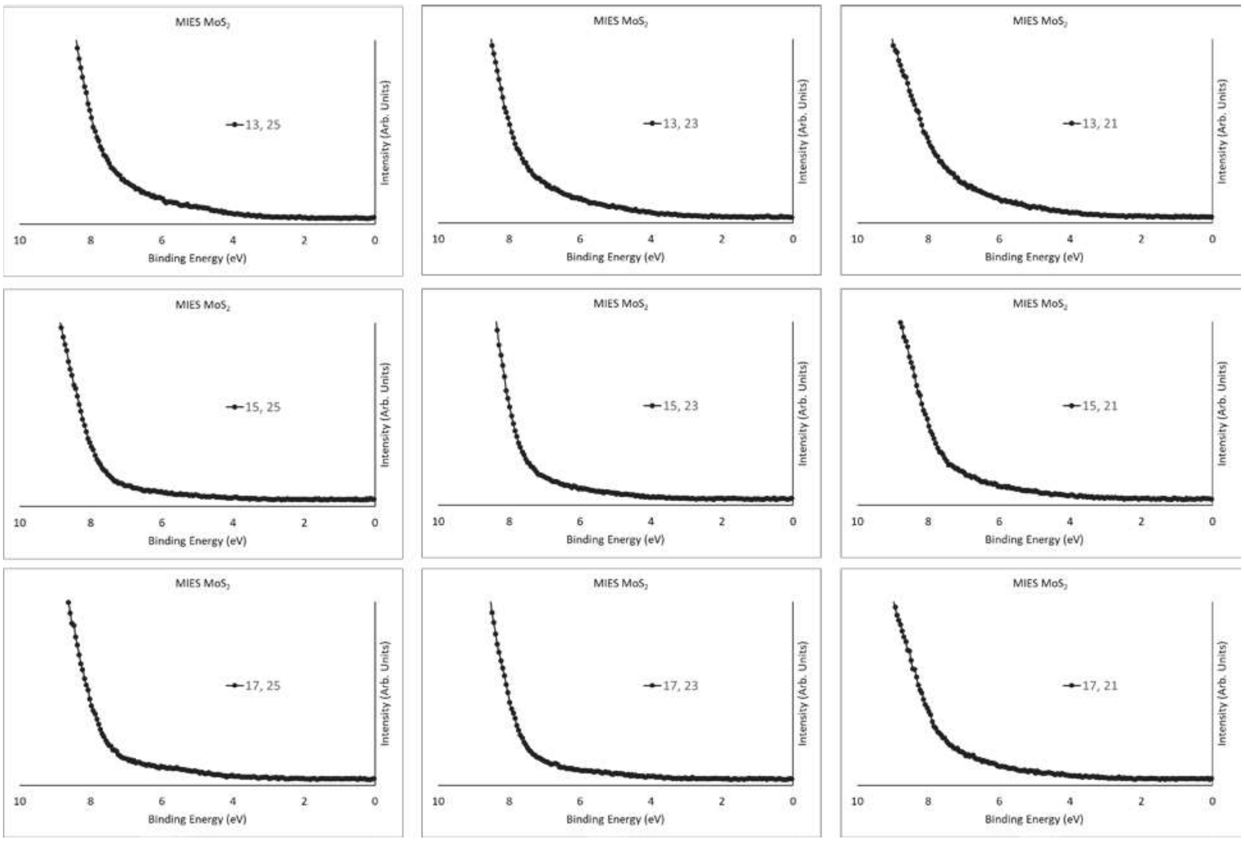

Figure 8–10: Thin film MoS$_2$ MIE spectra for all positions 1-9

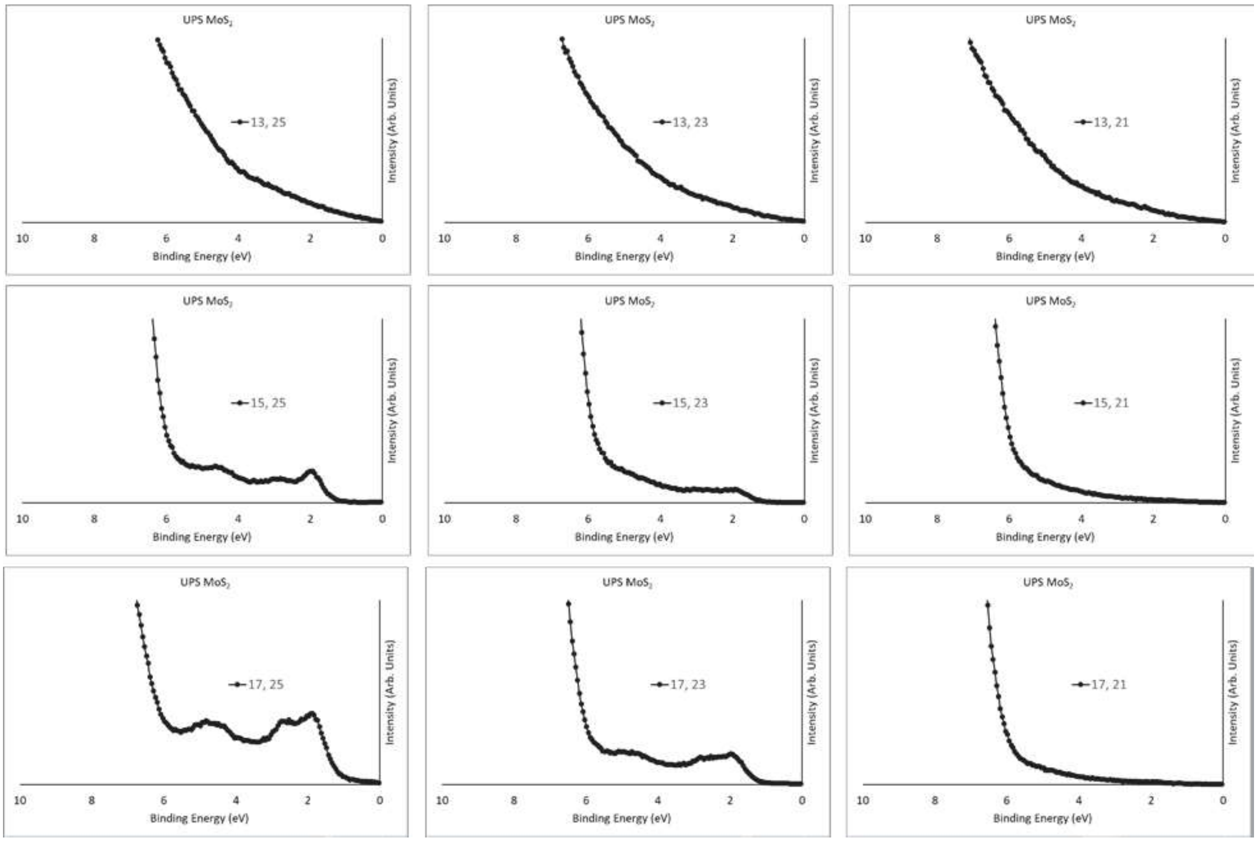

Figure 8–11: Thin film MoS$_2$ UP spectra for all positions 1-9

Singular value decomposition is a useful mathematical process for separating components from within a series of data that experiences a variation in those components between each data set. Previously it was used to separate the interactions MIES had with the sample at various temperatures to isolate the AD components which were directly compared with UP spectra. In this case MIES shows no useful variation and no AD contribution can be determined, however the SVD process can be used to separate the MoS_2 and silicon components within the UP spectra. Variation in coverage, throughout the series of different locations, would result in different concentrations of MoS_2 and hence vary the contribution of the MoS_2 and silicon DoS. Three separate components A, B and C eventuated from the SVD analysis. The reference spectra are plotted in Figure 8–12 with the respective coefficients presented in Figure 8–13.

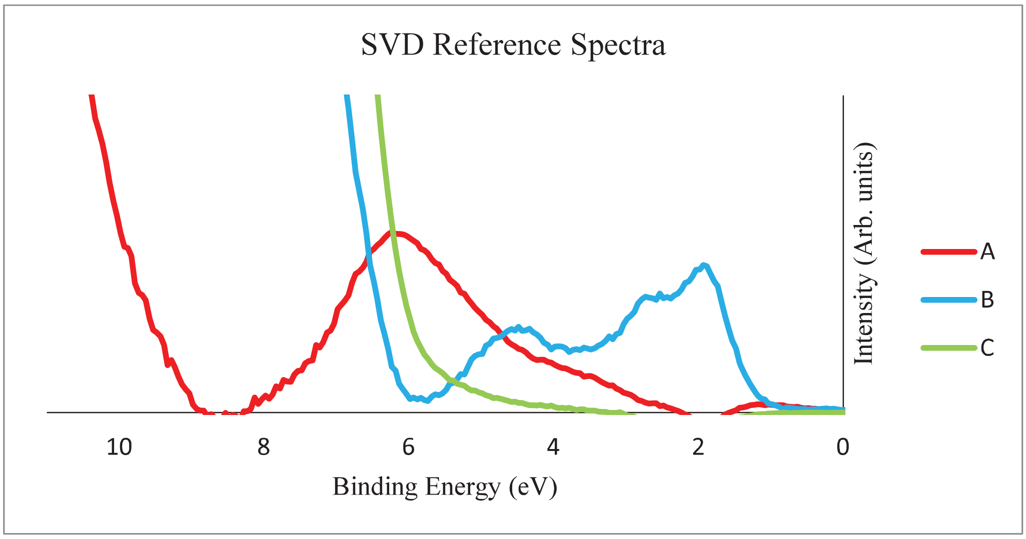

Figure 8–12: SVD reference spectra for MoS_2 UPS

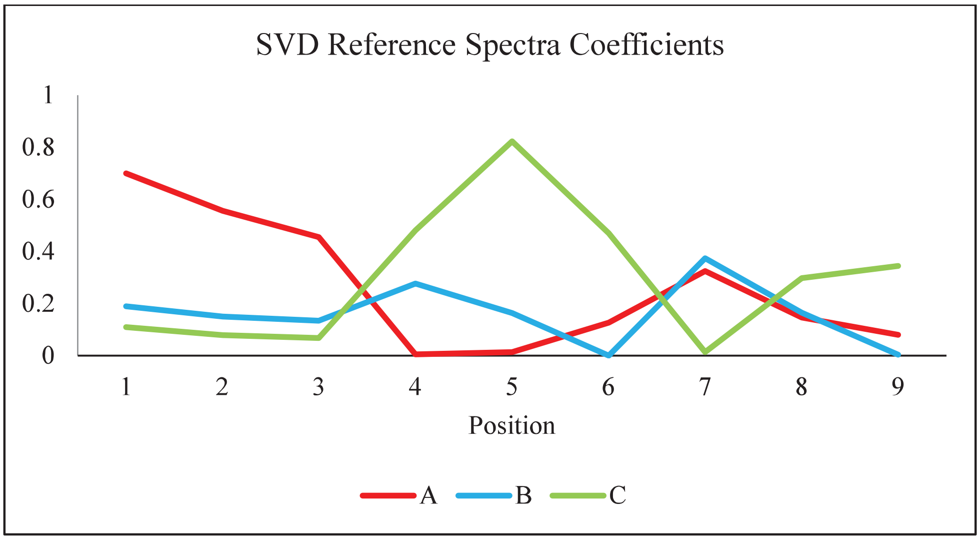

Figure 8–13: SVD reference spectra coefficients

Spectrum B, allocated as the MoS_2 reference spectrum, has a structured DoS which is in close agreement with literature for MoS_2 [12] and is similar to the bulk MoS_2 UP spectra previously measured. Examining the reference spectra coefficients, spectrum B minimises at positions 6 and 9 indicating that the right section of the sample has reduced MoS_2 contribution. The strongest MoS_2 contribution appears at positions 4, 5, 7 and 8. Reference spectrum A possesses a shape similar to silicon with adventitious carbon whilst reference spectrum C appears as a featureless signal that looks similar to secondary electron background, indicating that the background signal varies throughout measurements. Spectrum A, allocated to represent silicon with adventitious carbon, dominates positions 1, 2, 3 ,6 and 9; examining the spectra in Figure 8–11, this correlates with the lack of structure between 0 eV and 6 eV at these positions. Reviewing reference spectrum A, a feature between 1.5 eV and 0 eV that is not observed in any measured UP spectra is found. This is a mathematical artefact originating from the modelling algorithm discussed in Section 2.4.1. Negative values in reference spectra are minimised however in some circumstances are unable to be completely omitted during the modelling due to the limitations of the algorithm. It should be highlighted that this does not represent any real negative values in intensity, but negative values in one of many reference spectra that when summed result in a simulated spectrum that closely resemble the measured spectra. Multiplying the reference spectra illustrated in Figure 8–12 by the coefficients plotted in Figure 8–13 and adding the three resultant spectra results in simulated spectra that are compared with the measured spectra in Figure 8–14. The fit between the simulated and measured spectra were optimised by the solver and were unable to be optimised any further. It is worth noting that spectra 6 and 9 experience major differences in the low binding energy due to the artefact in reference spectrum A.

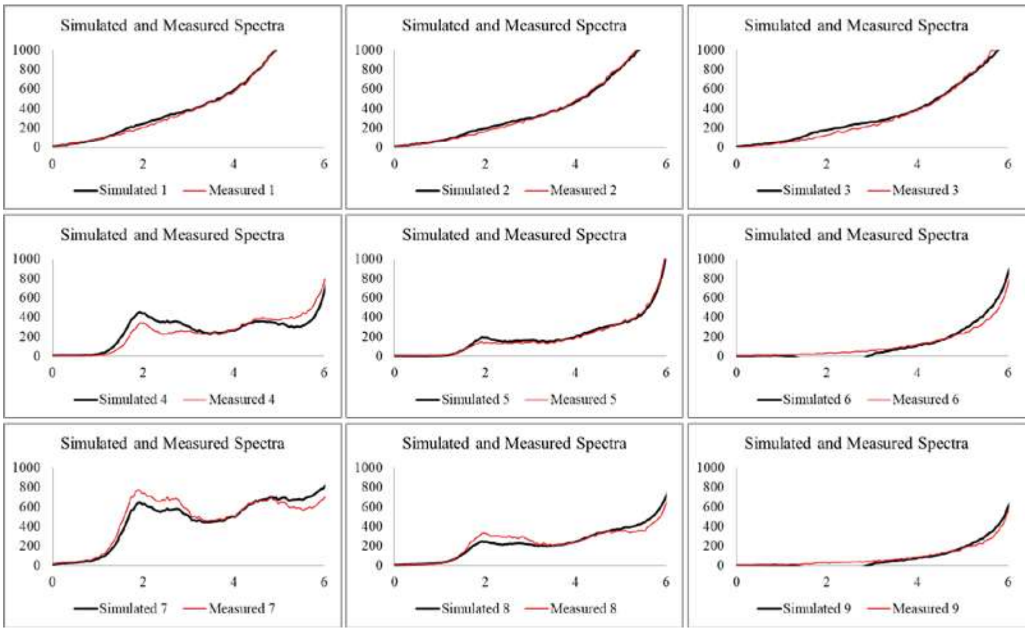

Figure 8–14: Comparison of simulated spectra with measured UPS spectra

The difference between the measured spectra and simulated spectra has been plotted for all spectra in Figure 8–15, there are two specific areas that the modelling had difficulty with; the 1 ev to 3 eV region which is associated with the MoS_2 DoS and the 5 eV to 8 eV region which is associated to the silicon and carbon DoS.

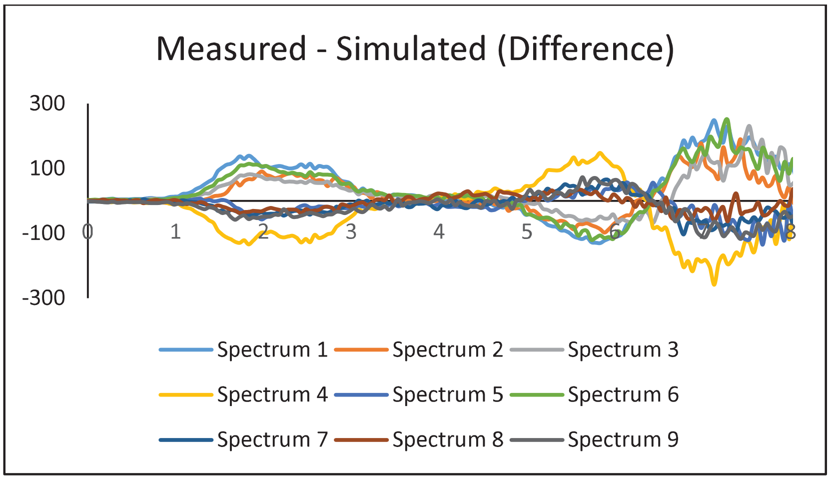

Figure 8–15: Difference between simulated and measured spectra

Due to the nature of the sample, the coverage of the sample varies greatly within the analysis area with a radius of 0.7 mm. This results in the limited separation of components due to the variation within sampling areas. To improve separation, one would either require a much higher sampling across the surface, such as increasing from 3 × 3 to 10 × 10 sample areas, or an improved coverage which would limit the variation within the sampled areas. Given the presented data exceeds 20 hrs continuous supervised measurements, it would require alternating users, or having the sample remain unattended and heated whilst the original user rested appropriately; neither are practical due to filament lifetime and lab safety. The alternative of producing a sample with less sample variation such as a single monolayer or bilayer would be ideal.

The reference MoS_2 spectrum obtained from the SVD process is compared with the bulk MoS_2 in Figure 8–16. The type of coverage has not been defined, as such this MoS_2 component can only be assigned to describing thin film MoS_2, in contrast to specifying as monolayer, bilayer or multilayer of a specific numeration. It is worth noting however that the DoS differ considerably from the bulk crystal of MoS_2. This may be an effect of confinement of the MoS_2 to a few number of layers. As the number of layers increase a repetition of the band structure tends to result in the broadening of components within the DoS. It is also known that confining the thickness of MoS_2 results in increases in the bandgaps [5], which is represented by the increase in Fermi edge cut off.

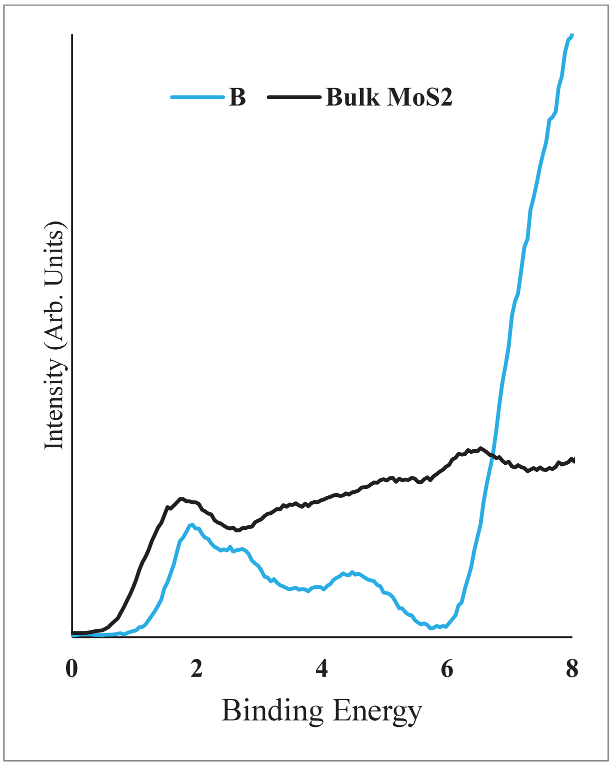

Figure 8–16: A comparison of bulk MoS_2 and thin film MoS_2

The SVD process has allowed for the separation of MoS_2 DoS from the substrate and other material such as adventitious carbon. The form of this MoS_2 is not known through these instrumental techniques alone. As such further characterisation is required to assist in understanding whether the MoS_2 component is related to any specific form of MoS_2.

8.7.1. Raman Spectroscopy and Optical Imagery

Raman spectroscopy and optical imagery were chosen as suitable instrumentation to examine the thin film structural properties and provide some insight into the coverage. Experimental details are discussed in Section 4.4.

Figure 8–17 contains an optical image of the MoS_2 that was taken with a series of positions highlighted. The positions highlighted are examples of key positions chosen to conduct Raman spectroscopy to evaluate the structural properties. The respective Raman spectra are displayed adjacent to the indicated positions. The optical image itself appears to have triangular crystalline structures, MoS_2 grown using chemical vapour deposition is known to grow in triangular or hexagonal shapes.

The first region within the triangular crystalline shape appeared to be MoS_2 with peaks at 384.8 and 404.5 cm^{-1}. The separation of these peaks (19.7 cm^{-1}) combined with the high intensity of the silicon peak at 520 cm^{-1} indicates monolayer MoS_2 in this region [14]. The second location, a white cloudlike region, still has MoS_2, however the reduced silicon peak intensity indicates a higher MoS_2 concentration. The MoS_2 peaks are situated at 382.5 cm^{-1} and 408.5 cm^{-1} and are separated by 26 cm^{-1}. This separation combined with the higher MoS_2 concentration than the monolayer indicates multilayer MoS_2 [14, 15]. The last region which is a dark black spot on the optical image possesses high intensity MoS_2 peaks at 380.0 cm^{-1} and 406.0 cm^{-1} with no visible silicon peaks. The MoS_2 is thus thick enough to obstruct the detection of silicon and is classified as bulk MoS_2.

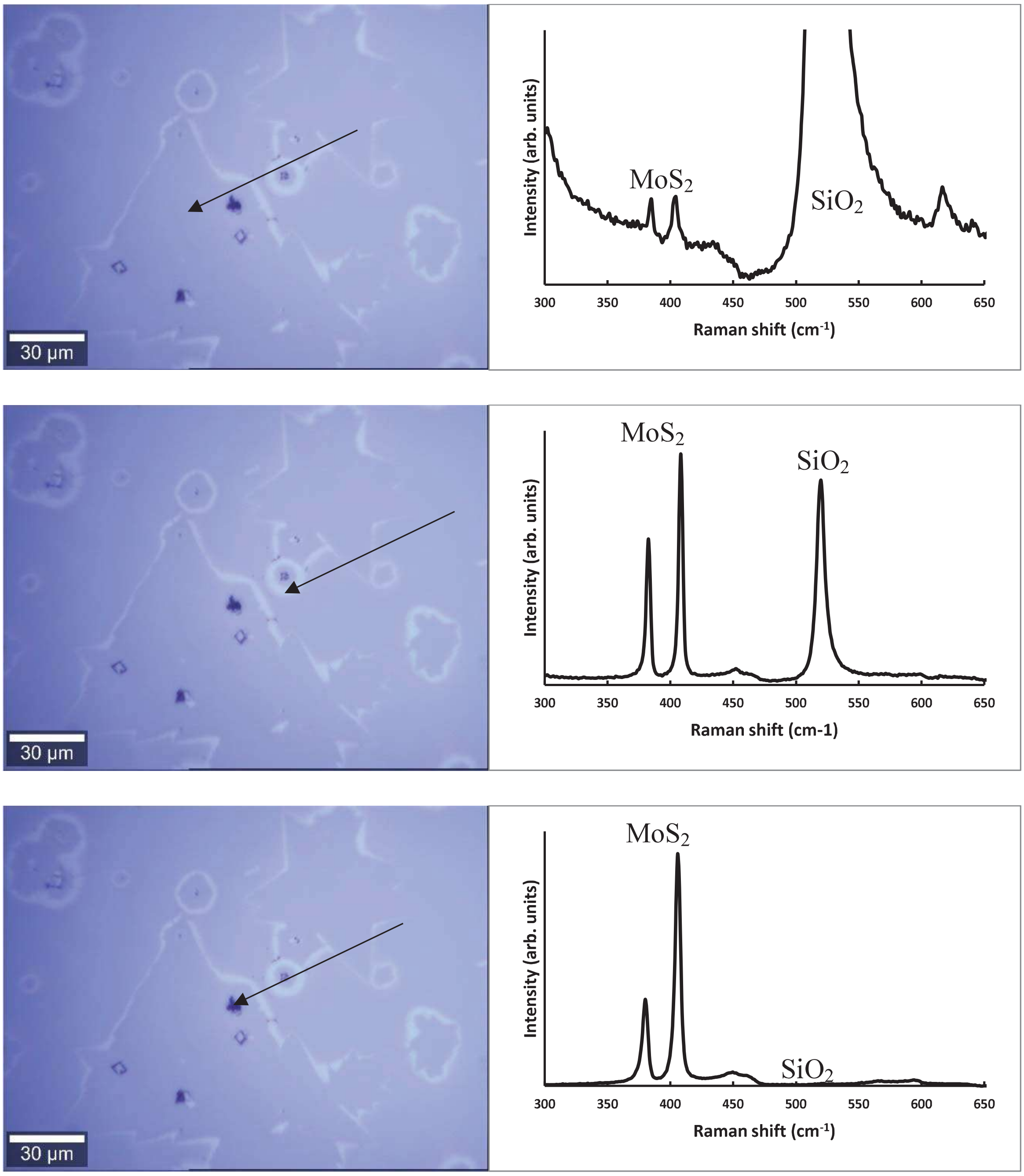

Figure 8–17: Optical images with labels that correspond with adjacent Raman spectra

Figure 8–18 illustrates a series of optical images that were taken with an approximate spacing and locations as the MIES, UPS and XPS. There were no methods of specifying the position on the Raman and optical microscope to the specific positions as the XPS and UPS. The positions taken were estimated by hand using the light source focused to a point as a guide. Regardless of the positional error of the optical image, evaluating the images it is evident that the sample variation in terms of both coverage and quality between sampling positions varied substantially. The area of the images taken were approximately 300 × 500 µm, much smaller in comparison to the 1.4 mm analysis area that the UPS and XPS.

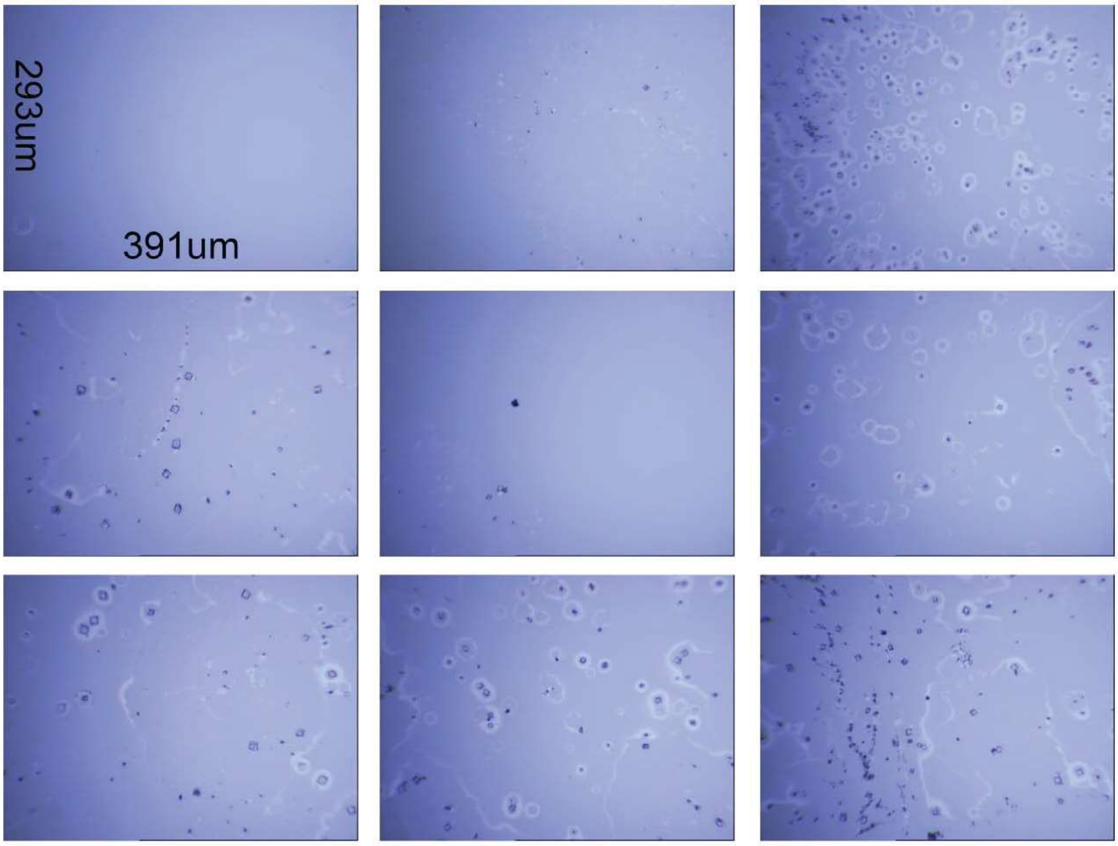

Figure 8–18: Optical images at approximately similar locations as UPS/MIES and XPS

Although these images have not specifically aided in any quantitative evaluation they have indicated that the resultant spectra from UPS and XPS average across areas with high variation in coverage. The combination of optical microscopy and Raman spectroscopy has provided some information on the MoS_2 film; the coverage is irregular, and the thickness of the film is non-uniform.

To quantify the MoS_2 coverage Auger electron spectroscopy and scanning electron microscopy (SEM) is considered for further characterisation.

8.7.2. Scanning Electron Microscopy and Auger Spectroscopy

SEM and AES measurements were conducted on the PHI 710 Scanning Auger Nanoprobe at Flinders University. A series of SEM images of the thin film sample is presented in Figure 8–19. The images were taken with the maximum field of view (FOV) 2000 µm using a 1 kV and 10 nA beam profile. The black and white scale provides a scale of the measured electron intensity spatially. The flat light areas represent the silicon substrate whilst the rough dark areas represent the deposited MoS_2 film. The black and white scale relates to signal intensity.

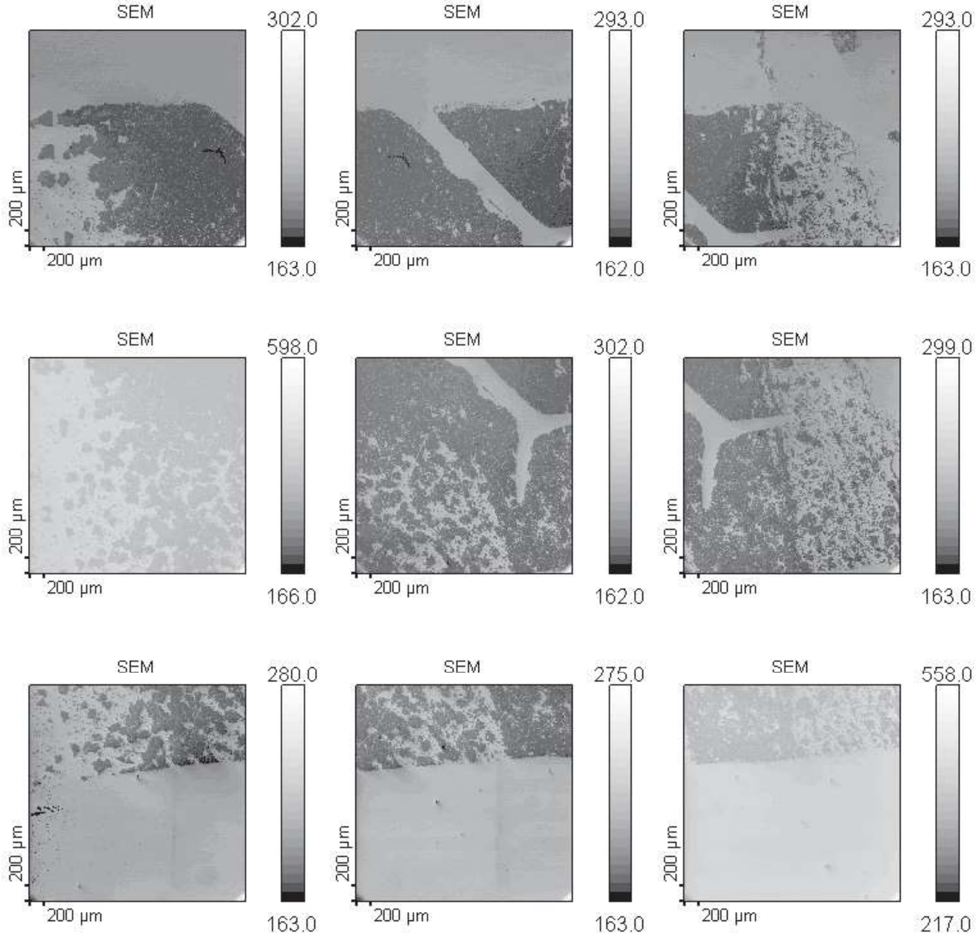

Figure 8–19: SEM images of MoS_2 thin film sample

The series of SEM images have been stitched into a single image, displayed in Figure 8–20, approximately 6 × 6 mm. The precise locations that XPS and UPS were conducted are still unable to be connected to the SEM image, however it can provide context to the evaluation of individual sample positions. The first observation to make is confirming that the centre of the sample, position 5, has a large vein of silicon, assisting in explaining the decrease in MoS_2 in the XPS results, Additionally the coverage towards the right of the sample, positions 3, 6 and

9 have scarce coverage and explain the lack of structural features in the UPS for these positions.

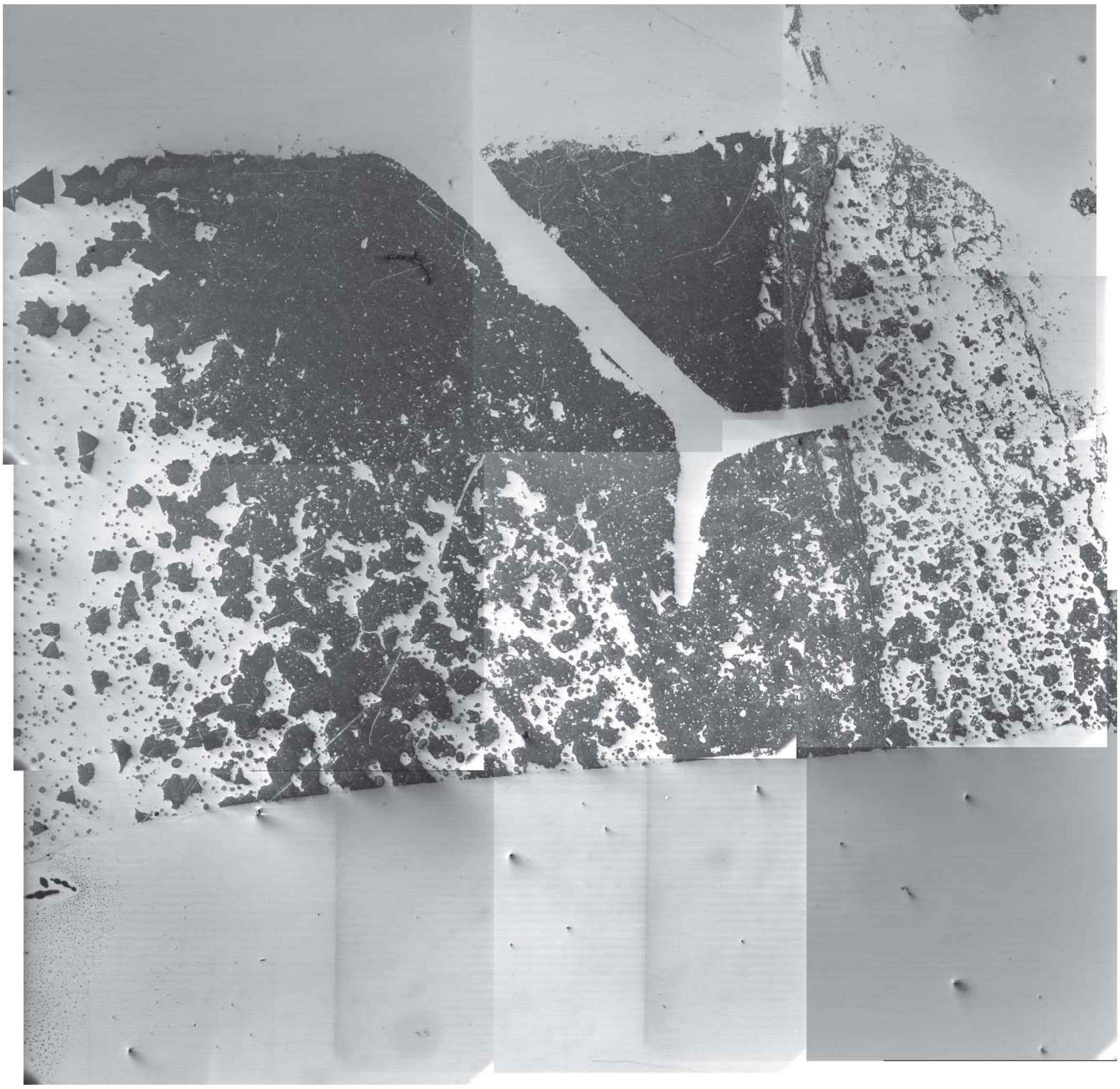

Figure 8–20: Stitched SEM image (Approximately 6 × 6 mm)

From this SEM image one can approximate the coverage using some free image analysis software “imageJ” obtained from “https://imagej.nih.gov/ij/”. This software was used to analyse the range of colours for every pixel in the image. A histogram is produced and a range of limits can be provided to calculate the area within this histogram such that a proportion can be made. Whilst making these limits the highlighted regions on the image are presented such that by changing the limits in increments one can evaluate the effect visually. Figure 8–21 is an illustration of this histogram for the stitched SEM image whilst Figure 8–22 represents the areas selected using the limits 45 to 128 on the greyscale colour intensity histogram. Using the limits of 45 to 128 representing the MoS_2 and 135 to 255 representing the silicon the total area counted for MoS_2 and silicon were 1796818 and 1729167 respectively giving an approximate 51 % MoS_2 and 49 % silicon proportionality.

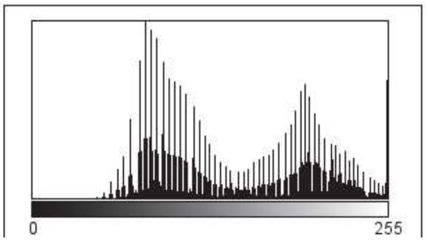

Figure 8–21: Histogram of stitched SEM image

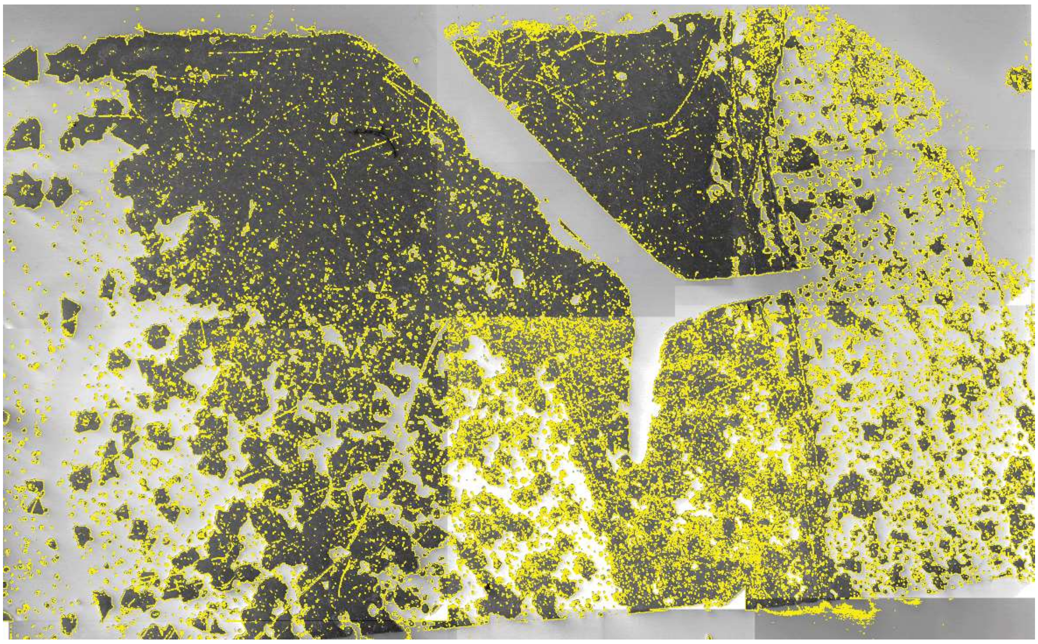

Figure 8–22: Highlighted region for limits of 48 to 128, MoS_2 *encompassed by selection*

The first set of SEM images (2000 µm FOV) were to illustrate the general coverage. Using SEM with lower FOV in conjunction with Auger spectroscopy the composition with spatial resolution can be characterised. All further AES and SEM measurements are conducted with a 10 kV and 10 nA beam profile. An SEM image with a 500 µm FOV is presented in Figure 8–23. The areas of interest in the SEM are labelled 1 to 5 and were analysed using Auger spectroscopy; the resultant spectra are presented in Figure 8–24. It should be noted that unlike the XPS and UPS, the Auger spectrometer had no heating filaments, as such no in-situ heating in vacuum was conducted. Thus direct comparison of XPS and Auger will not be suitable as the measured surfaces will not be identical; the Auger spectrometer will be analysing a surface with adsorbed water and adventitious carbon. The resultant Auger spectra are presented in Figure 8–24.

Position 1 appears to be an empty area in the SEM image and is described by the Auger spectrometer as having silicon (18.7 %) and oxygen (70.8 %) indicating it is the silicon oxide substrate with some adventitious carbon (10.4 %). Position 2 in the optical image seems to be darker and have variations in colour, the Auger spectrum indicates MoS_2 (12.6 % Mo, 19.2 % S) and a lower concentration of silicon (10.3 %) and oxygen (9.7 %) is present, although a high amount of carbon (48.2 %) is present. Due to the high MoS_2 concentration and some silicon still being detected it is concluded that this area is comprised of a thin film of MoS_2 ranging from a monolayer to a few monolayers thick. Position 3 focussed on a square crystalline structure that appeared white in the SEM image. The Auger spectrum for position 3 indicates high MoS_2 concentration (19.1 % Mo, 28.2 % S) with high carbon (45.5 %) and some oxygen (7.1 %). No silicon is detected indicating that this crystalline structure is bulk MoS_2. Position 4 is an area just next to the crystal at position 3 and looks similar in appearance to position 2. Unlike position 2 however, no silicon is detected at position 4; combined with a higher MoS_2 concentration, this area can be classified as multilayer to bulk MoS_2. Position 5 looks like a single MoS_2 triangle crystal in the SEM image; the Auger spectrum shows a high concentration of silicon (22.2 %), oxygen (44.8 %) and carbon (17.8 %), with the least amount of MoS_2 (6 % Mo, 9 % S) seen, excluding plain silicon areas, further indicating the triangle is a single monolayer of MoS_2.

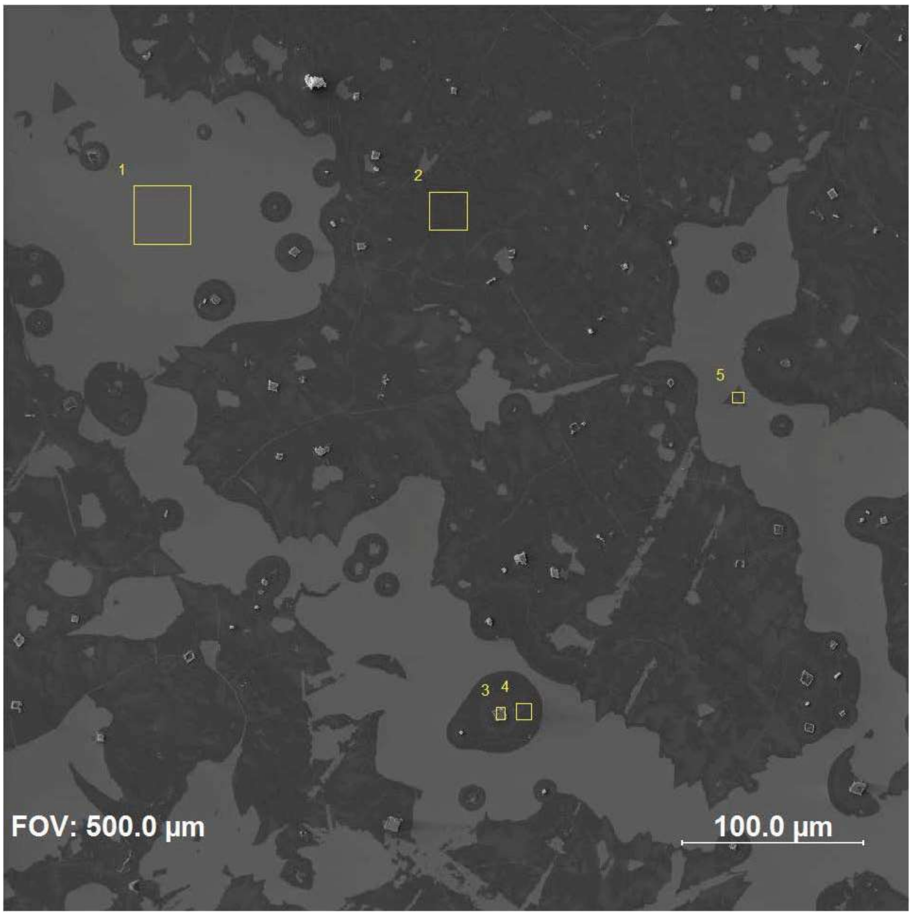

Figure 8–23: SEM image of MoS_2 with labels of interest for Auger spectroscopy

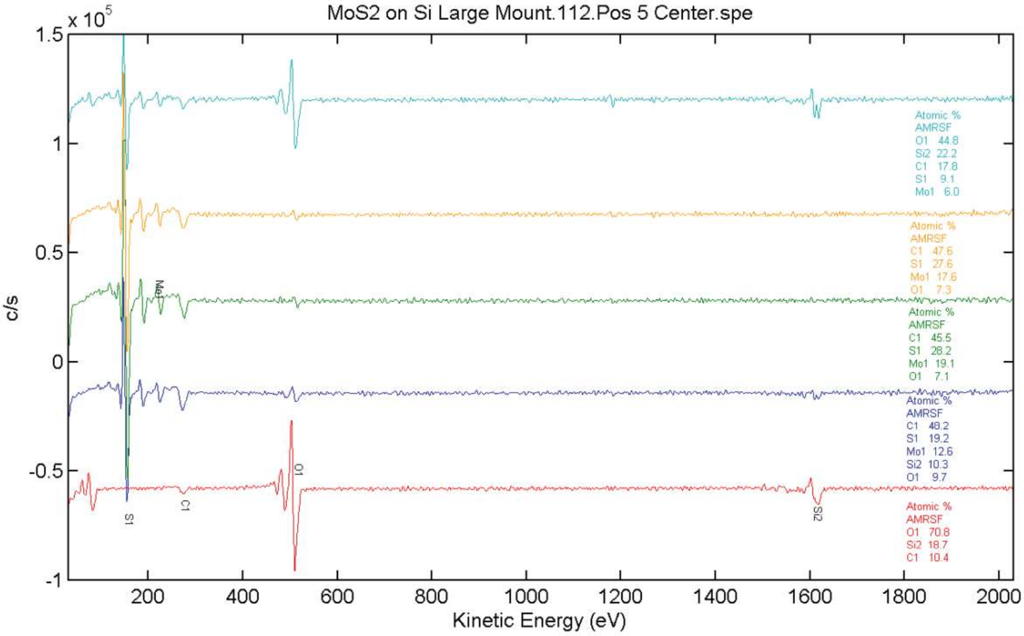

Figure 8–24: Auger spectra for positions 1 (bottom) to 5 (top)

Using a similar method to that used for the stitched SEM image, imageJ was used to approximate the proportion of MoS_2 and silicon within the 500 µm FOV SEM image. An extension to the previous method was made in an attempt to identify the proportion of single and multilayer MoS_2 using an extra set of limits.

Using the greyscale thresholds shown in Table 8-6 specific areas of the image are selected. Figure 8–25 is the result of setting thresholds; the selected regions, defined by the thresholds, are coloured black. Figure 8–25a highlights all MoS_2 as black whilst Figure 8–25b highlights all the silicon as black. An attempt at highlighting single monolayer MoS_2 is made and the resultant selection is presented in Figure 8–25c. The remainder of the MoS_2 (multilayer or bulk) is highlighted in Figure 8–25d. The resultant areas are presented in Table 8-6 and indicate that 35.7 % of the surface is silicon whilst the sum of single monolayer and few monolayer components results in total MoS_2 coverage of 64.3 %. To separate the monolayer film from the multilayer or bulk the thresholds were modified. The threshold was modified to select monolayer regions using the single triangle of MoS_2 previous characterised as a target; tuning the selection such that the triangle was selected. Once a sharp selection had been made the area was counted. The remainder of the MoS_2 threshold was used to define an area of multilayer or bulk MoS_2. The bulk crystalline structures that were previously defined as being MoS_2 unfortunately have a bright white colour in the SEM image which proved to be problematic as the population of this colour existed within the same colour range that the silicon areas possessed. As such the silicon is over represented, reviewing Figure 8–25b it can be seen there is some black selection within the crystals examined using Auger spectroscopy. This area is minimal and does not detract from the approximation of the coverage.

Table 8-6: ImageJ thresholds and measured area proportions

Element	Thresholds	Area	%
Silicon	130-174	385283	35.7
MoS_2 total	85-130	694550	64.3
1ML MoS_2	109-130	141748	13.1
MoS_2 few layers	85-109	552802	51.2
Total	85-174	1079833	

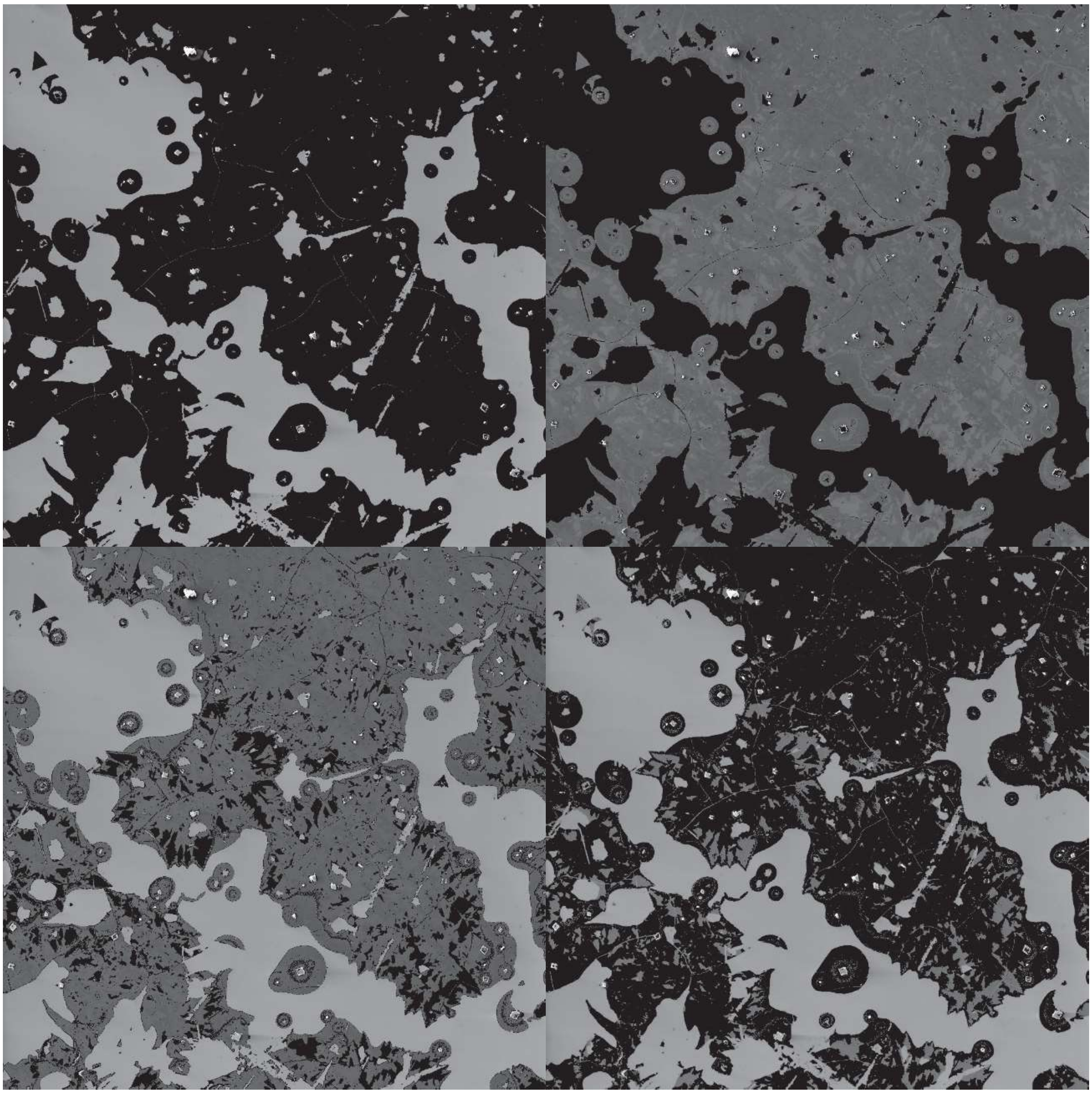

Figure 8–25: (a) MoS_2 area (b) silicon area (c) single monolayer MoS_2 (d) multilayer MoS_2 (2ML to bulk)

A smaller SEM image of 100 µm FOV, Figure 8–26, is taken to improve the characterisation of the thin film and improve the separation of multilayer and single layer MoS_2. This image is a magnification of the region from the bottom right of the 500 µm SEM image. It is easier to identify areas of monolayer and multilayer within this SEM image. The Auger spectra of the highlighted regions are presented in Figure 8–27. Position 1 as expected is bare silicon (24 % Si) with a high amount of oxygen (76 % O). Position 2 consisted of MoS_2 (8 % Mo, 13 % S) but also had a large amount of silicon (19.7 % Si), oxygen and carbon (37.3 % O, 22 % C); possessing a similar composition to the single monolayer MoS_2 triangle in the 500µm FOV SEM image. Areas 3 and 4 are identified as thick MoS_2, that is thick enough to obscure the silicon from the Auger spectrometer, approximately 6 nm or thicker.

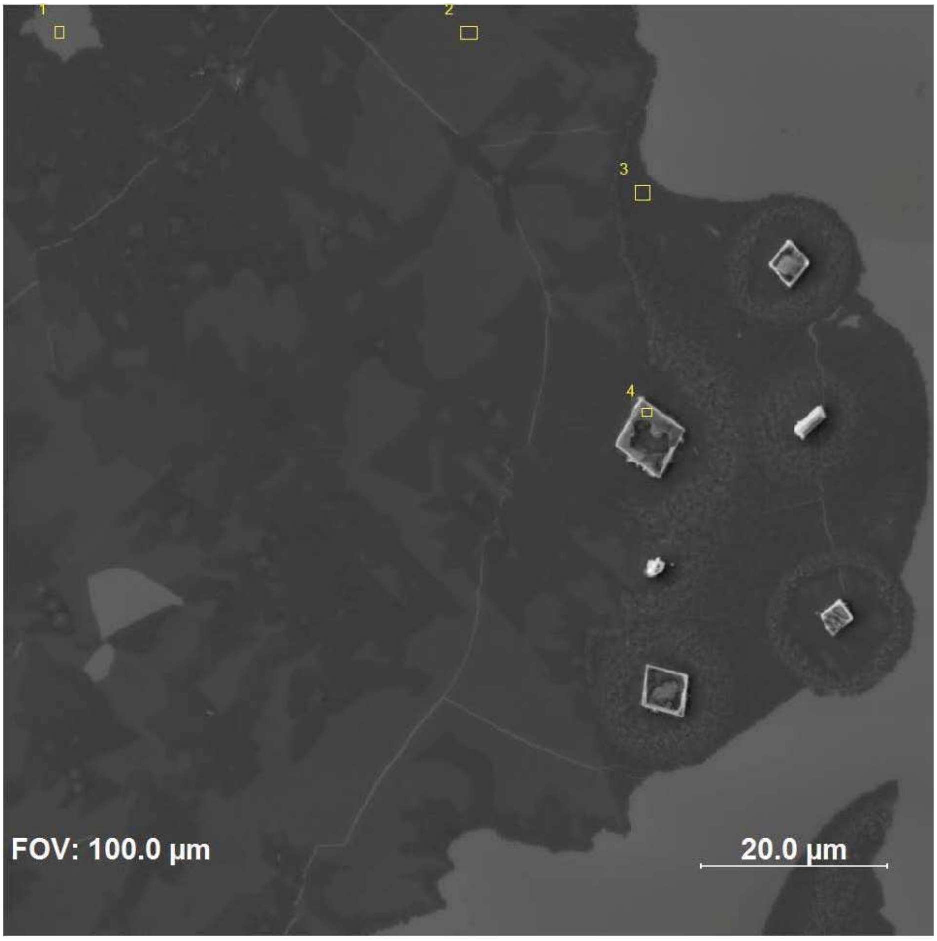

Figure 8–26: SEM image of MoS_2 with labels of interest for Auger spectroscopy

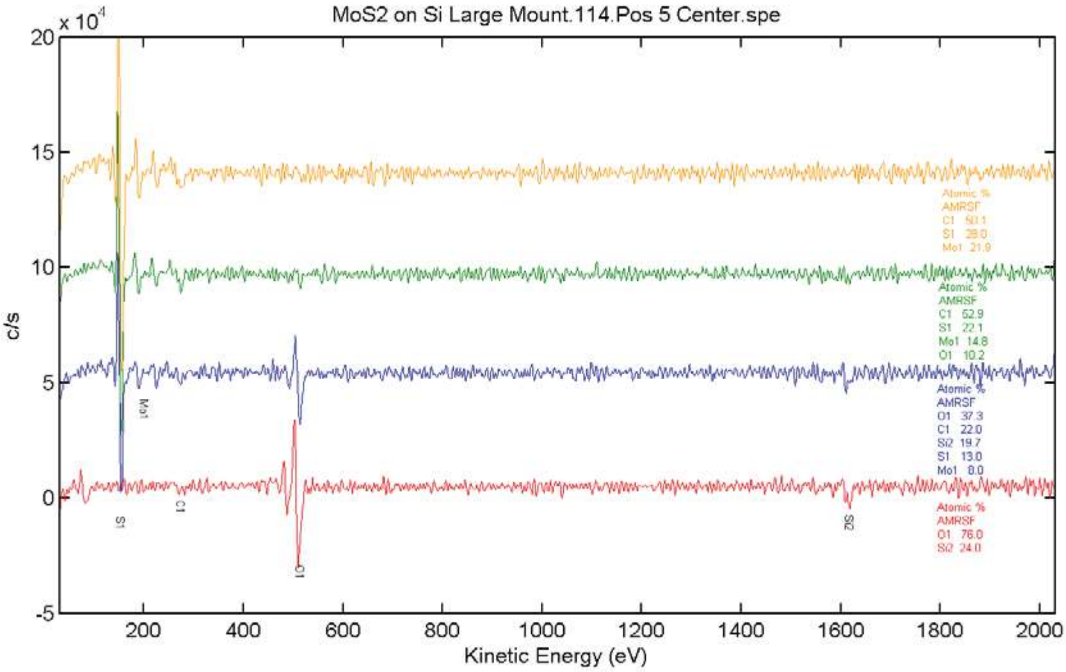

Figure 8–27: Auger spectra for positions 1 (bottom) to 4 (top)

Using a similar approach as the previous SEM images, ImageJ was used to count the areas of monolayer MoS_2, multilayer MoS_2 and silicon, the selected areas are presented in Figure 8–28. Increasing the magnification assists in separating these features.

Increasing the resolution allows for the crystalline features to be ignored using the threshold selection, this reduces the over representation of the silicon. Reviewing Figure 8–28 the crystal structures are not selected by any of the thresholds; the area counted for these are less than 4400 resulting in a contribution less than 1 % within this SEM image.

By increasing the resolution, the detail around the crystalline structure is improved; the crystalline structure is surrounded by a powder like area which appears to be brighter than the multilayer MoS_2 and similar colour on the greyscale intensity histogram as the monolayer MoS_2. A similar powder like area has been measured using Auger spectroscopy; position 4 from the 500 µm image was previously characterised as being thick enough to obscure the silicon such that this feature consists of multilayer or bulk MoS_2. Due to these powder like regions being unable to be separated from the monolayer MoS_2 greyscale limits, the monolayer MoS_2 is now over represented.

The thresholds used to select the regions highlighted in Figure 8–28 combined with the measured areas and proportions are presented in Table 8-7. In the 100 µm FOV SEM image 18.2 % of the sample coverage is silicon with 81.7 % of the sample area being MoS_2. Separating the MoS_2 area into single monolayer and multilayer MoS_2 results in an approximate area of 29.0 % being monolayer and the remained 52.7 % being multilayer MoS_2.

Table 8-7: ImageJ thresholds and measured area proportions

Element	Thresholds	Area	%
Silicon	135-175	189372	18.23769
MoS_2 total	83-135	848983	81.76230
1ML MoS_2	110-135	301457	29.03217
MoS_2 few layers	83-110	547526	52.73014
Total	83-175	1038355	

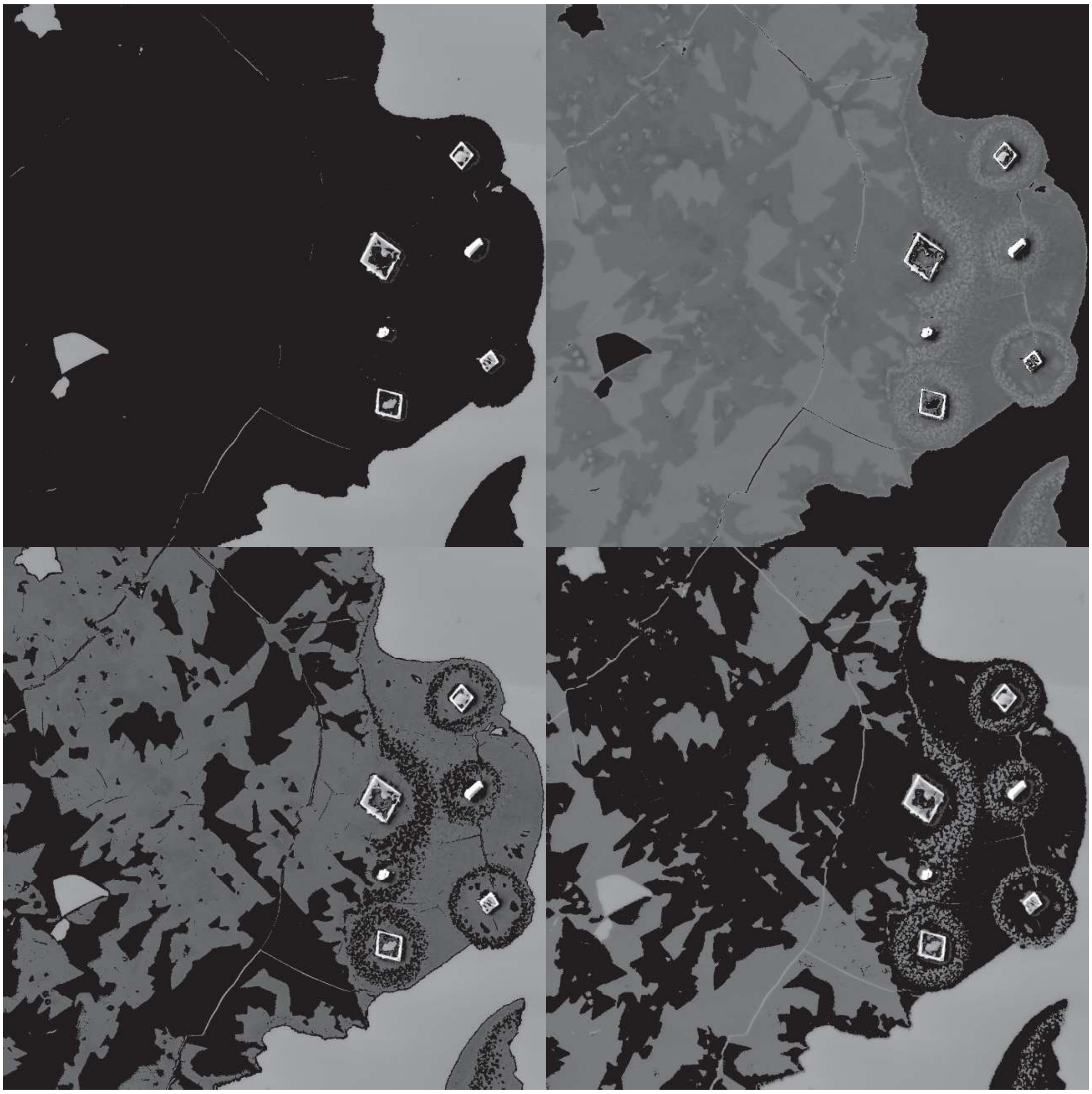

Figure 8–28: (a) MoS_2 area (b) silicon area (c) single monolayer MoS_2 (d) multilayer MoS_2 (2ML to bulk)

Examining the 500 µm and 100 µm FOV SEM images, it is observed that the monolayer regions in Figure 8–28c look identical to the lower resolution 500 µm area in Figure 8–25c. Regardless of the similarities in the thresholds the two FOV SEM images experienced different coverage amounts based on the area sampled. The most important result from these measurements is the separation of the MoS_2 component ratios in relation to the total MoS_2 for the analysed area. The 500 µm FOV SEM image is covered by 64.3 % of MoS_2, this results in the total coverage of MoS_2 being 13 % monolayer whilst 51 % is multilayer or bulk; only examining the MoS_2 area, 20.4 % is designated as monolayer whilst 79.6 % is designated as being multilayer or bulk. The 100 µm FOV SEM image is covered by 81.7 % of MoS_2, this results in the total coverage of MoS_2 being 29 % monolayer whilst 52 % is multilayer or bulk; only examining the MoS_2 area, the ratio of monolayer to multilayer/bulk MoS_2 is 35.5 % to 64.5 % respectively. Given the 500 μm area samples a larger portion of the sample, the ratio of monolayer to multilayer MoS_2 (20.4 % to 79.6 %) will be used to estimate the entire sample. As such any signal in UPS would be heavy dominated by multilayer MoS_2.

8.8. Conclusion

MIES of 2D MoS_2 demonstrated that the spectra experienced very little AD contribution; indicating that this transition metal dichalcogenide possesses orbital vacancies that are spatially permitted, resulting in the RI/AN process to dominate. The resultant spectra are therefore broad and featureless, demonstrating that MIES is less suitable for examining the DoS of 2D TMDCs. SVD of the UPS series successfully separated the DoS associated to the MoS_2 thin film. A comparison of this thin film with the purchased bulk MoS_2 indicated that the thin film possesses sharper DoS features and a higher Fermi edge cut-off, whilst the bulk material experiences a broad distribution of DoS with a lower Fermi edge cut-off indicating a smaller band gap than the film. Optical microscopy and Raman spectroscopy provided some insight into the variation in sample coverage that was experienced in the UPS and XPS. The sample coverage varied greatly and the type MoS_2 found included monolayer, multilayer and bulk. Scanning electron microscopy combined with Auger electron microscopy allowed for the identification of areas of monolayer and multilayer MoS_2. SEM images were analysed using ImageJ to estimate that 20 % of the deposited MoS_2 was single layer whilst the remainder 80 % was multilayer or bulk. Provided that 80 % of the deposited MoS_2 was multilayer, the DoS comparison between the thin film and crystal is a comparison of multilayer MoS_2 and bulk MoS_2 DoS. Through the combination of the spectroscopic methods the determination of the average DoS across a non-homogenous sample has been made.

8.9. Acknowledgements

I would like to thank Antony George and Andrey Turchanin from Jena University for preparing the MoS_2 samples, Alex Sibley and Professor Jamie Quinton from Flinders University for assistance with the Scanning Auger Nanoprobe measurements. I acknowledge the expertise, equipment and support provided by the Australian Microscopy and Microanalysis Research Facility (AMMRF) and the Australian National Fabrication Facility (ANFF) at Flinders University.

8.10. References

1. Mak, K. F., Lee, C., Hone, J., Shan, J., and Heinz, T. F., *Atomically thin* MoS_2*: a new direct-gap semiconductor.* Physical Review Letters, 2010. **105**(13): p. 136805.
2. Frisenda, R., Molina-Mendoza, A. J., Mueller, T., Castellanos-Gomez, A., and van der Zant, H. S. J., *Atomically thin p–n junctions based on two-dimensional materials.* Chemical Society Reviews, 2018. **47**(9): p. 3339-3358.
3. Lee, Y., Lee, J., Bark, H., Oh, I.-K., Ryu, G. H., Lee, Z., Kim, H., Cho, J. H., Ahn, J.-H., and Lee, C., *Synthesis of wafer-scale uniform molybdenum disulfide films with control over the layer number using a gas phase sulfur precursor.* Nanoscale, 2014. **6**(5): p. 2821-2826.
4. Kim, J. H., Lee, J., Kim, J. H., Hwang, C. C., Lee, C., and Park, J. Y., *Work function variation of* MoS_2 *atomic layers grown with chemical vapor deposition: The effects of thickness and the adsorption of water/oxygen molecules.* Applied Physics Letters, 2015. **106**(25): p. 251606.
5. Ganatra, R. and Zhang, Q., *Few-layer* MoS_2*: a promising layered semiconductor.* ACS Nano, 2014. **8**(5): p. 4074-4099.
6. van der Zande, A. M., Huang, P. Y., Chenet, D. A., Berkelbach, T. C., You, Y., Lee, G.-H., Heinz, T. F., Reichman, D. R., Muller, D. A., and Hone, J. C., *Grains and grain boundaries in highly crystalline monolayer molybdenum disulphide.* Nature Materials, 2013. **12**: p. 554.
7. Winter, A., George, A., Neumann, C., Tang, Z., Mohn, M. J., Biskupek, J., Masurkar, N., Reddy, A. L. M., Weimann, T., Hübner, U., Kaiser, U., and Turchanin, A., *Lateral heterostructures of two-dimensional materials by electron-beam induced stitching.* Carbon, 2018. **128**: p. 106-116.
8. Kuc, A., Zibouche, N., and Heine, T., *Influence of quantum confinement on the electronic structure of the transition metal sulfide* TS_2*.* Physical Review B, 2011. **83**(24): p. 245213.
9. Ye, M., Winslow, D., Zhang, D., Pandey, R., and Yap, Y., *Recent advancement on the optical properties of two-dimensional molybdenum dDisulfide (*MoS_2*) thin films.* Photonics, 2015. **2**(1): p. 288.
10. Morgner, H., *The quantitative characterization of liquid and solid surfaces with metastable helium atoms.* AIP Conference Proceedings, 2000. **500**(1): p. 687-698.
11. Heinz, B. and Morgner, H., *A metastable induced electron spectroscopy study of graphite: The k-vector dependence of the ionization probability.* Surface Science, 1998. **405**(1): p. 104-111.
12. Fives, K., McGovern, I. T., McGrath, R., Cimino, R., Hughes, G., McKinley, A., and Thornton, G., *The photoelectron bandstructure of molybdenum disulphide.* Journal of Physics: Condensed Matter, 1992. **4**(25): p. 5639.
13. Gilman, J. J., *Direct measurements of the surface energies of crystals.* Journal of Applied Physics, 1960. **31**(12): p. 2208-2218.
14. Lee, C., Yan, H., Brus, L. E., Heinz, T. F., Hone, J., and Ryu, S., *Anomalous lattice vibrations of single- and few-layer* MoS_2*.* ACS Nano, 2010. **4**(5): p. 2695-2700.
15. Mignuzzi, S., Pollard, A. J., Bonini, N., Brennan, B., Gilmore, I. S., Pimenta, M. A., Richards, D., and Roy, D., *Effect of disorder on Raman scattering of single-layer* MoS_2*.* Physical Review B, 2015. **91**(19): p. 195411.

Chapter 9

9. Conclusions

To design devices composed of nanomaterials, the surfaces of dimensionally confined materials are required to be characterised, such that the behaviour of any interface formed by nanomaterials is understood and can be developed for optimal performances. When characterising 2D materials with spectroscopic methods, one encounters a challenge of making a direct quantitative measurement of the surface exclusively, without contribution from its substrate.

This thesis has investigated the electronic and compositional properties of 2D materials using spectroscopic methods. With a heavy focus on MIES, concepts for quantitative measurements of the electronic structure of 2D materials and the separation of information from different layers are developed. The following are conclusions that relate to the aims and scopes discussed in Chapter 3.

9.1. Electronic and Compositional Characterisation of Graphene Oxide

Studies of graphene oxide with varying annealing temperatures highlighted that the electronic performance of thin film graphene oxide is improved through annealing at high temperatures in argon atmosphere. Whilst conductivity measurements highlighted that the sheet resistance of graphene oxide improved by annealing at 1273 K, a combination of UPS and XPS allowed the film to be characterised throughout the temperature series. The UPS measurements described the changes in electronic structure, showing an increase in the 2p π DoS with increasing annealing temperature. The XPS measurements described the compositional changes with increasing annealing temperature, showing an increase in the sp^2 carbon species with increasing temperature, necessary for charge transfer in graphene.

9.2. True Measurements of Graphene Density of States

Metastable (helium) induced electron spectroscopy was used to probe the density of states of graphene, obtaining information pertinent to the surface atoms only, unlike other spectroscopic techniques that measure information as deep as the mean free path of the excited electrons. Using a combination of Raman spectroscopy and MIES, it was found that the number of layers of graphene and the presence of defects within the graphene greatly influenced its DoS; highlighting the importance of directly determining the electronic structure of 2D materials.

9.3. Measurements of Inner and Outer Walls of DWCNT

The Auger deexcitation component from MIES was directly compared with UP spectra to provide separation of the DoS from the surface of DWCNT and its coaxial inner CNT. SWCNT were characterised by UPS and MIES, firstly showing the direct comparison of AD to UPS, and secondly a surface sensitive measurement of the CNT DoS is made. The SWCNT possessed favourable 2p π states necessary for optimal charge transport. DWCNTs characterised by XPS and Raman spectroscopy indicated higher defect concentration than the SWCNT, reflected in the AD component of MIES. UPS however indicated favourable 2p π states indicating that the DWCNT still possessed favourable charge transport properties. The combination of these spectroscopic techniques allowed a comprehensive characterisation of the DWCNTs illustrating that the outer walls of the DWCNTs possessed defects, whilst the inner coaxial CNT retained its sp^2 network and hence its optimal electronic properties. This method has potential in assisting with the preparation of DWCNTs for interfacing in devices to ensure, upon modification of the outer wall for attachment or functionalisation, the inner walls retain the optimal sp^2 network for applications in electronic devices.

9.4. Characterisation of Thin Film MoS_2

MIES of MoS_2 was less suitable for DoS characterisation as it was RI/AN dominated. A technique for examining a non-homogenous 2D material by applying SVD to UP spectra conducted over a series of locations was attempted. A component for the 2D MoS_2 was separated. Characterisation of the surface with Raman Spectroscopy, AES and SEM allowed for the UPS component to be assigned to few layer MoS_2; a quantitative measurement of the DoS for few layer MoS_2 is made. A comparison of few layer MoS_2 with bulk MoS_2 demonstrated an increase in the Fermi edge energy with decrease in thickness, highlighting the bandgap difference between bulk and 2D MoS_2. It has been demonstrated through the combination of spectroscopic methods, that the average electronic structure over a large area of non-homogenous material can be quantitatively determined. With improved sample coverage and thickness control, an ideal sample could lead to improved characterisation of MoS_2 with specified number of layers; an investigation into the DoS changes with incremental thicknesses could be made. This work would be advantageous for the design of tuneable work functions and band gap materials for the use in optimising interfaces within electronic devices.